Title
Surface Modification of Ultrahigh Molecular Weight Polyethylene to Improve Lubrication in Total Hip Replacements

Author
Kane, Sheryl Rose

Publication Date
2008-05-23

Peer reviewed|Thesis/dissertation

Surface Modification of Ultrahigh Molecular Weight Polyethylene

to Improve Lubrication in Total Hip Replacements

by

Sheryl Rose Kane

DISSERTATION

Submitted in partial satisfaction of the requirements for the degree of

DOCTOR OF PHILOSOPHY

in

Bioengineering

in the

GRADUATE DIVISION

of the

UNIVERSITY OF CALIFORNIA, SAN FRANCISCO

AND

UNIVERSITY OF CALIFORNIA, BERKELEY

Dedication

Walk with me the diamond road
Tell me every story told
Give me something of your soul
That I can hold onto…

When the night falls
When you're stumbling
It's gonna take a little time
To make it to the other side

So don't miss the diamonds along the way
Every road has led us here today
Life is what happens while you're making plans
All that you need is right here in your hands.

"Diamond Road" by Sheryl Crow

To six years in California, and some of the diamonds I will always remember:

The heady fragrance of the flowers and the deep shadows from the late-afternoon sun at the Berkeley Rose Garden

Amazing food at every turn – Berkeley Bowl, Oliveto, the Gourmet Ghetto, the Ferry Building

Skiing every trail, gully, and glade at Kirkwood with good friends and (usually) good conditions

Biking in the foothills, up Euclid and Grizzly Peak, with views of the bay and the rolling hills stretching out for miles

Driving through Yosemite after midnight, alone with the deer and the moonlight on a deserted highway through a beautiful park

Acknowledgments

For those who have given me personal friendship, adventure, hours of laughter, and unwavering support through the good times and the bad, thank you. You know who you are.

Many people have also offered me technical expertise, advice, and encouragement. I would like to thank:

Lisa Pruitt, my dissertation advisor, for her advice and perspective, and J.J. and Juan for helping me make one life-changing decision

All of my labmates in the Medical Polymers and Biomaterials Group,
particularly Shikha Gupta and Jevan Furmanski, my staunchest supporters and toughest critics, and now my labmates for life,
and Stephanie Uhlich and Amy Walters, my awesome undergrads

Paul Ashby, for generously sharing his wealth of knowledge, thoughtful critiques, and more of his time than I ever meant to take up

Kyriakos Komvopoulos, for plasma deposition and tribology advice

Michael Martin, for his ATR-FTIR expertise

Steve Kaplan, Russell Kam, and Albert Odom at 4th State Inc., for their cheerful help, knowledge, and access to their plasma deposition equipment

Funding and research support:

National Science Foundation Graduate Research Fellowship

American Association of University Women Dissertation Year Fellowship

Sigma Xi Grant-in-Aid of Research

UCSF Graduate Student Research Award

AFM work at the Molecular Foundry was supported by the Director, Office of Science, Office of Basic Energy Sciences, Division of Materials Science and Engineering, of the U.S. Department of Energy under Contract #DE-AC02-05CH11231.

XPS was performed at the University of Washington NESAC/BIO facility, supported by NIH grant #EB-002027.

Abstract

Almost 200,000 total hip replacements (THRs) were implanted in 2007 in the United States. About one-third of the recipients were under the age of 65. Since THRs typically last 10-20 years, many patients will outlive their implants and require painful, costly revision surgery. Increasing the lifetime of hip replacements would reduce the need for revision surgery and greatly improve patient quality of life.

The most common cause of late-stage failure of THRs is wear-mediated osteolysis, bone loss around the implant caused by chronic joint inflammation from wear particles generated at the articulating surfaces of the hip replacement. In implants that contain an ultrahigh molecular weight polyethylene (UHMWPE) acetabular cup, the UHMWPE generates the majority of wear particles. Consequently, reducing wear at the UHMWPE surface is expected to increase the lifetime of the implant.

This research focuses on improving lubrication at the articulating surface by coating the UHWMPE with crosslinked poly(ethylene glycol) (PEG), a lubricious, biocompatible hydrogel. First, the plasma deposition process used to generate the PEG-like coatings was developed. Plasma deposition power, monomer flow rate, and chamber temperature all affected the coating chemistry and crosslinking, while deposition time and substrate placement determined coating thickness. The resulting coatings are covalently bonded to the UHMWPE. They contain 76-83% ether, indicating that they are very similar to PEG, and are much more hydrophilic and protein-resistant than uncoated UHMWPE.

The PEG-like coatings withstood pin-on-disk testing at 3 MPa contact pressure, comparable to total hip replacements in vivo. Analysis of the wear behavior at the mesoscale (tens to hundreds of microns) and microscale (less than 10 μm, similar to asperity contact) determined that the coatings fail due to a combination of adhesive, abrasive, and delamination wear mechanisms; however, delamination predominated at the mesoscale. Comparison of two sets of coatings with different degrees of crosslinking determined that, at the microscale, the more crosslinked coatings better resist wear and fail only by delamination. This suggests that the wear resistance of PEG-like coatings could be further improved by increasing the degree of covalent bonding to the UHMWPE substrate and increasing the crosslink density of the coatings.

Table of Contents

List of Tables

List of Figures

Appendix: Detailed Experimental Protocols

Chapter 1

Introduction

Total hip replacements

In the United States alone, more than 380,000 partial and total hip replacement surgeries were performed in 2005, over 100,000 more than in 1995 [1]. In addition, one-third of the procedures performed in 2005 involved patients under the age of 65. The average life expectancy in the United States is 78 years [2]; the average life expectancy for a primary total hip replacement is 10-20 years. Therefore, it is clear that many patients will outlive their implants and require costly and painful revision surgery.

Total hip replacements (THRs) are implants intended to reduce pain and restore hip function to patients suffering from hip degeneration, usually caused by arthritis, injury, or congenital defects. The devices replace the cartilage of the acetabulum, as well as the femoral head and neck, with the components shown in Figure 1: an acetabular backing, usually made of titanium to promote osseointegration; an acetabular cup, typically either cobalt-chromium (CoCr), ceramic (alumina or zirconia), or ultrahigh molecular weight polyethylene (UHMWPE); a CoCr or ceramic femoral head; and a titanium or CoCr femoral stem. As in the natural joint, synovial fluid – an aqueous

mixture of proteins, phospholipids, hyaluronic acid, and other biomolecules – surrounds the joint and lubricates the surfaces of the acetabular cup and the femoral head.

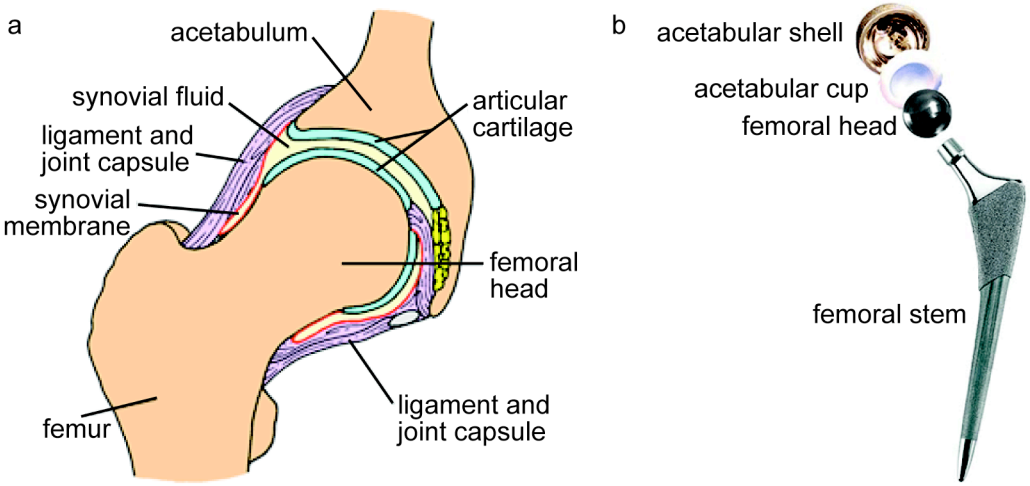

Figure 1: a) Anatomy of the natural hip joint [3]. The femoral head and neck, as well as the acetabular cartilage, are replaced by b) the components of a typical total hip replacement [4].

The basic design of contemporary implants has existed since the late 1950s, when Sir John Charnley first began implanting devices with relatively small femoral heads – 22 mm in diameter, much smaller than the natural femoral head – to reduce friction during articulation against the acetabular cup. He initially used cups made of Teflon, but switched to ultrahigh molecular weight polyethylene within a few years because it exhibited greatly superior wear behavior [5]. Although some current implants have ceramic or metal acetabular cups, the majority implanted in the United States are still made of polyethylene.

Ultrahigh molecular weight polyethylene: microstructure and strain hardening

UHMWPE is a polyolefin made of CH_2CH_2 repeat units. It consists of very long, entangled linear chains with a molecular weight of up to 6 million g/mol, as opposed to only 200,000 g/mol for high density polyethylene, HDPE, which is used to make milk bottles and other packaging [6]. The long chains confer significant wear resistance, such that UHMWPE acetabular cups exhibit very low linear wear rates, on the order of 0.1 mm/year in vivo [7].

UHMWPE is semi-crystalline, with about 50% crystallinity (the exact percentage depends on processing) and an unusual microstructure, shown in Figure 2. The crystalline regions consist of tightly-packed UHMWPE chains folded over and over into plate-like structures, called lamellae, which are roughly 10-50 nm thick and 10-50 μm wide and long [5]. The material surrounding the lamellae is an amorphous entanglement of polymer chains, including some that are partially incorporated into one or several nearby lamellae. The amorphous phase is well above its glass transition temperature (-80°C), which enables large amounts of recoverable chain extension and deformation. Each lamella contains multiple polymer chains, and these individual chains also often pass through the amorphous region and into other lamellae, creating a network of interconnected crystallites. Chains that span multiple lamellae are known as tie molecules, and they contribute significantly to the behavior of the material under load.

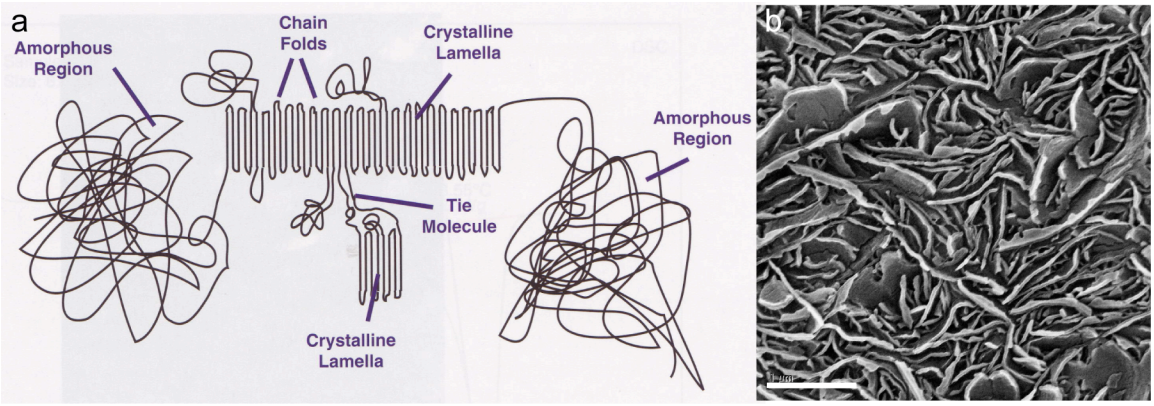

Figure 2: a) A schematic of the microstructure of UHMWPE, reproduced from [6]. b) A scanning electron micrograph of the lamellar structure of UHMWPE; the scale bar is 1 μm.

Under plane strain, the microstructure of UHMWPE rearranges such that the lamellae orient normal to the loading direction. The material exhibits two primary deformation mechanisms. First, the lamellae slip with respect to each other, allowing them to rotate and elongate (Figure 3) until the tie molecules are fully extended. This occurs by a compression ratio of 1.95. At this point, the lamellae start to lock into place, and further deformation occurs by lamellar bending to form a V shape. By a compression ratio of 4.0, the lamellae are oriented with their normals either parallel to the loading direction or 28° off from the loading direction due to bending [8]. Similarly, under uniaxial tension, the UHMWPE microstructure first undergoes interlamellar slip and rotation, followed by lamellar locking at an angle of ~65° from the direction of the tensile force (Figure 4) [9].

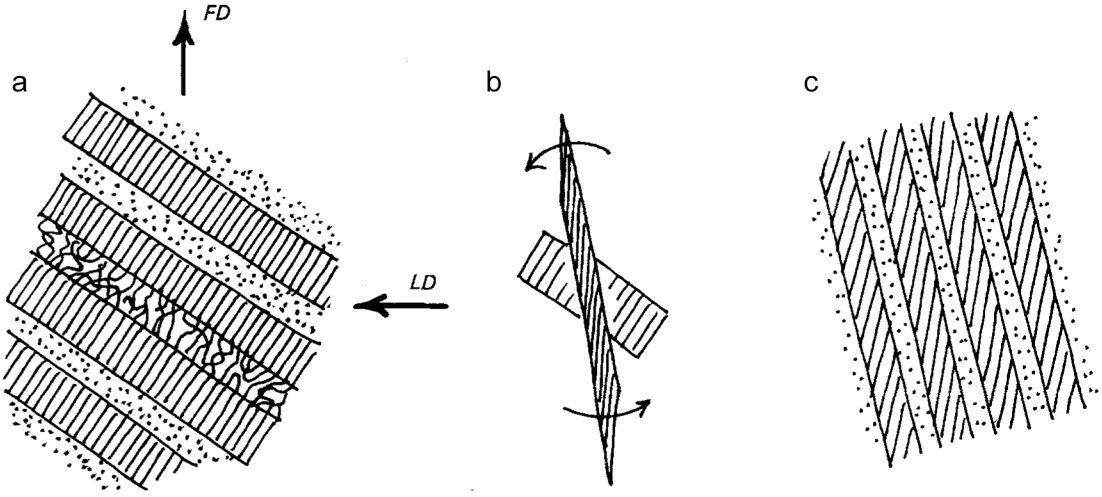

Figure 3: Lamellar evolution under stress, modified from [10]. LD is the loading direction and FD is the flow direction. a) Interlamellar shear, b) rotation, and c) elongation. Note that this diagram represents HDPE, not UHMWPE. In HDPE, the lamellae naturally pack into ordered regions called spherulites; hence, the unstrained material shown in part a) takes the form of a spherulite rather than the random orientation of lamellae seen in unstrained UHMWPE.

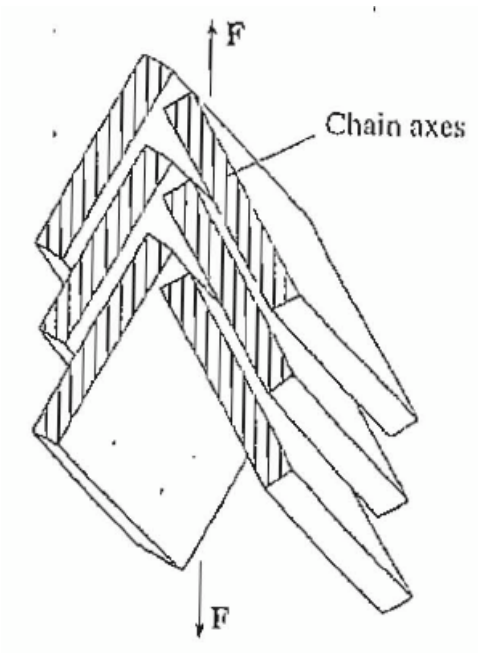

Figure 4: Final lamellar orientation in UHMWPE after uniaxial strain; the lamellae are oriented ~65° off of the direction of tension. Reproduced from [9].

Lamellar alignment, or orientation, in UHMWPE is responsible for its tendency to strain harden. Under unidirectional shearing, the lamellae orient relative to the direction of shear, hardening the surface more in the direction of the shear. However, the material correspondingly weakens in other directions, such that the material is less resistant to cross-shear perpendicular to the primary direction of sliding. In UHMWPE, strain hardening results in reduced rupture strength in the direction transverse to orientation [11] as well as substantially higher wear rates for multidirectional rather than linear or reciprocating motion; for example, Wang et al observed a difference of two orders of magnitude between multidirectional and reciprocating wear tests [12].

Strain hardening is clinically relevant because articulation in total joint replacements is multi-directional, with a primary sliding axis in the direction of the stride as well as cross-shear along a multitude of secondary axes due to rotation, adduction/abduction, and other motions. Lamellar orientation has been observed in retrieved acetabular cups [13] and is considered to be a precursor to wear particle formation [14]. The formation of wear particles is highly unfavorable because wear particles in the joint space can induce a severe inflammatory response that culminates in wear-mediated osteolysis, or bone loss, which is the primary cause of late-stage failure of total hip replacements.

Wear-mediated osteolysis

First recognized in the 1980s, wear-mediated osteolysis, also known as aseptic loosening, was then identified as “particle disease” or “cement disease,” with the

inflammatory particles attributed to the poly(methyl methacrylate) (PMMA) bone cement then employed to adhere the femoral stem to the femur [15, 16]. However, the use of non-cemented, osseointegrating stems did not prevent particle disease, as had been expected. In 1990, Maloney et al first suggested that polyethylene wear particles might be the true cause [17]; by 1994, the concept of "cement disease" had been debunked after studies determined that, although PMMA and metal particles can cause osteolysis, the UHMWPE acetabular cup generates the majority of inflammatory particles [16, 18, 19].

Not all UHMWPE (or PMMA or metal or ceramic) particles are inflammatory. The immune system evolved to fight off more traditional disease vectors such as viruses and bacteria, which tend to be approximately 0.1 μm and 1 μm in diameter/length, respectively [20]. Consequently, the immune system is extremely sensitive to particles in this size range, which is also the size scale of most UHMWPE wear particles generated by the hip: 90% of polyethylene wear particles are 1 μm or less in size [21]. Unfortunately, the immune system has minimal capability to distinguish between invasive microorganisms and inert wear particles, so the response to all foreign bodies on this scale follows the same basic steps: opsonization, phagocytosis, release of pro-inflammatory and cytotoxic molecules by the macrophages, and, if the material is not successfully eliminated by these processes, escalation of the inflammatory response and transition from acute to chronic inflammation [21-26]. In the bone around joint replacements, the chronic immune response caused by wear debris culminates in bone loss. Figure 5 shows the complicated immune cascade that leads to wear-mediated osteolysis.

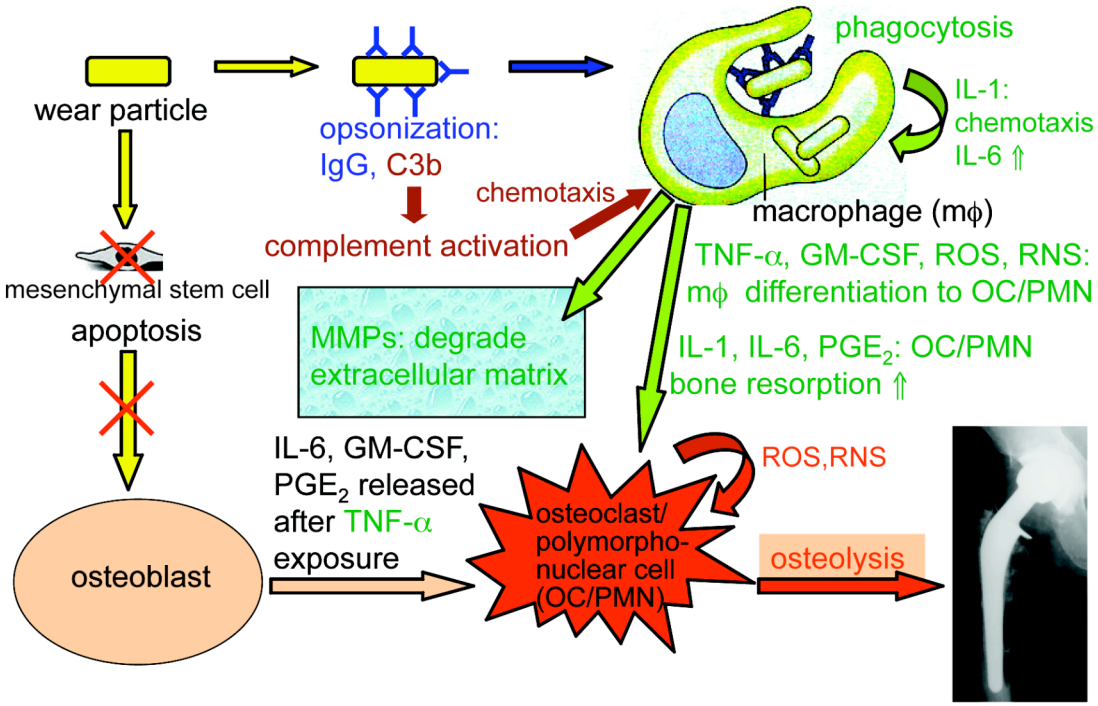

Figure 5: The immune response to wear particles. The process begins in the top left corner and proceeds to the bottom right. Opsonization is shown in blue, complement activation in dark red, and direct effects of phagocytosis in green. Straight arrows indicate effects exerted by one particle, cell, or process on other cells or processes, while curved arrows indicate autoactivation (a single cell releasing chemicals that further stimulate the same cell).

Opsonization and phagocytosis involve related defense mechanisms.

Opsonization is the process of specific proteins adsorbing to the surface of a foreign body, such as a bacterial cell wall or a polyethylene wear particle. These proteins, which include ubiquitous biomolecules such as fibrinogen, as well as more specialized antibodies such as IgG, are known as opsonins. Their function is to adhere to the surface of the foreign body and essentially provide handles to which macrophages can attach, enabling more efficient and rapid phagocytosis. Some opsonins, such as C3b, also activate the complement system, a secondary pathway that also can produce a strong inflammatory response.

Macrophages are multifunctional immune system cells that are found in tissues throughout the body. One of their primary modes of action is phagocytosis, the process of enveloping material and ingesting it into the macrophage for digestion. The material can be a number of things, including viruses or bacteria; dead, damaged, tumor-forming, or virally-infected native cells; or very small foreign body particulates, such as micron- and submicron-sized UHMWPE wear particles. In all cases, the material is phagocytosed more readily if it is coated with opsonins, which can increase the rate of phagocytosis several thousandfold [23]. It is important to note that UHMWPE adsorbs proteins readily; thus, UHMWPE wear particles can be opsonized and phagocytosed more rapidly in the body, and they can also adsorb complement molecules and activate the complement system.

Phagocytosis activates the macrophage, initiating the respiratory burst, production of a variety of lytic or proinflammatory chemicals. Many, including reactive oxygen and nitrogen species (ROS and RNS), as well as lysozyme and defensins, are antimicrobial or cytotoxic. These can be secreted both internally and externally, to kill both the ingested cell and any similarly-harmful cells located nearby; however, these species are indiscriminate, and cause localized damage to healthy tissue as well as infectious agents and tumors. Activated macrophages also secrete proinflammatory chemokines and cytokines, such as interleukins IL-1 and IL-6, tumor necrosis factor α (TNF-α), and prostaglandin E_2 (PGE_2). Some of these chemicals further upregulate the immune response in the activated macrophage; they also recruit and activate other nearby immune system cells, including other macrophages, fibroblasts, and osteoclasts, which are in fact a type of tissue-specific macrophage [22-24].

If the respiratory burst successfully digests the ingested material, then the immune response ends. However, none of the chemicals secreted by macrophages can break down UHMWPE particles. Instead, the particles remain inside the macrophages and continue to activate them, resulting in a condition called frustrated phagocytosis. Unable to destroy the UHMWPE particles, the macrophages continue to secrete chemokines and cytokines, upregulating the immune response in themselves and in neighboring cells and attracting additional macrophages and leukocytes, white blood cells which can differentiate into macrophages at the site of the inflammation. Clusters of activated macrophages also fuse into multinuclear foreign body giant cells, a classic marker of periprosthetic inflammation, and form granulomas, cyst-like masses of macrophages and multinuclear foreign body giant cells (also called polymorphonuclear cells) that replace nearby tissue, in this case bone [23, 25].

Macrophages undergoing frustrated phagocytosis, multinuclear giant cells, and granulomas all continue to release chemicals that promote localized tissue damage and continuation of the immune response, which becomes chronic due to the continuous reactivation. As in earlier stages, these chemicals include: i) high levels of cytotoxins such as reactive oxygen species that damage the surrounding bone and blood vessels, leading to further stimulation of the immune response; ii) matrix metalloproteinases (MMPs), which destroy the extracellular matrix of the nearby bone; and iii) proinflammatory cytokines such as TNF-α, PGE_2, and granulocyte-macrophage colony stimulating factor (GM-CSF) that further upregulate the immune response. MMPs and some proinflammatory cytokines also affect the behavior of both osteoblasts and osteoclasts, which is particularly damaging to bone.

Healthy bone consists of a balance between osteoblasts, which generate new bone tissue, and osteoclasts, which destroy existing bone tissue. The immune cascade caused by frustrated phagocytosis affects this balance in several ways, all of which lead to bone loss. IL-1, IL-6, TNF-α, PGE_2, and GM-CSF all promote macrophage differentiation into osteoclasts and upregulate osteoclast activity [22]. TNF-α also stimulates osteoblasts to produce PGE_2 [26], as well as IL-6 and GM-CSF [22], further promoting osteoclast differentiation and activation. In addition, Wang et al have found that exposure to titanium wear particles can suppress mesenchymal stem cell differentiation into osteoblasts, thereby reducing the osteoblast population around the hip implant [21]. In combination, the increase in osteoclast population and activity, along with a potential decrease in osteoblast population, results in bone loss around the implant.

Ultrahigh molecular weight polyethylene wear mechanisms

Since the majority of inflammatory wear particles originate from the UHMWPE acetabular cup, an obvious way to combat wear-mediated osteolysis is to reduce the wear rate of UHMWPE. This strategy requires an understanding of the mechanisms of UHMWPE wear. Due to the differences in contact stresses in hip and knee implants (less than 10 MPa versus up to 45 MPa, respectively), the wear behavior of the two systems is actually quite different. The lower contact stresses in the hip concentrate the stress near the surface, causing adhesive and abrasive wear mechanisms, along with surface microcracking, to predominate and generate smaller wear particles, while the higher contact stresses in the knee cause subsurface stress that produces delamination wear and correspondingly larger particles [12, 27].

Qualitatively, adhesive wear occurs when asperities on contacting surfaces briefly adhere and the asperity on the harder surface removes a small piece of material from the softer surface. This material either sticks to the hard countersurface to form a transfer film, or does not stick and becomes a loose wear particle. Quantitatively, adhesive wear is governed by a classic tribological relationship, Archard's Law, which predicts the wear volume V of a system based on the normal load L, the sliding distance x, the hardness H of the softer material, and a wear coefficient k based on the lubrication state of the system, as well as other factors [28]:

$$V_{adh} = k_{adh} \frac{Lx}{H} \quad [1].$$

Abrasive wear occurs as a result of harder material plowing into a softer surface. This can involve two-body wear from asperities on the harder bearing surface, or three-body wear from debris such as PMMA particles or pieces of bone. In either case, abrasive wear takes a form that is quantitatively similar to adhesive wear, but k_{abr} derives from plowing by an asperity or third-body particle at an angle θ [29]:

$$V_{abr} = \frac{\overline{\tan\theta}}{\pi} \frac{Lx}{H} = k_{abr} \frac{Lx}{H} \quad [2].$$

The wear coefficient is usually 10^{-6}-10^{-3} for adhesive wear and 10^{-3}-10^{-1} for abrasive wear [30]. When both processes occur simultaneously, the two equations can be combined into a more general relationship,

$$V = k \frac{Lx}{H} \quad [3].$$

Although forms of Equation 3 are often used to determine the wear factor of UHMWPE under various conditions, its validity has been questioned by a number of researchers due to conflicting reports on the effects of load and contact stress [31-33].

Wang et al have proposed several alternative wear models to account for factors such as contact stress [32] and crosslinking [34]; they also proposed that adhesion actually couples with fatigue to generate wear particles by a process of strain accumulation [27, 35]. Each wear cycle generates a small increment of plastic strain, which accumulates with repeated cycles until an asperity reaches a critical failure strain, which can be approximated by the elongation at break ε_u of the UHMWPE. In this model, the wear volume per walk cycle, ΔV, also depends on the load L, the average roughness R_a of the counterbearing (the femoral head), and the ultimate tensile strength σ_u of the UHMWPE:

$$\Delta V \propto L^{3/2} R_a^{3/2} \frac{1}{\sigma_u^{3/2} \varepsilon_u} \qquad [4].$$

Like Archard's Law, the wear volume in Equation 4 depends on the normal load and material properties of the softer surface. However, the dependence on the normal load is stronger (to a power of 1.5 rather than 1), which fits some experimental data more closely [35], and the critical material properties are different: ultimate stress and strain (essentially, toughness) rather than hardness. This is particularly interesting for polymers, which can be both tough and relatively soft. In addition, the sliding distance has been replaced by the number of cycles (to convert ΔV to V), indicating the wear pattern is more important than the wear distance.

Although the models are different, some factors in both are predetermined by the fact that the system under consideration is a total hip replacement. The normal load is dictated by the patient's body weight and cannot be changed without radically altering the geometry of the implant. The sliding distance and number of cycles depend on the patient's joint biomechanics and level of activity. The roughness of CoCr heads is already quite low (on the order of 0.05 μm or less [36]), and ceramics are even smoother;

therefore, the counterbearing roughness is unlikely to be further reduced. This leaves only the material properties and the wear coefficient as variables.

During the 1990s, the predominant approach to improving wear resistance of the total hip replacement system involved crosslinking the UHMWPE to hinder lamellar alignment in the polyethylene. Crosslinking produces covalent bonds between neighboring chains primarily in the amorphous region of the material [37]. These crosslinks should limit interlamellar slip and rotation, slowing or eliminating the processes shown in Figure 3 and thereby reducing orientation, strain hardening, and wear. Crosslinked UHMWPE is indeed more wear-resistant than uncrosslinked, or conventional, UHMWPE. In vitro, the wear rate was found to decrease with increasing crosslink density during pin-on-disk testing [38]; in vivo, a small study of retrieved acetabular cups showed that the crosslinked cups exhibited substantially lower wear rates than uncrosslinked cups of the same type [39].

However, the crosslinking process also generates free radicals, which must be neutralized (usually by melt-annealing above 137°C, the melting temperature of UHMWPE) to prevent oxidation and embrittlement. The combination of crosslinking and post-processing alters the microstructure of the UHMWPE, often lowering the crystallinity and reducing the size of the lamellae. These materials exhibit changes to their bulk mechanical properties, including decreased ultimate strength and strain [37] and fatigue crack inception [40]. As a result, crosslinked UHMWPE is more wear-resistant but less fatigue- and fracture-resistant than conventional UHMWPE. Recent clinical evidence indicates that this trade-off sometimes decreases the lifetime of total hip replacements: Tower et al [41] and Furmanski et al [42] have both reported on early

failures of THRs due to rim cracking of the crosslinked UHMWPE acetabular cups that was likely caused by a combination of design flaws – stress concentrations and overly thin cups – and reduced fracture toughness of the UHMWPE.

An alternative approach to improving UHMWPE wear resistance is to focus on the surface of the acetabular cup, rather than changing the bulk properties of the material. Surface modification alters either the material properties or lubrication state of the bearing, either increasing the hardness or toughness in Equations 3 and 4, or reducing the wear coefficient k.

A common surface modification is the amorphous carbon or diamond-like coating (DLC). Both consist of carbon and hydrogen, but amorphous carbon coatings contain predominantly sp^2 bonding, while diamond-like coatings are mainly sp^3. The hardness of these coatings varies widely, depending on both the carbon atom bonding state and the deposition method [43], but they are often used to harden UHMWPE [44, 45]. Interestingly, they are also applied to the ceramic or metal bearing surface, rather than to the UHMWPE [46]. This approach seems counterintuitive; further hardening the harder surface should not reduce the wear rate, and could in fact increase it if the coating formed a rougher surface than the uncoated polished bearing. However, amorphous carbon and diamond-like coatings are sometimes intended to improve the lubrication of the bearing, rather than the hardness. In many applications, coatings with primarily sp^2 bonding form graphite-like transfer films on the counterbearings, resulting in solid-lubricated graphite-on-graphite sliding. However, Hauert reported that other researchers have achieved mixed results in systems involving aqueous lubrication, and he questioned whether the intended graphitic transfer film could actually form in a joint replacement in vivo, as the

liberated particles could easily be washed away by synovial fluid instead of adhering permanently to the counterbearing [46].

An alternative approach to increasing lubrication at the UHMWPE-counterbearing interface is to increase hydrophilicity of the UHMWPE in order to improve retention of synovial fluid at the surface. UHMWPE itself is relatively hydrophobic, with a contact angle of approximately 90°. Widmer et al treated the UHMWPE surface with oxygen plasma to add hydrophilic chemical groups, such as hydroxyls or carbonyls [47]. This does increase the hydrophilicity of UHMWPE; Klapperich et al also found that oxygen plasma treatment reduced adhesion force [48]. However, oxygen plasma also oxidizes the UHMWPE surface, which can cause oxidative embrittlement and increased, rather than decreased, wear. Widmer et al also observed that the increased hydrophilicity of the surface was temporary, with the hydrophobicity of the surfacing returning over a period of hours to days.

A few researchers have investigated the addition of hydrophilic coatings to the UHMWPE surface. These coatings, called hydrogels, swell in the presence of water and can begin to mimic – on a very small scale – the action of articular cartilage, the hydrogel present on the surface of both bones articulating in natural, healthy joints (see Figure 1). Articular cartilage consists of four major components: linear collagen fibers, oriented based on location with respect to the bone; branched proteoglycans, charged molecules that form an interpenetrating network with the collagen; chondrocytes, cells that secrete extracellular matrix; and water, which hydrates the tissue and lubricates the surface. The negative charges on the proteoglycan molecules repel each other while attracting water from synovial fluid, which swells the cartilage and resists compression. However, the

fluid flows in and out of the material depending on its loading state. As load is applied, synovial fluid flows out of the cartilage and lubricates sliding; when the load is removed, the cartilage reabsorbs the synovial fluid.

Three groups have applied cartilage-like charged hydrogels to the surface of UHMWPE to improve lubrication (see Figure 6; the hyaluronan microcomposite is not shown). Pavoor et al sequentially dip-coated substrates with poly(acrylic acid) and poly(allylamine hydrochloride) to form polyelectrolyte multilayers (PEMs) that reduced the wear rate of UHMWPE during pin-on-disk testing [49]. However, like the diamond-like/amorphous carbon coatings, the PEMs lubricated sliding by forming wear particles and transfer films after delaminating from regions of contact. While this mechanism works well in continuous-contact, flow-free pin-on-disk tests, it may not be as effective in the body, where contact is intermittent and the flow of synovial fluid may wash lubricious PEM fragments away from the articulating interface.

Therefore, covalently-bonded lubricious coatings seem more promising for in vivo usage. Zhang et al generated hyaluronan coatings on sintered UHMWPE microcomposites and found that they significantly reduced the wear volume compared to uncoated UHMWPE, but the sintering method using during the coating process produced inferior quality UHMWPE [50]. This suggests that direct surface treatments, such as photopolymerization or plasma treatment, are preferable. Moro et al photopolymerized 2-methacryloyloxyethyl phosphorylcholine (MPC), a monomer similar to phospholipids found in cell membranes, onto UHMWPE to form a covalently-bonded brush layer on the surface [51]. This coating, which was previously shown to resist protein deposition [52], reduced the immunogenicity of 500 nm diameter polystyrene particles (used in place of

polyethylene particles) in both cell culture and an in vivo mouse calvarial model. In addition, the coating reduced the wear rate of crosslinked UHMWPE fourfold in a hip joint simulator, and it survived at least 3,000,000 load cycles.

The performance of the MPC surface provides strong proof of concept for the use of covalently-bonded hydrogel coatings to increase lubricity and decrease wear of UHMWPE. This work investigates the efficacy of a different coating material, poly(ethylene glycol) (PEG), which has been widely used for other biomedical applications. PEG was chosen for its hydrophilicity, lubricity, biocompatibility, and resistance to protein adsorption. Plasma treatment was chosen as the surface modification method because it produces coatings that are both covalently bonded to the substrate and internally crosslinked, rather than end-grafted in individual chains like the MPC brush layer (see Figure 6). Crosslinking is expected to increase the mechanical strength of the coating and improve wear resistance relative to a brush layer of similar chemical structure.

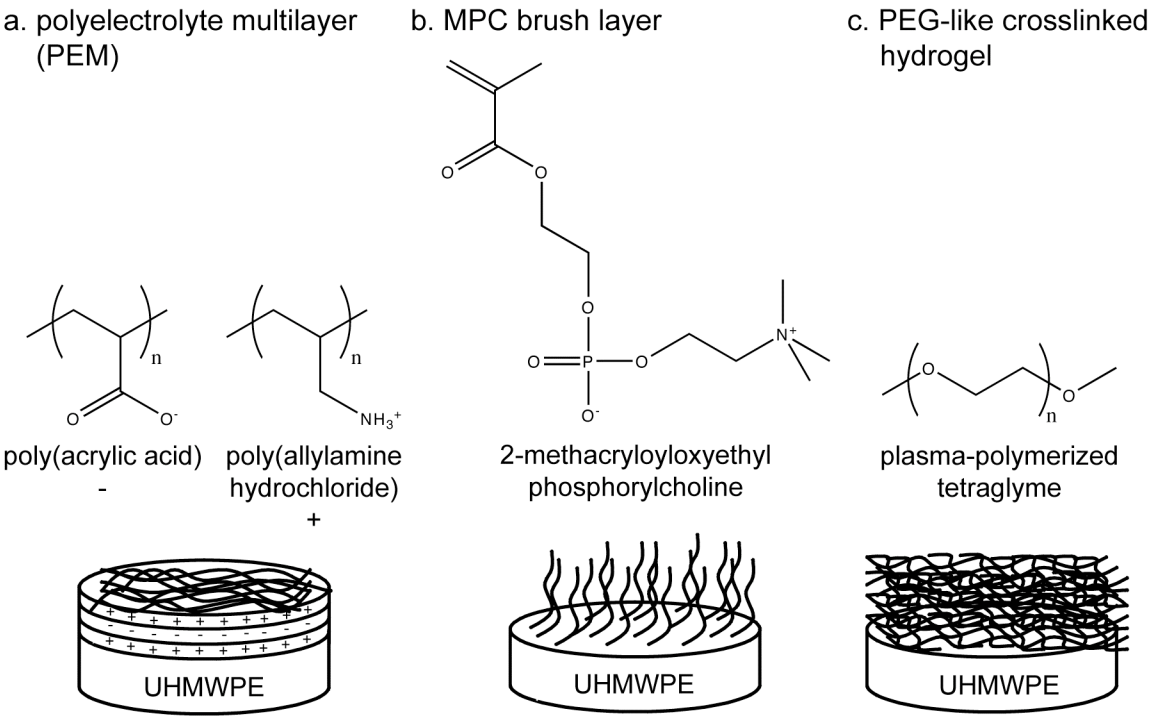

Figure 6: A comparison of the chemical structures and molecular architectures of PEM, MPC, and PEG-like coatings on UHMWPE. The PEM layer [49] is produced by dip coating, so it is adsorbed rather than chemically bonded to the UHMWPE surface. The MPC molecules [51] are photografted onto the UHMWPE surface, which forms covalent bonds to the UHMWPE surface by addition over the C-C double bond at the top of the molecule. The PEG-like layer, which is the focus of this thesis, is formed by plasma-polymerizing tetraglyme onto the surface to create a crosslinked polymer network that is also covalently bonded to the UHMWPE surface.

Poly(ethylene glycol)

Poly(ethylene glycol) (PEG), also known as polyethylene oxide (PEO), is a flexible linear polymer comprised of CH_2CH_2O repeat units (see Figure 7). PEG has been extensively studied for more than two decades because it is hydrophilic, biocompatible, and resistant to protein and cell deposition. Collectively, these traits render it attractive for a wide range of applications. In vivo, PEG is valued for its abilities (conferred by its resistance to protein deposition) to evade detection and uptake by the immune system, and to avoid deposition of infectious organisms such as bacteria.

This has led to several therapeutic applications: PEGylation of drugs, particularly peptides and proteins, to reduce antigenicity and enzymatic degradation, and to increase their half-life in the bloodstream [53, 54]; and PEG-coated liposomes, again to increase their half-life in the bloodstream [55, 56]. In vitro, PEG enables surface patterning and functionalization for cell and tissue culture studies. For example, proteins, peptides, and other biomolecules are often conjugated to PEGylated surfaces to present specific signals for behaviors such as attachment, spreading, proliferation, and differentiation [57, 58]. These functionalized surfaces offer potential as tissue engineering constructs for growing tissue in vitro or healing defects in vivo.

Since resistance to protein adsorption offers so many advantages, the basic science behind it has been studied extensively. Most work attempts to address one of two questions: what is the mechanism for resistance to protein adsorption, and which chemical structures confer the greatest resistance?

Although PEG has been known to resist protein adsorption since at least 1960 [59], and to decrease protein immunogenicity since at least 1977 [60], the bulk of PEG-related research did not begin until the 1990s. In 1991, Jeon et al published two seminal papers that modeled the energetics of the approach of a protein toward a polyethylene substrate coated with adsorbed PEG, focusing on three contributions: van der Waals attractions between the protein and the polyethylene surface, hydrophobic attraction between PEG and the protein, and steric stabilization causing repulsion due to compression of the PEG chains [61, 62].

Steric stabilization, a theory developed to explain the ability of hydrophilic polymers to stabilize hydrophobic particles as colloids in aqueous solutions, is based on a

thermodynamic argument that includes enthalpic and entropic components. Both involve separation of the hydrophobic particles, which would cluster without the polymer present. However, as two particles approach each other in the presence of a hydrophilic polymer, the particles compress the polymer. This leads to an unfavorable change in entropy as the number of possible conformations of the polymer are restricted, and to an unfavorable change in enthalpy if water in the polymer solvation shell is expelled into the bulk aqueous solution. The latter is often described in terms of an osmotic pressure: the concentration of water is lower in the solvation shell than in the bulk solution, so the osmotic gradient disfavors water leaving the solvation shell. The sum of the enthalpic and entropic energy expended during water removal exceeds the energy of the hydrophobic interactions driving the attraction between the two hydrophobic particles, so they remain separate. For protein-PEG interactions, protein – and sometimes a hydrophobic substrate below the PEG surface – serve as the hydrophobic particles.

Several interesting results emerged from the studies by Jeon et al, which attempted to identify the optimal surface density and chain length for protein resistance. First, they determined that the van der Waals attractions are an order of magnitude lower than the other forces, and could therefore be neglected. This meant that the protein resistance of the PEG coating depended only on the balance between steric repulsion away from the PEG chains and hydrophobic attraction to them. Second, the relative importance of surface density versus PEG chain length depended on how the protein is modeled [62], but in most cases, a fairly high optimum surface density coupled with long PEG chains yielded the most protein-resistance surfaces.

Finally, Jeon et al also found that the hydrophobic interactions depended on the refractive index of the polymer, with a lower index of refraction decreasing the force of attraction. This somewhat unintuitive relationship results from the fact that hydrophobic interactions arise from induced dipoles in the hydrophobic portions of the protein and PEG molecules. The magnitude of the dipoles is related to the dielectric response of the protein, the PEG, and the medium between them, and the dielectric response depends on the refractive indices of all three materials [63]. Jeon et al consequently suggested that the unusually high protein resistance of PEG is conferred by its relatively low refractive index (given here as 1.456, the value for low molecular weight species; higher molecular weight species have a refractive index of 1.51-1.54 [64]) [61].

While Jeon et al successfully modeled a realistic scenario of long-chain PEG polymers adsorbed on a substrate, such systems are not ideal for experimental purposes because they often do not allow for sufficient control over the surface chemistry, density, or PEG layer thickness. Consequently, model surfaces were developed to mimic PEG-protein interactions. The predominant type of model system consists of self-assembled monolayers (SAMs), short oligomers that spontaneously adsorb to certain substrates to form well-controlled, ordered surfaces. The most common SAMs possess an alkanethiol (R-SH) group at one end, which adsorbs readily to gold and silver substrates. The bodies of the molecules consist of an oligomer with a hydrocarbon spacer unit at the alkanethiol end, and can be terminated with a head group of choice at the free end (see Figure 7). This structure enables a high degree of control over the surface chemistry and thickness, while the gold and silver substrates allows for some control over molecular conformation

and density, as well as the use of highly sensitive techniques such as surface plasmon resonance (SPR) [65] to measure protein deposition in nanogram quantities.

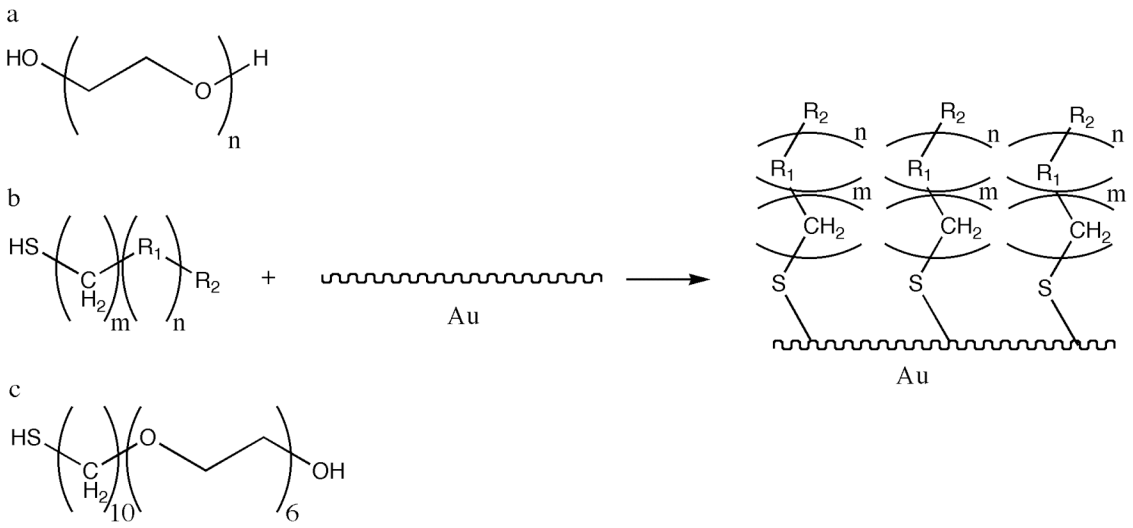

Figure 7: a) Poly(ethylene glycol); n is usually in the tens or hundreds. b) The most general chemical structure of an alkanethiol (left) used to generate a self-assembled monolayer (right). For these alkanethiols, m is usually 1-20 and n is 0-20. R_1 represents the chemical structure of the monomer of interest, often ethylene glycol or a sugar, and R_2 represents the head group: OH, OCH_3, COOH, etc. An extremely comprehensive set of alkanethiols appears in [66]. c) A typical oligo(ethylene glycol) alkanethiol.

Just a few months after the theoretical studies from Jeon et al, Prime and Whitesides established the validity of SAMs as model surfaces for protein adsorption studies in another seminal paper [67]. This work confirmed that, as expected from long-chain experiments with PEG, SAMs comprised of ethylene glycol oligomers (in this case, n=6) could prevent the deposition of five different proteins. The study, which compared single-component and mixed SAMs based on ethylene glycol, maltose, decane, and decanol, also used contact angle measurements to offer limited experimental evidence that increasing surface hydrophilicity reduced protein adsorption. The authors therefore concluded that adsorption was related to hydrophobic interactions.

Subsequent SAMs and PEG research continued to address both the mechanistic and chemical aspects of protein resistance. During the 1990s and early 2000s, a number of groups investigated the effect of surface chemistry on protein deposition. These studies ranged from relatively simple comparisons of hydroxy- versus methoxy-terminated oligo(ethylene glycol) (OEG) SAMs [68, 69] to mixtures of oligo(ethylene glycol) and hydrocarbon SAMs [65, 67, 69] to evaluations of the protein resistance of more complicated chemical structures such as long-chain polysaccharides [70] and sugar alcohol-terminated SAMs [71]. In 2001, Ostuni et al performed an exhaustive study of SAMs end group chemistries, including several hydrophobic groups, various ethylene glycol derivatives, amines, amides, crown ethers, sugars, nitriles, and other species [66]. Many of the SAMs studies also evaluated the effect of chain length of the hydrocarbon [71] and/or ethylene glycol (or other functional group) [66, 68, 69] segments on protein resistance.

In general, these studies concluded that, while slight variations in the surface chemistry such as termination in –OH versus $–OCH_3$ have minimal effect, increasing the hydrophobicity of the OEG surfaces by increasing the mole fraction of hydrocarbon alkanethiol increases protein adsorption. Increasing the length of the ethylene glycol segment does not affect protein adsorption in single-component SAMs, but can decrease adsorption in mixed hydrophobic/hydrophilic SAMs, when the mole fraction of the ethylene-glycol-containing is low enough. Combined, these observations support the theory of Jeon et al that hydrophobic attraction between proteins and PEG promote protein adsorption.

Based on their extensive survey of alternative chemical structures [66], Ostuni et al reported four molecular characteristics common to SAMs components that resisted protein deposition: i) hydrophilicity, ii) presence of hydrogen bond acceptors, iii) absence of hydrogen bond donors, and iv) charge neutrality. All of these concepts had appeared in prior studies [70-72], though never in full combination, and the second and third criteria seem contradictory. Hydrogen bonding increases hydrophilicity, and it is difficult to explain why surfaces containing hydrogen bond acceptors would behave differently than hydrogen bond donors. It is perhaps unsurprising, then, that Luk et al found that SAMs containing hydrogen-bond-donating mannitol groups rather than ethylene glycol resisted protein deposition and cell attachment [71]. However, the first and last characteristics from Ostuni et al agree readily with Jeon et al (like the refractive index, charge affects the dielectric response of the material).

By the late 1990s, a significant body of literature regarding chemical structure-function relationships of oligo(ethylene glycol) and related molecules had accumulated. Harder et al chose a new direction: investigating the effect of molecular conformation in addition to chemical structure [73]. In this study, three different oligo(ethylene glycol) SAMs (EG_3-OCH_3, EG_6-OCH_3, and a slightly branched EG_3[3,1]-OCH_3) were adsorbed on both gold and silver substrates, and the molecular conformation of the alkane and ethylene glycol regions, as well as the protein deposition resistance of each surface, were quantified by Fourier transform infrared reflection absorption spectroscopy (FTIRAS). The study demonstrated that molecular conformation was more important than surface chemistry in determining resistance to protein adsorption. Like EG_6-OCH_3 on both substrates, EG_3-OCH_3 packed into a helical configuration with predominantly *gauche*

bond conformations on gold. However, on silver, EG_3-OCH_3 formed a more densely packed, planar structure with predominantly *trans* bonds – and lost its protein resistance, which the helical molecules all exhibited. (*Gauche* and *trans* refer to two possibilities for the relative rotation of the bulkiest groups on adjacent carbon atoms. *Gauche* groups are next to one another and can therefore repel each other, lowering the packing density of the molecules and increasing water uptake in the OEGs. *Trans* groups are opposite each other and too far apart to interact in most cases; therefore, mostly-*trans* OEGs pack more densely and absorb less water than mostly-*gauche* OEGs.) EG_3[3,1]-OCH_3, which possessed enough branching to preclude ordered molecular packing, exhibited an amorphous molecular conformation, but still resisted protein deposition like the helical SAMs.

The investigation of molecular conformation can be viewed as a bridge between experimental studies and molecular modeling, which attempts to predict low-energy (and therefore probable) conformations for molecules based on different theories of inter- and intra-molecular interactions. With computational power increasing steadily throughout the 1990s, such studies became increasingly viable. Consequently, after the work from Harder et al, some theorists focused on molecular modeling to examine the interactions between ethylene glycol, water, and proteins.

A trio of papers published in 2000 employed three complementary approaches: *ab initio* modeling of a single oligo(ethylene glycol) molecule interacting with 1-3 water molecules [74]; Grand canonical Monte Carlo simulation of 36 oligo(ethylene glycol) SAMs interacting with up to 1000 water molecules [75]; and experimental probing of the structure of oligo(ethylene glycol) SAMs in air and water using sum frequency

generation (SFG), a technique that determines surface/interface chemistry, and to some extent, orientation [76]. The studies assumed that penetration of water into the OEG layer and hydrogen bonding between water and the oxygen atoms in the OEG layer indicates that the surfaces would resist protein deposition due to entropic (osmotic) considerations.

The three studies agreed well with each other, and to a large extent, with Harder et al. *Ab initio* modeling indicated that hydrogen bonding between the oxygen atoms in the oligo(ethylene glycol) and the hydrogens of the water molecules was most energetically favorable when the OEG took on an all-*gauche* structure similar but not identical to the helical conformation, indicating that the *gauche* structure adsorbed water more readily than the *trans*. The Grand canonical Monte Carlo simulation found that water molecules penetrated into the helical (mostly-*gauche*) OEG SAMs much more deeply than into the *trans* SAM and, as in the *ab initio* model, hydrogen-bonded to the helical OEG oxygens to a much higher degree. In addition, penetration of the water molecules into the helical SAM surface caused the SAMs to lose their regular conformations and become more disordered and amorphous; this did not occur in the *trans* SAMs. The SFG experiments by Zolk et al examined the surface of EG_3-OCH_3 on gold (which Harder et al had found to be helical and protein-resistant [73]) in air and water. In air, the terminal methyl groups of the ethylene glycol moiety were oriented, but the addition of water caused them to lose their orientation and become amorphous, as the Monte Carlo simulations predicted; the SFG results also supported the predictions that water would penetrate into the OEG region of the molecules and form hydrogen bonds with the oxygen atoms there.

The amorphization of the OEG layer upon exposure to water suggests that the helical conformation observed by Harder et al may have been an experimental artifact caused by performing the FTIRAS measurements in air. This explains why the amorphous branched EG_3[3,1]-OCH_3 resisted protein deposition as effectively as the "helical" conformation: the two likely became conformationally similar upon exposure to water.

The fact that amorphous OEGs adsorb and hydrogen bond to water well may explain why a different class of ethylene-glycol-based surfaces also resist protein deposition. Coatings formed by plasma polymerization of oligo(ethylene glycol) monomers that resisted protein and cell deposition were first reported by Lopez et al in 1992 [77] and have been of interest ever since. A 1996 follow-up study examined the effects of various plasma processing parameters, such as power, flow rate and temperature, on the chemistry of coatings produced from methyl ether (CH_3-O-CH_3), mono-, di-, and triglyme (CH_3O-$(CH_2CH_2O)_n$-CH_3, where n=1, 2, and 3, respectively) and found that lower plasma power and temperature produced more PEG-like surfaces. At the lower temperature studied, increasing the size of the monomer also led to more PEG-like surfaces [78]. Johnston et al investigated the effect of monomer chemistry, including mono- through tetraglyme (n=1-4), dioxane, and two crown ethers, on coating composition and resistance to protein deposition, and found that all monomers except dioxane produced surfaces containing at least 50% ether. Among these, the surfaces generated from tetraglyme (see Figure 8) and the crown ethers had the highest ether content and low fibrinogen (protein) adsorption; the tetraglyme-based surfaces also

generally exhibited lower fibrinogen retention, indicating that tetraglyme produced highly PEG-like and generally protein resistant surfaces [79].

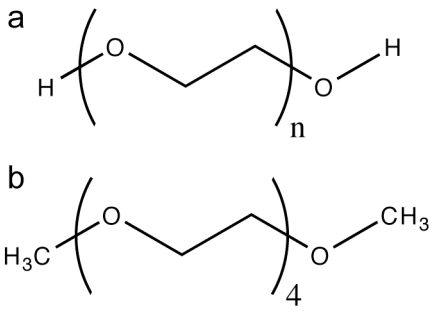

Figure 8: The chemical structures of a) poly(ethylene glycol) and b) tetraglyme.

Subsequent studies focused on the protein resistance of and biological response to plasma-polymerized tetraglyme surfaces. Shen et al determined that high ether content (~70%) and oxygen-to-carbon ratio (O:C > 0.40) correlated to low protein and cell deposition, while high hydrocarbon content correlated to high protein and cell deposition [80], while Cao et al reported that extremely low protein adsorption (< 5 ng/cm^2) on tetraglyme-based surfaces with at least 66% ether [81]. These results agree well with each other, and with the concept of hydrophobicity-modulated interactions between proteins and PEG surfaces.

In vitro, Cao et al found that polyethylene tubing coated with plasma-polymerized tetraglyme exhibited reduced platelet adhesion and thrombin compared to uncoated polyethylene, polyurethane, and Silastic; ex vivo, in a sheep carotid artery shunt, the tetraglyme surface greatly reduced platelet adhesion and prevented platelet aggregation compared to uncoated, heparin coated, and chromic acid etched polyethylene [82]. A follow-up in vitro study yielded similar findings, with tetraglyme-treated surfacing

exhibiting reduced protein adhesion and thrombus accumulation, as well as increased clotting time, compared to untreated controls [83].

By contrast, Shen et al observed in 2002 that tetraglyme-based surfaces resisted leukocyte adhesion less than the uncoated fluorinated ethylene propylene control in an in vivo mouse model [84], a result that conflicts with the bulk of published in vitro studies involving PEG, oligo(ethylene glycol) SAMs, and tetraglyme-based surfaces. Due to the greater complexity of the in vivo environment, it is not unusual for in vivo results to differ from in vitro data; however, the study from Shen et al highlights the fact that, despite the substantial body of literature regarding the protein resistance of PEG and PEG-like molecules, in vivo studies are necessary to validate their use for implantation.

Dissertation outline

This study focuses on the chemistry, in vitro protein resistance, and wear behavior of a PEG-like coating on UHMWPE. In order to covalently bond the PEG coating to the UHMWPE surface, which does not have reactive chemical groups, and to generate crosslinked rather than linear PEG, the UHWMPE surfaces were plasma treated with a PEG-like oligomer, tetraglyme (see Chapter 3). The resulting surfaces were chemically characterized by ATR-FTIR, XPS, and contact angle goniometry (Chapter 4). Resistance to protein deposition was measured by exposing the surfaces to fluorescently-labeled albumin and imaging the deposited protein using fluorescence microscopy (Chapter 4). Atomic force microscopy was used to measure the thickness of the coatings (Chapter 5) and to model asperity wear in order to evaluate the micron-scale wear mechanisms of the coatings (Chapter 6). Pin-on-disk tribotesting evaluated the lifetime of the coatings at the

macroscopic (millimeter) scale, and the worn surfaces were further examined by ATR-FTIR to determine the wear behavior of the coatings at the mesoscale of tens of microns (Chapter 6). These experiments evaluated the effects of PEG-like coating chemistry and thickness on wear behavior at three scales, and they provide a preliminary assessment of the expected lifetime of the coatings under a range of clinically-relevant wear conditions.

References

1. Agency for Healthcare Research and Quality, *http://hcup.ahrq.gov*. Viewed 31 March 2008.
2. Centers for Disease Control, *http://www.cdc.gov/nchs/fastats/lifexpec.htm*. Viewed 31 March 2008.
3. http://uuhsc.utah.edu/healthinfo/images/ei_0244.gif. Viewed 11 March 2008.
4. Smith & Nephew, *http://www.hipreplacementinfo.com/hip/treatmentoptions/hipreplacement/hip_replacement_material_and_technology.cfm*. Viewed 11 March 2008.
5. Callaghan, J.J., A.G. Rosenberg, and H.E. Rubash, eds. *The Adult Hip*. 2nd ed. Vol. 1. 2007, Lippincott Williams & Wilkins: Philadelphia.
6. Kurtz, S.M., *The UHMWPE Handbook: ultra-high molecular weight polyethylene in total joint replacement*. 2004, Boston: Elsevier Academic Press.
7. Turell, M., A.G. Wang, and A. Bellare, *Quantification of the effect of cross-path motion on the wear rate of ultra-high molecular weight polyethylene.* Wear, 2003. **255**: p. 1034-1039.

8. Boontongkong, Y., et al., *Orientation of plane strain-compressed ultrahigh-molecular-weight polyethylene.* Polymer, 1998. **39**(25): p. 6391-6400.

9. Oleinik, E.F., *Plasticity of Semicrystalline Flexible-Chain Polymers at the Microscopic and Mesoscopic Levels.* Polymer Science Series C, 2003. **45**(1): p. 17-117.

10. Galeski, A., et al., *Morphological Alterations During Texture-Producing Plastic Plane-Strain Compression of High-Density Polyethylene.* Macromolecules, 1992. **25**(21): p. 5705-5718.

11. Wang, A., et al., *Orientation softening in the deformation and wear of ultra-high molecular weight polyethylene.* Wear, 1997. **203**: p. 230-241.

12. Wang, A., C. Stark, and J.H. Dumbleton, *Mechanistic and morphological origins of ultra-high molecular weight polyethylene wear debris in total joint replacement prostheses.* Proceedings of the Institution of Mechanical Engineers Part H-Journal of Engineering in Medicine, 1996. **210**: p. 141-155.

13. Davey, S.M., et al., *Measurement of molecular orientation in retrieved ultra-high-molecular-weight polyethylene (UHMWPE) hip sockets using Fourier-transform infrared spectroscopy.* Strain, 2004. **40**(4): p. 203-210.

14. Edidin, A.A., et al., *Plasticity-induced damage layer is a precursor to wear in radiation-cross-linked UHMWPE acetabular components for total hip replacement.* Journal of Arthroplasty, 1999. **14**(5): p. 616-627.

15. Schmalzried, T.P. and J.J. Callaghan, *Wear in total hip and knee replacements.* Journal of Bone and Joint Surgery-American Volume, 1999. **81A**(1): p. 115-136.

16. Harris, W.H., *Osteolysis and Particle Disease in Hip-Replacement - a Review.* Acta Orthopaedica Scandinavica, 1994. **65**(1): p. 113-123.

17. Maloney, W.J., et al., *Endosteal Erosion in Association with Stable Uncemented Femoral Components.* Journal of Bone and Joint Surgery-American Volume, 1990. **72A**(7): p. 1025-1034.

18. Maloney, W.J., et al., *Severe Osteolysis of the Pelvis in Association with Acetabular Replacement without Cement.* Journal of Bone and Joint Surgery-American Volume, 1993. **75A**(11): p. 1627-1635.

19. Schmalzried, T.P., M. Jasty, and W.H. Harris, *Periprosthetic Bone Loss in Total Hip-Arthroplasty - Polyethylene Wear Debris and the Concept of the Effective Joint Space.* Journal of Bone and Joint Surgery-American Volume, 1992. **74A**(6): p. 849-863.

20. Campbell, N.A., J.B. Reece, and L.G. Mitchell, *Biology*. 5th ed. 1999, Menlo Park, CA: Benjamin/Cummings.

21. Wang, M.L., P.F. Sharkey, and R.S. Tuan, *Particle bioreactivity and wear-mediated osteolysis.* Journal of Arthroplasty, 2004. **19**(8): p. 1028-1038.

22. Archibeck, M.J., et al., *The basic science of periprosthetic osteolysis.* Journal of Bone and Joint Surgery-American Volume, 2000. **82A**(10): p. 1478-1489.

23. Goldsby, R.A., T.J. Kindt, and B.A. Osborne, *Kuby Immunology*. 4 ed. 2000, New York: W. H. Freeman and Company.

24. Ingham, E. and J. Fisher, *Biological reactions to wear debris in total joint replacement.* Proceedings of the Institution of Mechanical Engineers Part H-Journal of Engineering in Medicine, 2000. **214**(H1): p. 21-37.

25. Konttinen, Y.T., et al., *The microenvironment around total hip replacement prostheses.* Clinical Orthopaedics and Related Research, 2005. **430**: p. 28-38.

26. Goodman, S.B., et al., *In vitro, in vivo, and tissue retrieval studies on particulate debris.* Clinical Orthopaedics and Related Research, 1998(352): p. 25-34.

27. Wang, A., et al., *Wear Mechanisms of UHMWPE in Total Joint Replacements.* Wear, 1995. **181**: p. 241-249.

28. Archard, J.F., *Contact and Rubbing of Flat Surfaces.* Journal of Applied Physics, 1953. **24**(8): p. 981-988.

29. Rabinowicz, E., *Friction and Wear of Materials*. 1965, New York: John Wiley and Sons.

30. Komvopoulos, K., *Fundamentals of Tribology and Contact Mechanics (lecture notes)*. 2005, Berkeley, CA: University of California, Berkeley.

31. Vassiliou, K. and A. Unsworth, *Is the wear factor in total joint replacements dependent on the nominal contact stress in ultra-bigh molecular weight polyethylene contacts?* Proceedings of the Institution of Mechanical Engineers Part H-Journal of Engineering in Medicine, 2004. **218**(H2): p. 101-107.

32. Wang, A., A. Essner, and R. Klein, *Effect of contact stress on friction and wear of ultra-high molecular weight polyethylene in total hip replacement.* Proceedings of the Institution of Mechanical Engineers Part H-Journal of Engineering in Medicine, 2001. **215**(H2): p. 133-139.

33. Barbour, P.S.M., D.C. Barton, and J. Fisher, *The Influence of Contact Stress on the Wear of Uhmwpe for Total Replacement Hip Prostheses.* Wear, 1995. **181**: p. 250-257.

34. Wang, A., *A unified theory of wear for ultra-high molecular weight polyethylene in multi-directional sliding.* Wear, 2001. **248**(1-2): p. 38-47.

35. Wang, A., C. Stark, and J.H. Dumbleton, *Role of Cyclic Plastic-Deformation in the Wear of UHMWPE Acetabular Cups.* Journal of Biomedical Materials Research, 1995. **29**(5): p. 619-626.

36. McKellop, H.A., et al., *The Origin of Submicron Polyethylene Wear Debris in Total Hip-Arthroplasty.* Clinical Orthopaedics and Related Research, 1995(311): p. 3-20.

37. Ries, M.D. and L. Pruitt, *Effect of cross-linking on the microstructure and mechanical properties of utra-high molecular weight polyethylene.* Clinical Orthopaedics and Related Research, 2005(440): p. 149-156.

38. Muratoglu, O.K., et al., *Unified wear model for highly crosslinked ultra-high molecular weight polyethylenes (UHMWPE).* Biomaterials, 1999. **20**(16): p. 1463-1470.

39. Oonishi, H., E. Tsuji, and Y.Y. Kim, *Retrieved total hip prostheses - Part I - The effects of cup thickness, head sizes and fusion defects on wear.* Journal of Materials Science-Materials in Medicine, 1998. **9**(7): p. 393-401.

40. Baker, D.A., A. Bellare, and L. Pruitt, *The effects of degree of crosslinking on the fatigue crack initiation and propagation resistance of orthopedic-grade polyethylene.* Journal of Biomedical Materials Research Part A, 2003. **66A**(1): p. 146-154.

41. Tower, S.S., et al., *Rim cracking of the cross-linked longevity polyethylene acetabular liner after total hip arthroplasty.* Journal of Bone and Joint Surgery-American Volume, 2007. **89A**(10): p. 2212-2217.

42. Furmanski, J., et al., *Fracture of highly cross-linked UHMWPE acetabular liners.* Journal of Bone and Joint Surgery-American Volume, 2008. **submitted**.

43. Sedlacek, M., B. Podornik, and J. Vizintin, *Tribological properties of DLC coatings and comparison with test results: Development of a database.* Materials Characterization, 2008. **59**(2): p. 151-161.

44. Bertoti, I., et al., *Nitrogen-PBII modification of ultra-high molecular weight polyethylene: Composition, structure and nanomechanical properties.* Surface & Coatings Technology, 2007. **201**(15): p. 6839-6842.

45. Marcondes, A.R., et al., *Improvements of ultra-high molecular weight polyethylene mechanical properties by nitrogen plasma immersion ion implantation.* Brazilian Journal of Physics, 2004. **34**(4B): p. 1667-1672.

46. Hauert, R., *A review of modified DLC coatings for biological applications.* Diamond and Related Materials, 2003. **12**(3-7): p. 583-589.

47. Widmer, M.R., et al., *Influence of polymer surface chemistry on frictional properties under protein-lubrication conditions: implications for hip-implant design.* Tribology Letters, 2001. **10**(1-2): p. 111-116.

48. Klapperich, C., L. Pruitt, and K. Komvopoulos, *Nanomechanical properties of energetically treated polyethylene surfaces.* Journal of Materials Research, 2002. **17**(2): p. 423-430.

49. Pavoor, P.V., et al., *Wear reduction of orthopaedic bearing surfaces using polyelectrolyte multilayer nanocoatings.* Biomaterials, 2006. **27**(8): p. 1527-1533.

50. Zhang, M., et al., *A novel ultra high molecular weight polyethylene-hyaluronan microcomposite for use in total joint replacements. II. Mechanical and tribological property weight composite for evaluation.* Journal of Biomedical Materials Research Part A, 2007. **82A**(1): p. 18-26.

51. Moro, T., et al., *Surface grafting of artificial joints with a biocompatible polymer for preventing periprosthetic osteolysis.* Nature Materials, 2004. **3**(11): p. 829-836.

52. Ishihara, K., et al., *Photoinduced graft polymerization of 2-methacryloyloxyethyl phosphorylcholine on polyethylene membrane surface for obtaining blood cell adhesion resistance.* Colloids and Surfaces B-Biointerfaces, 2000. **18**(3-4): p. 325-335.

53. Roberts, M.J., M.D. Bentley, and J.M. Harris, *Chemistry for peptide and protein PEGylation.* Advanced Drug Delivery Reviews, 2002. **54**(4): p. 459-476.

54. Caliceti, P. and F.M. Veronese, *Pharmacokinetic and biodistribution properties of poly(ethylene glycol)-protein conjugates.* Advanced Drug Delivery Reviews, 2003. **55**(10): p. 1261-1277.

55. Allen, T.M., *The Use of Glycolipids and Hydrophilic Polymers in Avoiding Rapid Uptake of Liposomes by the Mononuclear Phagocyte System.* Advanced Drug Delivery Reviews, 1994. **13**(3): p. 285-309.

56. Gref, R., et al., *'Stealth' corona-core nanoparticles surface modified by polyethylene glycol (PEG): influences of the corona (PEG chain length and*

surface density) and of the core composition on phagocytic uptake and plasma protein adsorption. Colloids Surf B Biointerfaces, 2000. **18**(3-4): p. 301-313.

57. Bearinger, J.P., D.G. Castner, and K.E. Healy, *Biomolecular modification of p(AAm-co-EG/AA) IPNs supports osteoblast adhesion and phenotypic expression.* Journal of Biomaterials Science-Polymer Edition, 1998. **9**(7): p. 629-652.

58. Desai, T.A., *Micro- and nanoscale structures for tissue engineering constructs.* Medical Engineering & Physics, 2000. **22**(9): p. 595-606.

59. Dowben, R.M., et al., *Direct ion-exchange chromatography of tissue extracts without precipitation of protein by use of non-ionic detergents.* Biochimica et Biophysica Acta, 1960. **43**: p. 338-341.

60. Abuchowski, A., et al., *Alteration of immunological properties of bovine serum albumin by covalent attachment of polyethylene glycol.* J. Biol. Chem., 1977. **252**(11): p. 3578-3581.

61. Jeon, S.I. and J.D. Andrade, *Protein Surface Interactions in the Presence of Polyethylene Oxide .2. Effect of Protein Size.* Journal of Colloid and Interface Science, 1991. **142**(1): p. 159-166.

62. Jeon, S.I., et al., *Protein Surface Interactions in the Presence of Polyethylene Oxide .1. Simplified Theory.* Journal of Colloid and Interface Science, 1991. **142**(1): p. 149-158.

63. Adamson, A.W. and A.P. Gast, *Physical Chemistry of Surfaces*. 6th ed. 1997, New York: John Wiley & Sons, Inc.

64. Brandrup, J., et al., eds. *Polymer Handbook*. 4th ed. 1999, John Wiley & Sons, Inc.: New York.

65. Mrksich, M., G.B. Sigal, and G.M. Whitesides, *Surface-Plasmon Resonance Permits in-Situ Measurement of Protein Adsorption on Self-Assembled Monolayers of Alkanethiolates on Gold.* Langmuir, 1995. **11**(11): p. 4383-4385.

66. Ostuni, E., et al., *A survey of structure-property relationships of surfaces that resist the adsorption of protein.* Langmuir, 2001. **17**(18): p. 5605-5620.

67. Prime, K.L. and G.M. Whitesides, *Self-Assembled Organic Monolayers - Model Systems for Studying Adsorption of Proteins at Surfaces.* Science, 1991. **252**(5009): p. 1164-1167.

68. Prime, K.L. and G.M. Whitesides, *Adsorption of Proteins onto Surfaces Containing End-Attached Oligo(Ethylene Oxide) - a Model System Using Self-Assembled Monolayers.* Journal of the American Chemical Society, 1993. **115**(23): p. 10714-10721.

69. Chapman, R.G., et al., *Preparation of mixed self-assembled monolayers (SAMs) that resist adsorption of proteins using the reaction of amines with a SAM that presents interchain carboxylic anhydride groups.* Langmuir, 2000. **16**(17): p. 6927-6936.

70. Osterberg, E., et al., *Comparison of Polysaccharide and Poly(Ethylene Glycol) Coatings for Reduction of Protein Adsorption on Polystyrene Surfaces.* Colloids and Surfaces a-Physicochemical and Engineering Aspects, 1993. **77**(2): p. 159-169.

71. Luk, Y.Y., M. Kato, and M. Mrksich, *Self-assembled monolayers of alkanethiolates presenting mannitol groups are inert to protein adsorption and cell attachment.* Langmuir, 2000. **16**(24): p. 9604-9608.

72. Deng, L., M. Mrksich, and G.M. Whitesides, *Self-assembled monolayers of alkanethiolates presenting tri(propylene sulfoxide) groups resist the adsorption of protein.* Journal of the American Chemical Society, 1996. **118**(21): p. 5136-5137.

73. Harder, P., et al., *Molecular conformation in oligo(ethylene glycol)-terminated self-assembled monolayers on gold and silver surfaces determines their ability to resist protein adsorption.* Journal of Physical Chemistry B, 1998. **102**(2): p. 426-436.

74. Wang, R.L.C., H.J. Kreuzer, and M. Grunze, *The interaction of oligo(ethylene oxide) with water: a quantum mechanical study.* Physical Chemistry Chemical Physics, 2000. **2**(16): p. 3613-3622.

75. Pertsin, A.J. and M. Grunze, *Computer simulation of water near the surface of oligo(ethylene glycol)-terminated alkanethiol self-assembled monolayers.* Langmuir, 2000. **16**(23): p. 8829-8841.

76. Zolk, M., et al., *Solvation of oligo(ethylene glycol)-terminated self-assembled monolayers studied by vibrational sum frequency spectroscopy.* Langmuir, 2000. **16**(14): p. 5849-5852.

77. Lopez, G.P., et al., *Glow-Discharge Plasma Deposition Of Tetraethylene Glycol Dimethyl Ether For Fouling-Resistant Biomaterial Surfaces.* Journal Of Biomedical Materials Research, 1992. **26**(4): p. 415-439.

78. Lopez, G.P. and B.D. Ratner, *Molecular Adsorption and the Chemistry of Plasma-Deposited Thin Organic Films: Deposition of Oligomers of Ethylene Glycol.* Plasmas and Polymers, 1996. **1**(2).

79. Johnston, E.E., J.D. Bryers, and B.D. Ratner, *Plasma deposition and surface characterization of oligoglyme, dioxane, and crown ether nonfouling films.* Langmuir, 2005. **21**(3): p. 870-881.

80. Shen, M.C., et al., *Multivariate surface analysis of plasma-deposited tetraglyme for reduction of protein adsorption and monocyte adhesion.* Langmuir, 2003. **19**(5): p. 1692-1699.

81. Cao, L., B.D. Ratner, and T.A. Horbett, *Plasma deposition of tetraglyme inside small diameter tubing: Optimization and characterization.* Journal of Biomedical Materials Research Part A, 2007. **81A**(1): p. 12-23.

82. Cao, L., et al., *Glow discharge plasma treatment of polyethylene tubing with tetraglyme results in ultralow fibrinogen adsorption and greatly reduced platelet adhesion.* Journal of Biomedical Materials Research Part A, 2006. **79A**(4): p. 788-803.

83. Cao, L., et al., *Plasma-deposited tetraglyme surfaces greatly reduce total blood protein adsorption, contact activation, platelet adhesion, platelet procoagulant activity, and in vitro thrombus deposition.* Journal of Biomedical Materials Research Part A, 2007. **81A**(4): p. 827-837.

84. Shen, M.C., et al., *PEO-like plasma polymerized tetraglyme surface interactions with leukocytes and proteins: in vitro and in vivo studies.* Journal of Biomaterials Science-Polymer Edition, 2002. **13**(4): p. 367-390.

Chapter 2

Introduction to Methodology and Instrumentation

Introduction

This project involves three steps: production, characterization, and tribological testing of the PEG-like coating on UHMWPE substrates. Each step requires different instrumentation, including a plasma deposition system to generate the coating, several different surface chemical analysis methods (x-ray photoelectron spectroscopy, attenuated total reflection Fourier transform infrared spectroscopy, contact angle goniometry, and protein deposition), and two tribological testing systems (the atomic force microscope and the pin-on-disk wear tester). In addition, ANOVA was performed on several data sets to establish the effect of various plasma deposition parameters. This chapter provides a short introduction to each instrument/technique, including the basic principles of operation, the relevant type(s) of information provided, and the analysis methods employed during this project.

Plasma deposition

Plasma treatment systems are used to modify the surface of a substrate. At their simplest, plasma systems consist of a chamber and a power source; many systems also involve a vacuum pump used to evacuate the chamber, as well as intake valves to introduce gases used during surface treatment, and an electric field to facilitate transport of plasma species to the substrate surface. The substrate is placed within the chamber, the vacuum pump removes the air, the desired gas is introduced into the chamber, and the power source adds energy to the gas. This creates energetic species – ions, free radicals, and excited neutral atoms or molecules – that can modify the surface of the substrate in several different ways, depending on the power of the plasma, the chemical species it contains, and various other factors [1]. The reactor setup used in these experiments is shown in Figure 1.

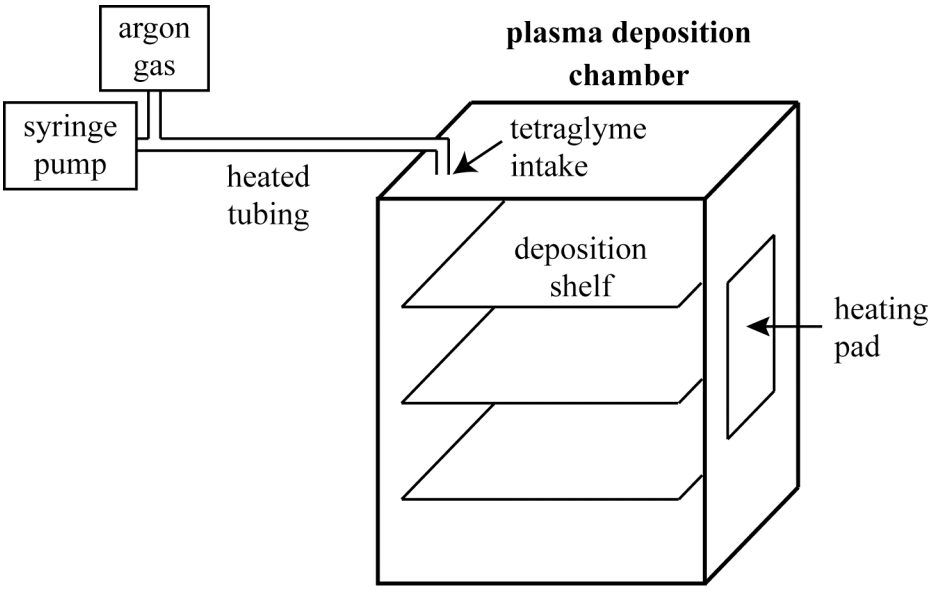

Figure 1: The configuration of the plasma deposition chamber used in this work. The syringe pump introduces tetraglyme into the heated tubing at a constant rate; the heated

tubing vaporizes the tetraglyme before it enters the plasma chamber. The external heating pads on each side of the chamber control the temperature during the deposition.

Although many types of plasmas exist and exert a variety of effects on the substrate, we will concentrate on those that are used in this work. High-power, non-reactive plasmas essentially bombard the surface of the substrate with energy. This can remove adsorbed surface contaminants [2], break chemical bonds to activate the surface [2], and etch away material [2, 3]. Low-power, reactive plasmas consist of species that can bond to each other and to reactive sites on the substrate surface, generating coatings of polymerized precursor, or monomer, molecules [4]. The plasma deposition process employed in this study, which is described more thoroughly in Chapter 3 and the appendix, utilizes both of these types of plasma (see Figure 2).

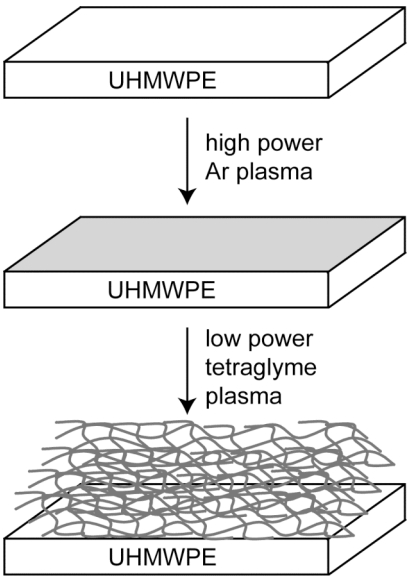

Figure 2: The sequential plasma deposition process. The sonicated UHMWPE substrate (top) is exposed to argon plasma to further clean and activate the surface (middle), enabling covalent bonding to the polymerized tetraglyme coating that is subsequently deposited (bottom).

During the first step of the process, a high-powered non-reactive argon plasma cleans the surface and breaks bonds in the UHMWPE substrate to form reactive sites. These sites are then exposed to a low-power tetraglyme plasma, which covalently bonds to the UHMWPE surface and polymerizes to produce the desired PEG-like coatings. Afterward, the chamber is flushed with argon three times to remove any remaining tetraglyme vapor. Oxygen and other undesired species are largely excluded from the process by pumping the chamber down to vacuum (30 mTorr) before the first step and between each subsequent steps.

Plasma deposition is a complex process affected by a number of different parameters. In order to produce coatings with the intended PEG-like chemistry and range of thicknesses, five variables were identified and investigated: tetraglyme flow rate, plasma power, chamber temperature, deposition time, and substrate position within the chamber. The results of these studies are presented in Chapter 3.

X-ray photoelectron spectroscopy (XPS)

X-ray photoelectron spectroscopy (XPS) is a technique employed to determine the chemical composition of the top 5-10 nm of a surface. The instrument consists of a vacuum chamber with a sample stage, an x-ray source, and an electron detector (see Figure 3). The source directs x-rays toward the surface of the sample. When the x-rays impact the sample, they dislodge core electrons from atoms on the surface (electrons from atoms deeper in the material cannot escape, which is why XPS is sensitive to only the top ~10 nm of the surface). Each electron leaves the surface with a velocity proportional to the binding energy of the atom from which it originated. The detector

measures the speed of the each ejected electron that impacts it, producing a plot of electron counts versus binding energy, which is calculated from the impact speed according to

$$E_K = h\nu - E_B - E_W \quad [1].$$

E_K is the kinetic energy of the emitted electron (determined from the impact speed on the photodetector), h is Planck's constant, ν is the frequency of the x-ray, E_B is the binding energy of the emitted electron, and E_W is the work function, which corrects for the difference between binding energies in solids and in vacuum. The value of $h\nu$ is dictated by the x-ray source (1253.6 eV for Mg Kα and 1486.6 eV for Al Kα, the source used in this work). Since the binding energy of each type of electron (1s, 2p, etc.) in each element is known and the intensity is proportional to the concentration of the element present, the binding energies act as chemical signatures, enabling quantitative determination of the elemental composition of the surface. In addition, since the chemical bonds between atoms slightly alter the binding energies of the electrons of those atoms, XPS also provides quantitative information about the types of chemical bonds present between atoms [5].

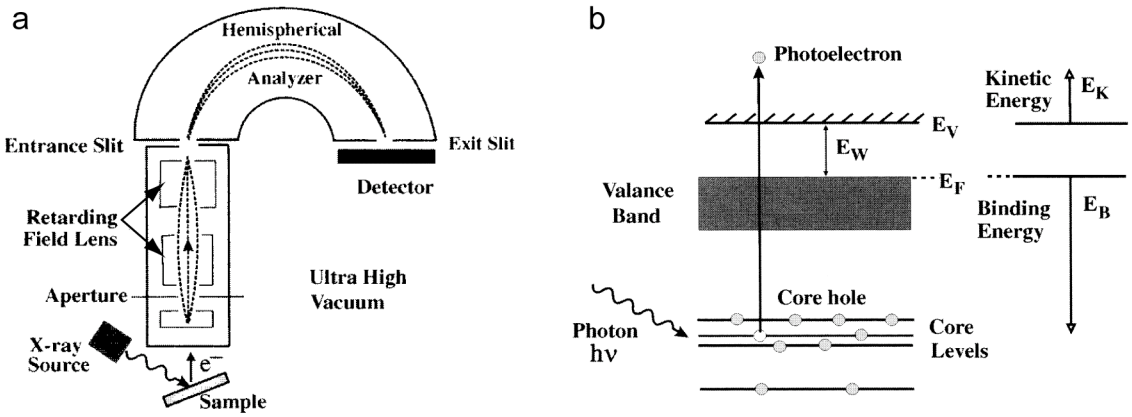

Figure 3: a) Schematic of an x-ray photoelectron spectrometer. The incoming photon and sample surface are highlighted in b), an energy diagram of the photoelectric effect. The photon imparts energy to the surface. When the photon energy hν exceeds the binding energy E_B of a core electron, the photon can eject the core electron with kinetic energy E_K. The ejected electrons pass through the hemispherical analyzer and into the detector in a), producing the XPS signal. Both figures were reproduced from [5].

The goal of the tetraglyme plasma deposition was to add a PEG-like coating to the surface of the UHMWPE substrates. Chemically, this converts surfaces that contain only carbon and hydrogen single-bonded to each other (C-H, often referred to by the more generic term hydrocarbon) to surfaces containing a combination of carbon, hydrogen, and oxygen. Plasma-polymerized tetraglyme should contain both hydrocarbon and ether (carbon single-bonded to oxygen, or C-O) bonds; these surfaces may also contain undesirable carbonyl (carbon double-bonded to oxygen, or C=O) bonds.

XPS cannot detect hydrogen, so a survey of the overall chemical composition was used to determine the amounts of carbon and oxygen on the surfaces, as well to verify that no other elements (contaminants) were present. In addition, more detailed analysis of the carbon 1s peak was performed to determine the relative quantities of hydrocarbon, ether, and carbonyl groups present. On a plot of binding energy versus number of counts (the standard XPS output) the peaks from the various species of carbon overlap and must

be fitted using analytical software. Figure 4 shows an example of an XPS survey spectrum, used to identify all of the elements present on the surface, and a fitted C1s peak, used to determine the bonding states of the carbon, as well as the binding energies of the species of interest.

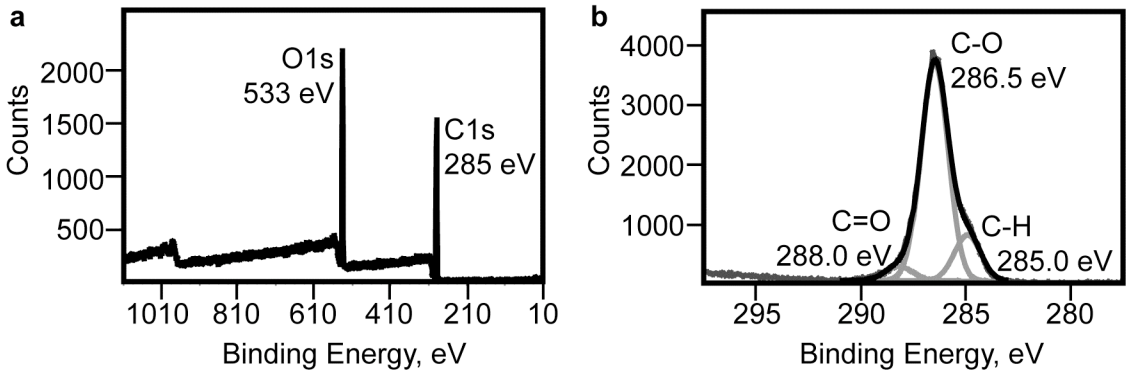

Figure 4: XPS results. a) A full survey spectrum with the O1s and C1s peaks labeled; as expected, no other XPS peaks are present. b) The high-resolution C1s peak from the same sample. The fitted hydrocarbon, ether, and carbonyl peaks are shown in light grey, the sum of the fitted peaks appears in black, and the actual spectrum is shown in dark grey.

Attenuated total reflection Fourier transform infrared spectroscopy (ATR-FTIR)

Fourier transform infrared spectroscopy (FTIR) is a common method for chemical analysis. In FTIR, a beam of infrared light passes through a sample and excites various bond motions – stretching, bending, wagging – at known frequencies specific to each type of bond and motion produced. The material absorbs the infrared energy only at the frequencies that cause vibrations, such that the resulting absorbance spectrum exhibits peaks only at those frequencies. The area under these peaks relates directly to the number of bonds present according to Beer's Law:

$$A = \varepsilon c l \qquad [2]$$

where A is the infrared light absorbance, ε is the molar absorptivity of the material, c is the concentration (number of bonds within the sampling volume), and l is the thickness of the sample, or the path length.

Attenuated total reflection Fourier transform infrared spectroscopy (ATR-FTIR) is a surface-sensitive form of infrared spectroscopy. In ATR-FTIR, instead of the infrared beam passing directly through the entire sample, the beam passes through a crystal to produce an evanescent wave at the crystal surface. The sample is pressed against the surface of the crystal such that the evanescent wave penetrates the surface of the sample to a depth d, which depends on the infrared light wavelength λ, the angle θ of the incident light, and the refractive indices of the crystal and sample (n_1 and n_2, respectively):

$$d = \frac{\lambda}{2\pi\sqrt{n_1^2 \sin^2\theta - n_2^2}} \quad [3].$$

This cutoff is not absolute (it represents the point where the intensity of the evanescent wave reaches 1/e of its maximal value), but it provides a reasonable estimate of the maximum sampling depth of the system [6].

The dependence of the penetration depth on the wavelength of the infrared light has several important consequences. First, bond motions that absorb energy at very different frequencies (for example, the C-H stretch at ~3000 cm^{-1} versus the C-O stretch at ~1100 cm^{-1}) are detected to very different maximal depths. Second, in ATR-FTIR, the penetration depth d replaces the sample thickness l in Equation 2. As a result, the absorbance also varies with the wavelength of the infrared light.

To account for the wavelength dependence of the absorbance, an advanced ATR correction is performed on the absorbance data. In the Omnic 7.3 software, the algorithm

linearly scales the absorbance intensity to remove the wavelength dependence and also corrects for several other ATR-related issues, including changes in the sample refractive index n_2 near absorption peaks and shifts in the locations of absorption peaks to lower wavenumbers [7]. However, the wavelength dependence of the sampling depth cannot be accounted for with a mathematical correction; ATR-FTIR cannot detect chemical bonds that are below than the penetration depth of the infrared beam. Consequently, for complete chemical characterization of a coating, the calculated penetration depth of the instrument used must exceed the thickness of the film.

The ATR-FTIR instrument employed in this study is a Nicolet Avatar 360 with Omni-Sampler. It has a germanium crystal with an index of refraction of 4.0 and a single-bounce wave path with an incident angle of 45°. The refractive index of the sample was assumed to be 1.5, the refractive index of both UHMWPE and PEG [8]. The penetration depths of the peaks of interest for the PEGylated UHMWPE samples were calculated using Equation 3, and the results are shown in Table 1. Since the coatings studied in these experiments rarely exceeded 200 nm in thickness (see Chapter 5), the sampling depth of this instrument was appropriate for the coatings analyzed.

Table 1: ATR-FTIR penetration depths

Chemical bond	Wavenumber, cm^{-1}	Calculated sampling depth, nm
Ether (C-O)	1115	595
Hydrocarbon (C-H)	1465	453
Carbonyl (C=O)	1730	384

Figure 5 shows a typical ATR-FTIR spectrum for the PEGylated UHMWPE samples. To determine the amounts of ether and carbonyl present, the region from 1800

or 1900 cm^{-1} to 900 cm^{-1} was peak fit using Omnic 7.3 software after performing the advanced ATR correction. For coated samples, this region usually contained ten peaks: one carbonyl (~1730 cm^{-1}); another carbonyl or water (1620-1650 cm^{-1}, always very small); one hydrocarbon doublet (modeled as a single peak at ~1465 cm^{-1}); and seven ether peaks from 940-1370 cm^{-1}. Of these, the areas under the carbonyl peak at ~1730 cm^{-1} and the most prominent ether peak at ~1115 cm^{-1} were used for quantification.

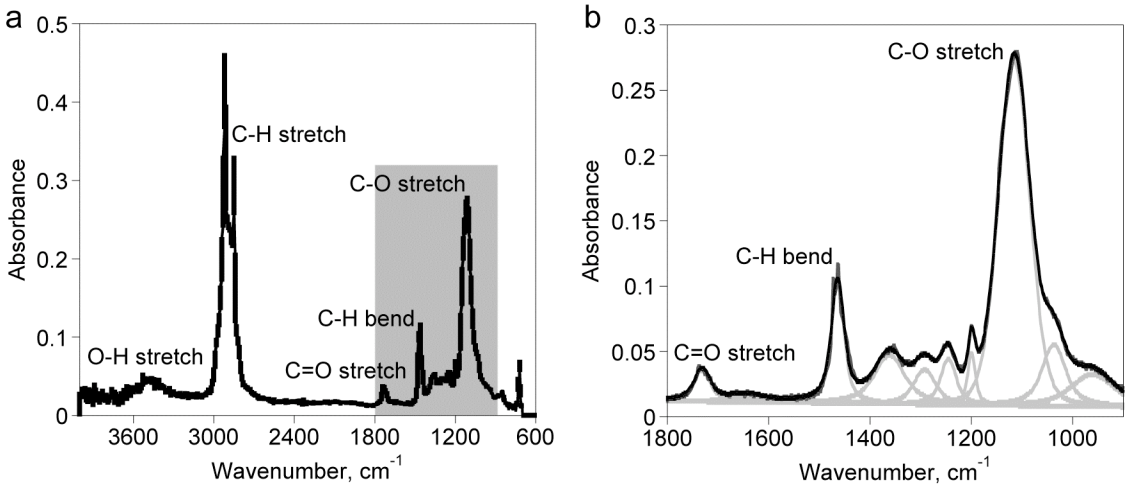

Figure 5: a) The full infrared absorbance spectrum of PEGylated UHMWPE from 4000 cm^{-1} to 600 cm^{-1}, with major peak assignments shown. The highlighted area is expanded in b) to show a ten-peak fit to the region between 1800 cm^{-1} and 900 cm^{-1}. The original data appears in dark gray, the fitted peaks in light gray, and the fitted spectrum in black. The peaks at 1115 cm^{-1} and 1730 cm^{-1} were used to quantify the ether and carbonyl content of the coatings, respectively.

However, quantification by ATR-FTIR produces different information than quantification by XPS. First, the sampling depths are quite different: about 10 nm for XPS versus a few hundred nanometers to a few microns for ATR-FTIR. Second, XPS can quantitatively determine the *absolute* elemental composition and chemical bonding of

a single surface, while ATR-FTIR can quantitatively evaluate the *relative* chemical bonding of different surfaces (or different spots on the same surface).

Like XPS, the areas under ATR-FTIR peaks are directly proportional to the concentration of the bonds from which they derive. However, unlike XPS, these areas are also affected by a number of other factors – for example, how strongly each given bond absorbs infrared energy – that cannot be readily quantified, such that comparison within a spectrum is not possible. Hence, a 1:1 ratio between the areas under the peaks from the ether stretch and the hydrocarbon bend in a single spectrum, for example, does not indicate that the surface is 50% ether and 50% hydrocarbon. Instead, a 1:1 ratio between the areas under the peaks from the ether stretches in two different spectra indicates that those two samples have the same amount of ether bonding – but the amount relative to the hydrocarbon content remains unknown.

One important caveat is that this analysis assumes an identical sampling volume between the surfaces being quantitatively compared. In ATR-FTIR, the sampling volume V depends on the penetration depth d from Equation 3, as well as area of the surface A_c in contact with the ATR crystal:

$$V = dA_c \qquad [4].$$

Path length appears in Equation 2 instead of sampling volume because Equation 2 assumes a constant cross-sectional area, which is appropriate in transmission-mode FTIR because the area depends only on the diameter of the infrared beam, but inappropriate in ATR because the ATR crystal spreads the beam across its entire surface. In ATR-FTIR, therefore, the absorbance depends directly on both the penetration depth and the area in contact with the crystal. As long as the two samples have the same refractive index and

the same pressure is applied to both, the sampling depth is constant between them; however, the area in contact with the ATR crystal can depend on the geometry of the sample [6]. For the work presented here, the 250 μm thick UHMWPE substrates used were compliant enough that they only made contact with the crystal directly below the tip of the ATR-FTIR sample holder, and it was verified that the pressure from the sample holder remained constant from sample to sample. Therefore, the quantitative comparisons presented in Chapters 3-5 should be valid.

ATR-FTIR mapping

Standard ATR-FTIR spectroscopy sends an infrared beam across the entire surface of the ATR crystal and measures the signal from the entire region of the sample that is in contact with the crystal, producing a single spectrum as the output. In contrast, ATR-FTIR mapping employs a focused infrared beam with a small spot size (here, 25 μm). The beam is rastered across a specific region of the sample at designated intervals (here, 37.5 μm), collecting a full spectrum at every spot. Maps of the surface are then constructed from the data in the individual spectra to provide information about a particular chemical bond. Due to the curvature of the ATR crystal, the maximal intensity of the FTIR signal varies across the mapped region. To compensate for this, all ATR maps used in this work were constructed by taking the ratio of the area under the peak of interest – usually the main ether peak at 1115 cm^{-1} – to the area under a reference peak from a chemical bond that is present in constant quantity across the entire surface. The reference peak used here was the hydrocarbon doublet at 1472 and 1465 cm^{-1}.

Contact angle goniometry

Contact angle goniometry measures the relative hydrophilicity or hydrophobicity of a surface. In its simplest form, the sessile drop method, a drop of water is placed onto the surface of a sample, and the angle between the sample surface and the tangent to the drop (through the liquid) is measured (see Figure 6). The more hydrophilic the surface is, the more the drop spreads, and the lower the contact angle is. Variants on this approach include the use of alternative liquids, such as diiodomethane or glycerol, as well as submerging the sample into liquid and measuring the angle between an introduced air bubble and the submerged sample surface [9].

The system shown in Figure 6 takes an image of the drop and calculates the contact angle θ using the Tangent Chord Theorem,

$$\theta = 2\tan^{-1}\left(\frac{2h}{l}\right) \qquad [5],$$

where h is the height of the drop at its highest point and l is the diameter of the base of the drop (see Figure 6b). This calculation assumes that the drop is spherical, which was confirmed by fitting the profile of the drop to a circle.

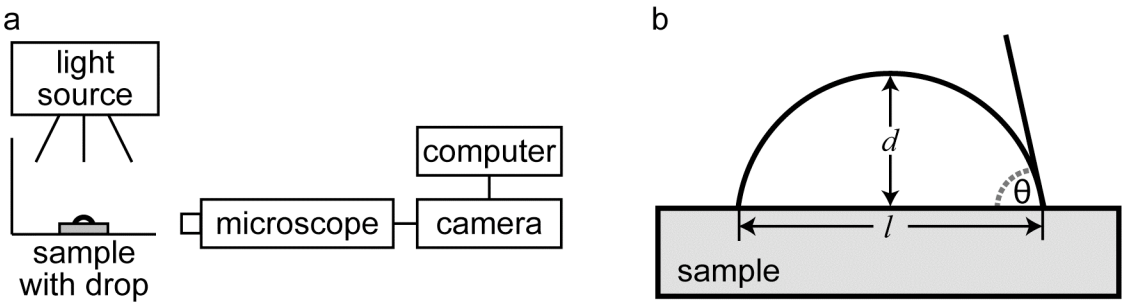

Figure 6: a) Schematic of the contact angle goniometer. b) A close-up view of the sample and drop. The angle θ is always measured through the drop.

The main reason for PEGylating the UHMWPE surface is to increase the hydrophilicity of the surface to improve retention of synovial fluid, and therefore lubrication, at the articulating surface. Contact angle measurements were performed to verify that the PEG-like coatings were in fact more hydrophilic than untreated UHMWPE.

Protein deposition/fluorescence microscopy

Directly detecting small amounts of protein on a surface can be challenging. Many methods, such as optical waveguide lightmode spectroscopy (OWLS) and quartz crystal microbalance (QCM) require the use of special substrates – for example, materials coated with an optical waveguide for OWLS, or quartz crystal disks for QCM. In contrast, fluorescence microscopy relies on modification of the protein, rather than the substrate, by covalently conjugating fluorophores to the proteins. While this restricts the choice of protein (it is impossible, for example, to measure the nonspecific binding of all proteins from serum on a surface), it allows for analysis of a wide range of substrates, including PEGylated UHMWPE. In addition, fluorescence microscopy takes images of the adsorbed proteins, which has the potential to show defects in the coatings.

The process of fluorescence is shown in Figure 7. Incident light ($h\nu_{EX}$) hits the fluorophore and excites an electron, raising it from the ground state (S_0) of energy to an excited state (S_1'; step 1 in the diagram). The excited electron then loses some energy to its surroundings (step 2), bringing it down to the relaxed excited state S_1. Finally, the electron emits a photon of light ($h\nu_{EM}$, step 3) and returns to the ground state. Since the electron loses energy as it shifts from the excited state to the relaxed excited state, the

light emitted from the relaxed excited state light is always lower-energy (higher wavelength) than the initial excitation light.

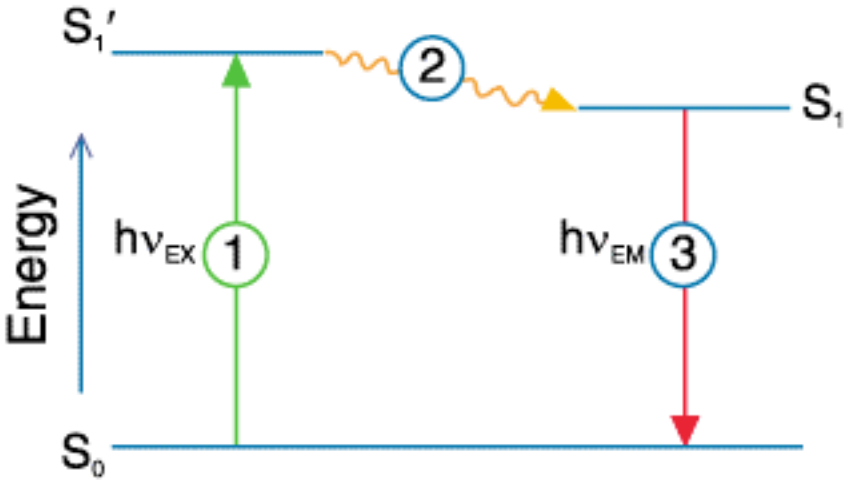

Figure 7: An energy diagram of the fluorescence process, reproduced from [11].

Well-characterized fluorophores are conjugated to proteins to render them fluorescent. The fluorophores can be chosen so that they fluoresce at a different wavelength from the background fluorescence from the sample. During a protein deposition experiment, samples are soaked in a solution of fluorescently-tagged protein, washed to remove protein that is not tightly bound, and then imaged in a fluorescence microscope. The samples are excited at the excitation wavelength of the chosen fluorophore and imaged at its emission wavelength. Band-pass filters reduce the signal from non-specific fluorescence, such as the background fluorescence of the sample.

The protein used in this experiment was bovine serum albumin (BSA) conjugated to AlexaFluor 488. BSA was chosen because albumin is the most abundant protein in

synovial fluid [10]; AlexaFluor 488 was chosen because its emission wavelength, 520 nm, is well-separated from the background fluorescence of UHMWPE.

Statistical analysis

Much of the focus of this work involves comparisons between groups: the chemistry and performance of untreated UHMWPE versus a variety of coatings produced with different plasma processing parameters. For XPS and contact angle goniometry, statistical analysis was used to determine the effect of two processing parameters, plasma deposition time and temperature, on the chemistry and hydrophilicity of the resulting coatings. Since the analysis focuses on differentiating between groups, the analysis of variance (ANOVA) method was chosen. This approach compares the variance (difference between measurements) of measurements taken between different groups to that of measurements taken within groups – for example, the variance of all contact angle measurements on samples produced at 50°C versus the variance of measurements within substrates from a single 50°C plasma batch.

ANOVA involves two main tools: the F test, which determines whether at least one of the groups is different from the rest of the population, and the *t* test, which identifies the pairs of individual groups that are distinguishable [12]. Both the F test and the *t* test are parametric (they assume that the data are normally distributed) and hypothesis-driven. The assumption of normal distribution means that these tests work best on groups with at least 30 samples, which is not true for this study; however, these tests are still used on data sets with smaller sample sizes. In all cases, the default, or null, hypothesis states that all groups under consideration are part of the same population; the

alternative hypothesis states that at least one group is different. The methods were used to evaluate the results of two sets of data: the ether content of the surfaces as measured by XPS and the relative hydrophilicity of the surfaces as measured by contact angle goniometry. In both cases, the statistical analysis focused on two questions: the effect, if any, of plasma deposition *time* on coating chemistry/hydrophilicity, and the effect, if any, of plasma deposition *temperature* on coating chemistry/hydrophilicity. Combined, the null hypotheses therefore state that

i. plasma deposition time does not affect the ether content or hydrophilicity of the surfaces; and
ii. plasma deposition temperature does not affect the ether content or hydrophilicity of the surfaces.

All analyses include comparisons to untreated UHMWPE, thereby also testing the null hypothesis that plasma deposition of tetraglyme under each combination of conditions did not change the chemistry or performance of the UHMWPE surface.

Since the analyses involve a large number of groups – untreated UHMWPE, as well as coatings produced at both 40°C and 50°C at a range of deposition times – the first step in each statistical analysis would typically be to perform an F test on the entire data set. However, the data for the surface are nested. Non-nested data consist of single measurements taken for single samples, such that there is no reason to believe that any individual data points are related to each other. In this case, all data are independent. Nesting occurs when multiple measurements are taken on the same sample, such that multiple data points might be related. For example, if XPS were performed at two different spots on each of five substrates, ten measurements would be reported. If these

measurements were truly independent, they would exhibit a normal distribution. However, if the variation in chemistry within a single substrate is lower than the variation between substrates (which might be expected if the plasma deposition process were highly spatially dependent), the data might look more like five pairs of results. In this case, the data would violate the assumption of a normal distribution, and the statistical analysis might not be valid.

The goal of both assays was to determine a single metric for an entire plasma deposition batch. To maximize the accuracy of the measurements, two substrates from each batch were tested, as were two spots on each substrate, for a total of four results per batch. The issue of nesting was addressed by assuming that all measurements were independent. Effectively, this treats all data as though they were taken separately, rather than as replicates of the same spot or substrate. This assumption is only valid if the variation within related measurements (such as two spots on a single substrate) approximately equals the variation between unrelated measurements (the data for two different substrates). However, the limited sample size of the data (two spots on two substrates) precludes a meaningful comparison of the within- and between-group variations.

After assuming independence, sequential F tests were performed to evaluate the two hypotheses (regarding the effects of plasma deposition time and temperature) separately. First the effect of deposition time was analyzed within groups produced at the same temperature. If the F test indicated that, within a given temperature, at least one group was different, Holm *t* tests were performed on every possible pair of groups to identify the ones with significant differences (indicative of time dependence). If a single

plasma deposition batch was consistently different from all others, it was removed from the overall group. To determine the effect of temperature, a second F test was then performed on the three overall groups – uncoated UHMWPE, coatings produced at 40°C, and coatings produced at 50°C - and, if the F test indicated a difference, followed by Holm *t* tests of all possible pairs.

It is important to note that the standard *t* test may only be used to compare two sets of samples. Performing multiple comparisons leads to an overestimate of the actual confidence of the comparison that is approximately proportional to the number of comparisons *c* that are made:

$$P_{true} \approx cP_{assumed} \quad [6].$$

P is related to the degree of confidence DC by

$$DC = 100 * (1 - P) \quad [7],$$

such that an increase in the true P value leads to a decrease in the true degree of confidence of the test. For example, by making three comparisons instead of one, an assumed level of confidence of 95% (P = 0.05) becomes an actual level of 85% (P ~ 0.15) [12].

From Equation 7, it follows intuitively that one can avoid overestimating the confidence of the test as a whole by dividing the desired degree of confidence by the number of comparisons to yield a new, lower P value for each individual *t* test. However, this approach, known as the Bonferroni *t* test, is quite conservative, and may therefore fail to detect a significant difference when one actually exists. The Holm *t* test is based on the Bonferroni test, but the *t* tests are performed sequentially, starting with the pair

most likely to exhibit significant difference, and each individual pairwise test is compared to a different critical value that accounts for tests already performed.

For example, to evaluate the effect of temperature, three overall groups must be compared pairwise: uncoated vs. 40°C, uncoated vs. 50°C, and 40°C vs. 50°C. To achieve an overall confidence P, the individual pairwise tests are ranked 1-3 in order of decreasing absolute *t* metric. The individual criteria α_i for each *t* test are then calculated as:

$$\alpha_i = \frac{P}{k-(i-1)} \qquad [8]$$

where *i* is the rank of the test being performed and *k* is the total number of pairwise comparisons being performed (here, 3). This means that the most different pair is held to the least stringent criterion for determining a difference, while the least different pair is held to the strictest criterion, the same value that would have been used for all pairwise comparisons according to the Bonferroni method.

Atomic force microscopy (AFM)

The atomic force microscope (AFM) is a very versatile tool. As shown in Figure 8, it consists of a cantilever with an attached tip that interacts with the sample surface. A laser beam reflects off of the back of the cantilever and into a photodetector. As the tip interacts with the sample surface, the cantilever bends and the reflected light moves on the photodetector; this data is used both as output and for feedback control of the system. The sample, which rests on a stage with x and y motion controllers, rasters underneath the tip to produce a topographical map of the surface ranging from tens of nanometers to tens of microns on a side. Experiments can be performed in air or liquid.

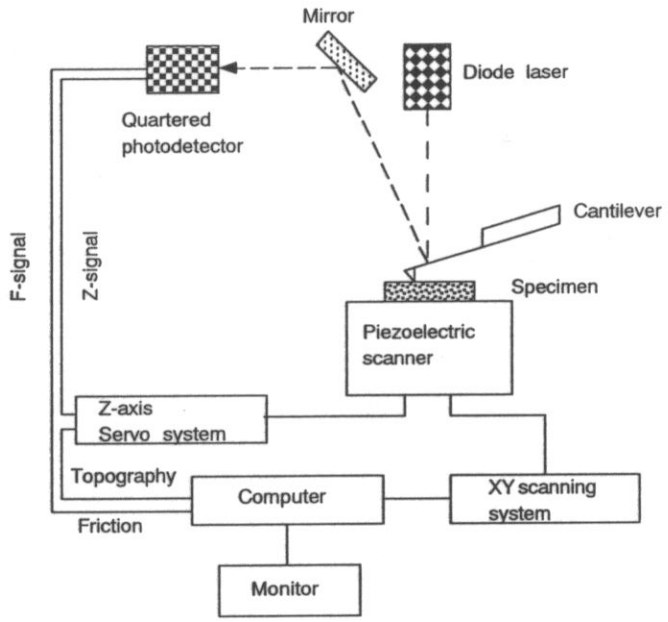

Figure 8: Diagram of an atomic force microscope, reproduced from [13].

Interactions between the tip and the surface are controlled by applying voltage to a piezoelectric crystal. The tip can interact with the surface in several modes, most commonly contact and tapping. In contact mode, the tip presses against the surface at a fixed force (from nanonewtons to micronewtons), which is maintained by feedback control of the voltage passed through the piezo. Since the tip drags across the sample surface during imaging, the process can damage the surface, particularly if the tip is sharp and the sample is soft [14]. This can be advantageous: in the thickness measurements described in Chapter 5 and the nanotribotesting presented in Chapter 6, contact mode AFM was used to wear away the coatings with a normal force of 1.0-2.5 μN.

Tapping mode AFM is more commonly used for imaging, and was employed to image the damage to the coating caused by the contact mode scratching. In tapping mode, the tip vibrates at a fixed amplitude, such that it remains a fixed distance above the surface. Interactions with the surface alter the amplitude of the vibration, changing the

amount of energy required to maintain the intended amplitude/distance. Since the tip taps against the surface intermittently rather than dragging across it, tapping mode AFM can non-destructively image soft surfaces, such as the PEG-like coating on the UHMWPE substrate. In this study, the resulting topography images were used to determine the thickness of the PEG-like coatings, as well as the RMS roughness of both untreated UHMWPE and PEGylated surfaces. Tapping mode images of a PEGylated sample before and after contact-mode wear appear in Figure 9.

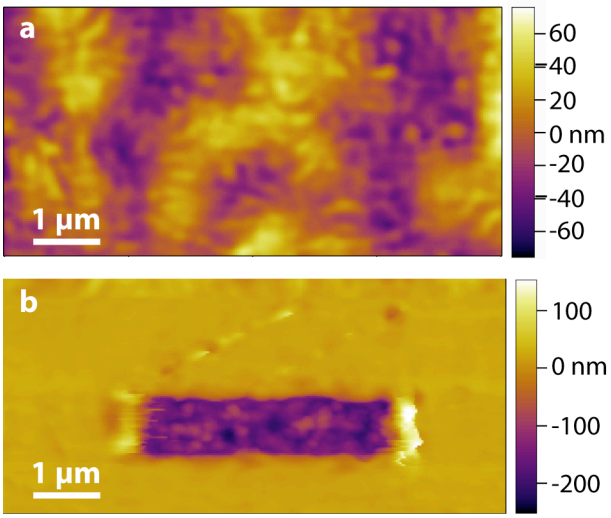

Figure 9: a) A topographical image of a PEGylated UHMWPE surface with RMS roughness of 20.9 nm. b) The same surface after the middle section was worn away by the AFM tip in contact mode. The unworn region appears smooth because the image of the undamaged surface in part a) was subtracted from the worn image to highlight the effects of the scratching by minimizing the appearance of the surface roughness. This method is discussed in greater detail in Chapter 5.

Pin-on-disk wear testing

Pin-on-disk tribotesting is a common technique used to evaluate the wear and friction behavior of articulating surfaces in a lubricant of choice. It has been employed

extensively to test materials and lubricants associated with total joint replacements [10, 15, 16]. The setup, shown in Figure 10, is analogous to a record player: a pin is attached to an arm and placed in contact with a rotating flat disk in a fluid bath. In the system used here, a cobalt-chrome (CoCr) disk rotates at a fixed speed, wearing against the UHMWPE pin for a finite distance in diluted bovine serum. Weights placed on the arm directly above the pin apply the normal force necessary to generate the desired contact pressure.

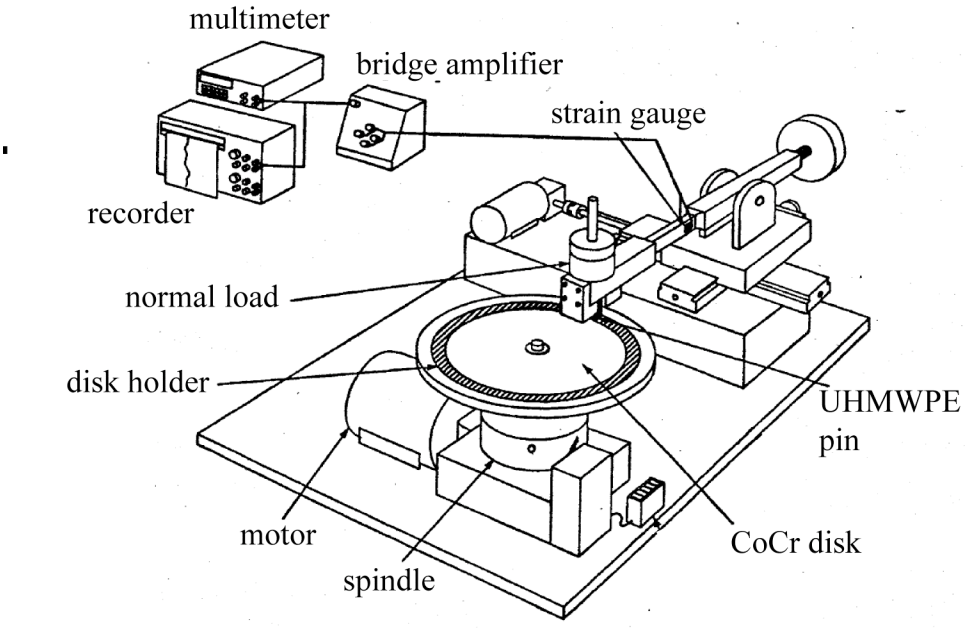

Figure 10: Diagram of the pin-on-disk wear tester, modified from [15].

Pin-on-disk experiments usually explore basic wear mechanisms or compare the tribological behavior of different combinations of materials and/or lubricants. These tests can provide valuable insight into material behavior and can evaluate the effect of changes to lubricants or materials. For example, Gispert et al used pin-on-disk testing to compare

the coefficient of friction of stainless steel, CoCr, and alumina pins articulating against UHMWPE disks lubricated with various combinations of Hank's balanced salt solution, hyaluronic acid, and bovine serum albumin [17]. In this vein, pin-on-disk testing was chosen to analyze the effect of PEGylation of the UHMWPE surface on the wear behavior of the material. However, pin-on-disk experiments have distinct limitations. While pin-on-disk testing provides valuable preliminary information about macroscopic material behavior, it cannot replicate the complex geometries and motions of total joint replacements in the body. A joint simulator would be necessary to evaluate the wear behavior of the entire system under more clinically-relevant conditions.

Thus, pin-on-disk testing evaluate tribological behavior at an intermediate level: smaller than a join simulator, which evaluates the behavior of parts that are tens or hundreds of square centimeters in area, but much larger than AFM scratch testing. In the experiments presented in Chapter 6, the PEGylated UHMWPE pin terminates in a flat surface 2 mm in diameter. The applied contact pressure was either 3 MPa, to simulate conditions in a total hip replacement, or 21 MPa, to simulate conditions in a knee replacement.

In contrast, the AFM scratch tests experiments employed a tip roughly 20 nm in diameter to scratch a region 4 μm^2 in area. Consequently, while both experiments involved unidirectional wear of the UHMWPE substrate, pin-on-disk testing is more indicative of how a larger, multi-asperity surface behaves, whereas AFM models the wear behavior of a single asperity on a surface. The normal forces in the AFM nanoscratching experiments ranged from 1.0-2.5 μN, resulting in contact forces on the order of 1 GPa. While this is 2-3 orders of magnitude greater than the contact pressure applied to the pin

in pin-on-disk testing, it is probably a reasonable approximation of the loading conditions of asperities on the pin. The contact pressure calculated for the pin assumes that the entire microtomed surface is in contact with the disk, but in reality only the asperities on the pin surface are in contact. The real area of contact could easily be orders of magnitude lower than the nominal contact area, raising the asperity contact pressure into the gigapascal range.

References

1. Rossnagel, S.M., J.J. Cuomo, and W.D. Westwood, eds. *Handbook of Plasma Processing Technology*. 1990, Noyes Publications: Park Ridge, NJ.
2. Bunshah, R.F., ed. *Handbook of Deposition Technologies for Films and Coatings*. 2nd ed. 1994, Noyes Publications: Park Ridge, NJ.
3. Wang, A., et al., *Orientation softening in the deformation and wear of ultra-high molecular weight polyethylene.* Wear, 1997. **203**: p. 230-241.
4. Forch, R., et al., *Recent and expected roles of plasma-polymerized films for biomedical applications.* Chemical Vapor Deposition, 2007. **13**(6-7): p. 280-294.
5. Verma, H.R., *Atomic and Nuclear Analytical Methods*. 2007, New York: Springer.
6. Smith, B.C., *Fundamentals of Fourier Transform Infrared Spectroscopy*. 1996, New York: CRC Press.
7. Nunn, S. and K. Nishikida, *Advanced ATR Correction Algorithm (Application Note 01153)*. 2003, Thermo Electron Corporation: Madison, WI.

8. Brandrup, J., et al., eds. *Polymer Handbook*. 4th ed. 1999, John Wiley & Sons, Inc.: New York.

9. Holmberg, K., ed. *Handbook of Applied Surface and Colloid Chemistry*. Vol. 1-2. 2002, John Wiley & Sons: Chichester, England.

10. Heuberger, M.P., et al., *Protein-mediated boundary lubrication in arthroplasty.* Biomaterials, 2005. **26**(10): p. 1165-1173.

11. Invitrogen, *http://probes.invitrogen.com/handbook/figures/0664.html*. Viewed 20 April, 2008.

12. Glantz, S.A., *Primer of Biostatistics*. 6th ed. 2005, San Francisco: McGraw-Hill.

13. USByte, *http://www.usbyte.com/images/AFM%20schematics.JPG*. Viewed 22 Jan, 2008.

14. Kaupp, G., *Atomic Force Microscopy, Scanning Nearfield Optical Microscopy and Nanoscratching*. NanoScience and Technology, ed. P. Avouris, et al. 2006, New York: Springer.

15. Klapperich, C., K. Komvopoulos, and L. Pruitt, *Tribological properties and microstructure evolution of ultra-high molecular weight polyethylene.* Journal of Tribology-Transactions of the ASME, 1999. **121**(2): p. 394-402.

16. Shi, W., H. Dong, and T. Bell, *Tribological behaviour and microscopic wear mechanisms of UHMWPE sliding against thermal oxidation-treated Ti6Al4V*. Materials Science and Engineering a-Structural Materials Properties Microstructure and Processing, 2000. **291**(1-2): p. 27-36.

17. Gispert, M.P., et al., *Friction and wear mechanisms in hip prosthesis: Comparison of joint materials behaviour in several lubricants.* Wear, 2006. **260**(1-2): p. 149-158.

Chapter 3

The Plasma Deposition Process

Introduction

Plasma deposition is a common technique for surface modification. It works on a wide range of substrate materials and sizes, and it can produce a wide range of surface chemistries, including coatings that are covalently bonded to the substrate. It is particularly attractive for unreactive substrates, such as polyethylene, which lack the side chain functionality required to graft other molecules onto the surface [1, 2]. In addition, plasma deposition can produce sterile surfaces, a significant benefit for medical applications [3].

Ratner et al have utilized plasma deposition to generate coatings from a number of different monomers, including various oligoglymes (mono-, di-, tri-, and tetra-), crown ethers (12-crown-4, 15-crown-5), and dioxane [4-6]. The goal of these studies was to produce surfaces that mimic the chemical structure of polyethylene glycol (PEG), a biocompatible hydrophilic polymer whose resistance to protein and cell deposition has been investigated extensively [7-9]. Resistance to protein deposition is expected to

reduce opsonization, an immunological response whereby immunoglobulins and other proteins coat the surface of foreign materials to make the particles easier to phagocytose.

Such treatments could be beneficial in the prevention or minimization of osteolysis associated with ultra high molecular weight polyethylene (UHMWPE) wear debris generated in articulation of total joint replacements (discussed in more detail in Chapter 1). Since phagocytosis of wear particles initiates the immune response that culminates in wear-mediated osteolysis, decreasing the phagocytosability of the wear particles by rendering them protein-resistant could lead to a decreased immune response and consequently decreased osteolysis. This effect was in fact observed in a study of bone resorption in response to injection of polystyrene particles, either uncoated or coated with protein-resistant 2-methacryloyloxyethyl phosphorylcholine, adjacent to mouse calvariae: the coated particles caused substantially less bone loss than the untreated polystyrene controls [10].

From all of the glymes and crown ethers they evaluated, Johnston et al [6] found that tetraglyme produced the most protein-resistant, hydrophilic, PEG-like coatings. Therefore tetraglyme was chosen for this study as well. Although Lopez et al [4, 5] and Johnston et al [6] determined effective plasma processing parameters such as plasma power and flow rate for their equipment, it is well known that plasma conditions vary from instrument to instrument [1, 2], and it was therefore necessary to reevaluate the parameters for the system employed in this study.

The goal of this work was to identify plasma processing conditions that generate variable-thickness coatings with a consistent, homogeneous chemical structure similar to PEG (unlike PEG, the plasma-deposited coatings are crosslinked). Although the

experiments were designed to elucidate the effects of various plasma processing parameters on the resulting coating chemistry, the study was not intended to be a true optimization of the process.

The chemical structure and relative thickness of every batch of coatings were evaluated using ATR-FTIR; XPS was also performed on selected samples to confirm the near-surface chemical structure of the coatings. As discussed in Chapter 2, the ATR-FTIR spectra of the coatings exhibit three peaks from three bonds of interest: hydrocarbon (C-H), ether (C-O), and carbonyl (C=O). UHMWPE consists solely of hydrocarbon bonds; however, tetraglyme also contains hydrocarbon groups, so changes in these peaks provide only limited information regarding the plasma deposition process. Ether bonds are unique to tetraglyme and provide information about both coating chemistry and relative thickness, which is explored in more detail in Chapter 5. Carbonyl bonds are not present in either UHMWPE or pure tetraglyme. Consequently, their presence in the plasma-deposited coatings indicates that some tetraglyme molecules fragment and recombine in undesirable ways during the deposition process. Since this produces less PEG-like surfaces, plasma processing parameters were chosen to minimize carbonyl content whenever possible.

Materials and Methods

A 250 μm thick sheet of UHMWPE (McMaster-Carr) was cut into 5 mm x 20 mm substrates, which were cleaned according to the protocol in the Appendix. The substrates were then coated with plasma-polymerized tetraglyme (Sigma-Aldrich), which was periodically tested by ATR-FTIR (Nicolet Avatar 360 with Omni-Sampler) to ensure

purity; no chemical changes or carbonyl species were ever detected. For the tetraglyme deposition, the substrates were placed on a wire mesh tray on the top shelf of the plasma chamber, a Plasma Science PS0500 with a 13.56 MHz, 550 W generator. During the tetraglyme deposition process, liquid tetraglyme was pumped into 130°C heated tubing outside of the deposition chamber using a syringe pump (Cole Parmer) at a controlled rate to vaporize the tetraglyme before it entered the chamber; simultaneously, a very low flow of argon was used to flush the vapor through the tubing and into the chamber. 30 sccm of argon gas was also flowed directly into the chamber in order to stabilize the plasma during deposition. For some depositions, the chamber temperature was controlled with external, feedback-controlled heating pads attached to two sides of the chamber. All deposition processes involved three steps:

1. high temperature argon plasma treatment to clean and activate the UHMWPE surfaces (250 sccm argon, 400 W, 3 min; chamber pressure ~200 mTorr), enabling covalent bonding of the tetraglyme coating
2. tetraglyme deposition (30 sccm argon, other parameters varied; chamber pressure ~55 mTorr for 50 W processes)
3. chamber flushing with argon to remove remaining tetraglyme vapor (250 sccm argon, 0 W, 1 min, repeated 3 times).

Before each step, the chamber was pumped down to a base pressure of 30 mTorr. A diagram of the instrument configuration, the details of the instrument setup, and all settings for each step can be found in the appendix.

After deposition, ATR-FTIR spectra of the coated samples were taken using a Nicolet Avatar 360 with an Omni-Sampler ATR accessory (Ge crystal, single-bounce

beam path, 45° incident angle, 32 scans). An advanced ATR correction was applied to all spectra and the region containing the ether, hydrocarbon bending, and carbonyl peaks was peak fit using Omnic 7.3 software. For most plasma deposition batches, spectra were collected on three samples at two spots, and the results of the six spectra were averaged to determine metrics for the batch as a whole. For depositions involving the wear pins used in Chapter 6, the chemistry of the coating on the pins was estimated by performing ATR-FTIR on two 250 μm thick UHMWPE strips near the pins: one in front of the leftmost of three adjacent pins, and the other behind the rightmost pin.

All variables investigated in this study pertained to the second step of the plasma process, the tetraglyme deposition. For this step, the variables of interest included the tetraglyme flow rate, plasma power, chamber temperature, sample position within the chamber, and deposition time. Results will be presented in this order.

Results and Discussion

Tetraglyme flow rate

Because tetraglyme is a large molecule (molecular weight 222.3 g/mol) with a high boiling point (276°C at atmospheric pressure), some care must be taken to ensure that it enters the plasma deposition chamber with a steady flow rate in gaseous form. Preliminary investigations found that these requirements were best met by flowing liquid tetraglyme through tubing pumped down to 30 mTorr and heated to 130°C to evaporate the tetraglyme before it entered the plasma chamber. A syringe pump maintained the flow of the liquid tetraglyme into the tubing tetraglyme, and low-pressure argon gas

flowed into the tubing to push the tetraglyme vapor into the deposition chamber. A diagram of the final setup is shown in Figure 1.

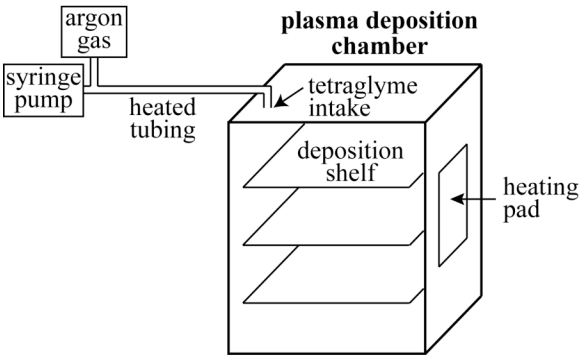

Figure 1: The plasma deposition system. A second heating pad, not visible in this diagram, is located on the outside of the left side of the chamber.

Several different tetraglyme flow rates (from the syringe pump into the heated tubing) were investigated, and the results are shown in Figure 2. As the plots indicate, the flow rate has a more significant effect on the ether content of the coatings than on the carbonyl content. Both 3 and 9 ml/hr produced coatings with widely varying ether content. At 3 ml/hr, the tetraglyme may have been entering the chamber in boluses, rather than as a steady stream. At 9 ml/hr, excess tetraglyme pooled in the bottom of the chamber and remained present after the deposition ended, likely leading to inconsistent tetraglyme vapor concentrations during the depositions. The ether content of the films was most reproducible at 6 ml/hr, so this flow rate was used for all subsequent depositions.

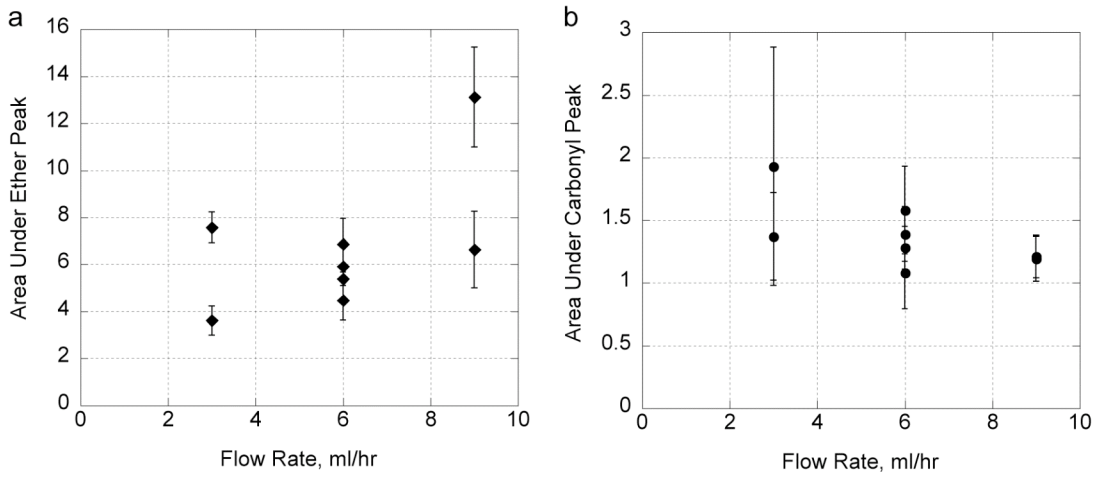

Figure 2: The effect of tetraglyme flow rate on the area under the a) ether and b) carbonyl peak. All depositions were performed for 10 minutes at 50 W in an unheated chamber.

Plasma power

Plasma power is known to affect the degree of fragmentation of precursor molecules during deposition. Higher power adds more energy to the system, which can increase fragmentation and decrease retention of the chemical structure of the precursor. Lopez et al found this to be true for glyme-based coatings: for a series of oligoglyme precursors, lower plasma power (40 W) produced coating chemistries more similar to the precursors – and therefore to PEG – than higher plasma power (80 W) [5]. In addition, Johnston et al found minimal differences in coating chemistries produced from tetraglyme at 5 W versus 20 W, but the surfaces generated at 5 W adsorbed and retained less fibrinogen than the surfaces generated at 20 W, suggesting that the 5 W surfaces better resist protein deposition [6].

Preliminary experiments with the deposition system used in this work indicated that high powers (200-400 W) produced surfaces with more hydrocarbon and carbonyl,

and less ether, than a true PEG-like surface should exhibit. As expected, lower powers (50-100 W) produced more PEG-like surfaces, and these powers were consequently investigated in more detail, with a focus on increasing ether content while decreasing carbonyl presence. Figure 3 shows the area under the ether and carbonyl peaks for surfaces deposited at two different powers and two different deposition times. Both deposition times show an undesirable increase in carbonyl content with increasing power. In addition, the ten-minute deposition produced surfaces with more ether at 50 W than at 100 W. Together, these results indicate that, as expected, that the lower power generated more PEG-like surfaces than the higher power. Consequently, 50 W was used as the power for most subsequent depositions.

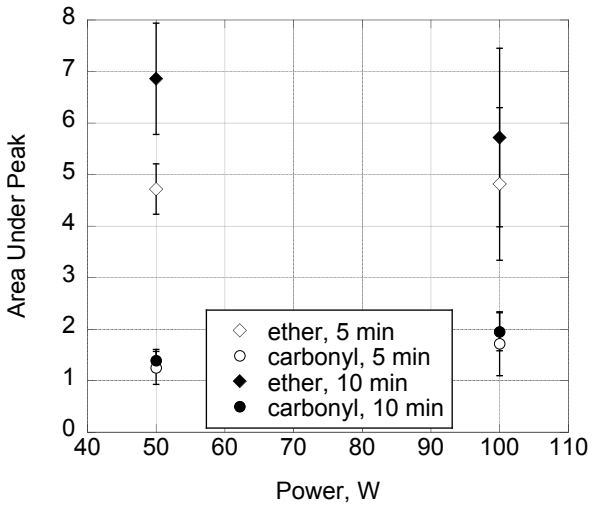

Figure 3: The effect of plasma power on coating chemistry in an unheated chamber. Depositions were performed in an unheated chamber at 50 W with 6 ml/hr tetraglyme flow for 5 minutes (open symbols) and 10 minutes (closed symbols). All data represent the areas under the ether or carbonyl peaks of the ATR-FTIR spectra of the coatings.

A second study, limited to ten-minute depositions, was performed at 30-70 W with the walls of the plasma chamber heated to 50°C (the chamber was unheated in the

first experiment). These results, shown in Figure 4, indicate that when the chamber is warmer, the ether content of the deposited surfaces rises steadily with increasing plasma power up to 70 W, while the carbonyl content does not change substantially.

Coupled with the data in Figure 3, this suggests two possibilities: either the ether content of the surface reaches a maximum for depositions performed between 70 and 100 W, or the temperature of the chamber affects the optimal plasma power. The latter could occur if the tetraglyme precursor condensed on the unheated chamber walls, decreasing the amount of tetraglyme vapor available to absorb the plasma energy and increasing fragmentation of the remaining vaporized molecules. In addition, the temperature of the system affects the diffusion of molecules on the substrate surface. Further experiments were conducted to elucidate the effects of temperature on the deposition process.

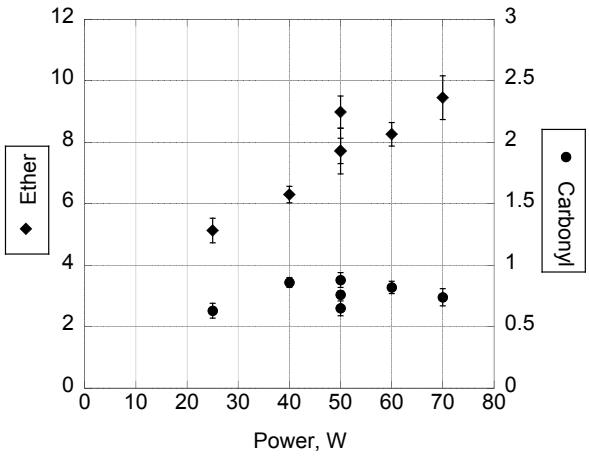

Figure 4: The effect of plasma power in a plasma chamber heated to 50°C. Depositions were performed at 50 W with 6 ml/hr tetraglyme flow for 10 minutes.

Chamber temperature

The temperature of the plasma chamber can affect several aspects of the deposition process. At lower temperatures, the monomer vapor can condense on the chamber walls, thereby decreasing the vapor concentration of the precursor. In addition, the temperature of the chamber can affect what types of chemical reactions – molecular fragmentation, recombination, polymerization, crosslinking – occur during the process, as well as their rates. Consequently, if the temperature varies from batch to batch, the vapor concentration of the precursor and the rate of each possible reaction can vary as well, and the resulting coatings may have different thicknesses and/or chemical structures.

The plasma deposition chamber used in these experiments was not insulated, and the ambient temperature varied by more than 10°C over the course of the study. During the initial experiments, two important observations emerged. First, tetraglyme sometimes condensed visibly on the top or bottom of the chamber. Second, the deposition results were often consistent over the course of a single day, but inconsistent from day to day, particularly when the ambient temperature outside the chamber varied widely. The first observation suggested that the vapor concentration of tetraglyme within the chamber depended on the chamber temperature, and the second indicated that it was significantly affecting the resulting coatings. To remove the effects of ambient conditions from the deposition process, and to ensure that the tetraglyme present in the chamber remained gaseous during the deposition, the chamber was heated with external, feedback-controlled heating pads located on two sides (see Figure 1).

The effect of the heating pad temperature was evaluated in the range of 35°C (slightly higher than the maximal ambient temperature observed) to 55°C. The internal temperature of the chamber was also monitored, and the results are shown in Figure 5.

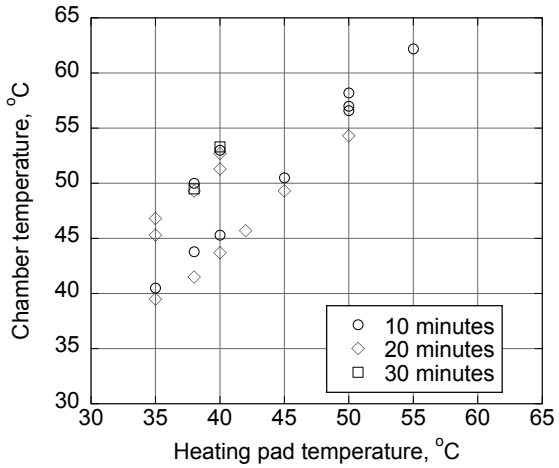

Figure 5: Actual plasma chamber temperature versus heating pad temperature for three different deposition times.

All deposition times exhibit higher chamber temperatures than heating pad temperatures. This increase stems largely from the heat imparted to the chamber during the first step of the plasma process, the high-power (400 W) argon cleaning step. However, some of the lower-temperature depositions (35-40°C heating pads) have chamber temperatures 5-7°C higher than others. This variation, which corresponds to which day the depositions were performed (and presumably to the ambient temperature outside the chamber on those days), suggests that heating below 40°C is insufficient to overcome the effect of the ambient temperature on the chamber temperature.

Figure 6 shows the effect of heating pad temperature on the resulting coating chemistry for both 10- and 20-minute depositions. The coatings deposited for ten minutes show only moderate dependence of ether content on temperature, while the

coatings deposited for 20 minutes exhibit a clear increase in ether content with increasing temperature up to 50°C. The lower temperature dependence of the ether content of the ten-minute depositions likely reflects the fact that shorter deposition times produce thinner coatings, and it is more difficult to detect differences between thinner coatings. In addition, the carbonyl content decreases substantially with increasing chamber temperature regardless of deposition time. Therefore, a heating pad temperature of 50°C was used for all subsequent depositions, including all pins for pin-on-disk wear testing.

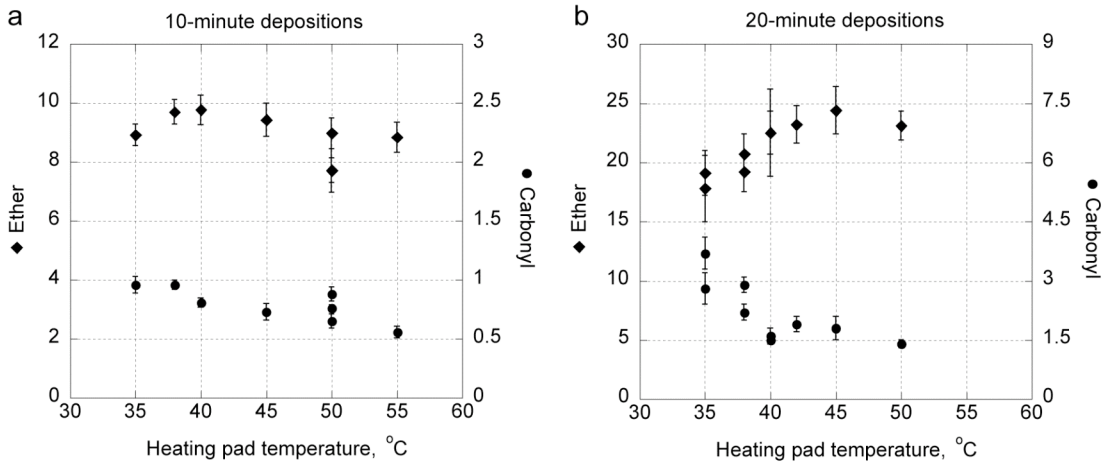

Figure 6: The effect of heating pad temperature on the ether and carbonyl contents of films deposited for a) 10 minutes and b) 20 minutes. All data represent the areas under the ether or carbonyl peaks of the ATR-FTIR spectra of the coatings. All processes were performed at 50 W with 6 ml/hr tetraglyme inflow.

Sample position

Since the composition of the plasma is spatially dependent, the plasma deposition process can vary with sample position in the deposition chamber (the entire shelf used in the deposition process was powered, so plasma power should not have varied significantly within the area of the chamber used for depositions). In the system used

here, the precursor enters the chamber from a point source in the top left corner of the chamber and then disperses by a combination of diffusion and vapor flow. To account for the effects of spatial variation on the plasma deposition processes, ATR-FTIR was performed on three different samples, which were usually taken from the front left, front right, and back center of the cluster of substrates deposited in each batch. This was intended to encompass the full range of possible coating outcomes of any given batch, but it also allowed for qualitative observation of the effect of substrate position on the coating chemistry. Preliminary observations suggested that the substrate closest to the tetraglyme intake valve (the substrate occupying the front left position) developed thicker coatings than those further away. Since this affected the inter- and intra-batch reproducibility of the process, the effect of sample position was investigated in more detail.

A special holder was machined to facilitate tetraglyme deposition on the pins used for the pin-on-disk wear tests. The holder, shown in Figure 7, consists of a block of aluminum with five sets of three holes in a row, such that up to fifteen pins could be coated during a single deposition, with additional space available around each row of pins to coat samples used for chemical characterization (ATR-FTIR, XPS, contact angle goniometry, and protein deposition).

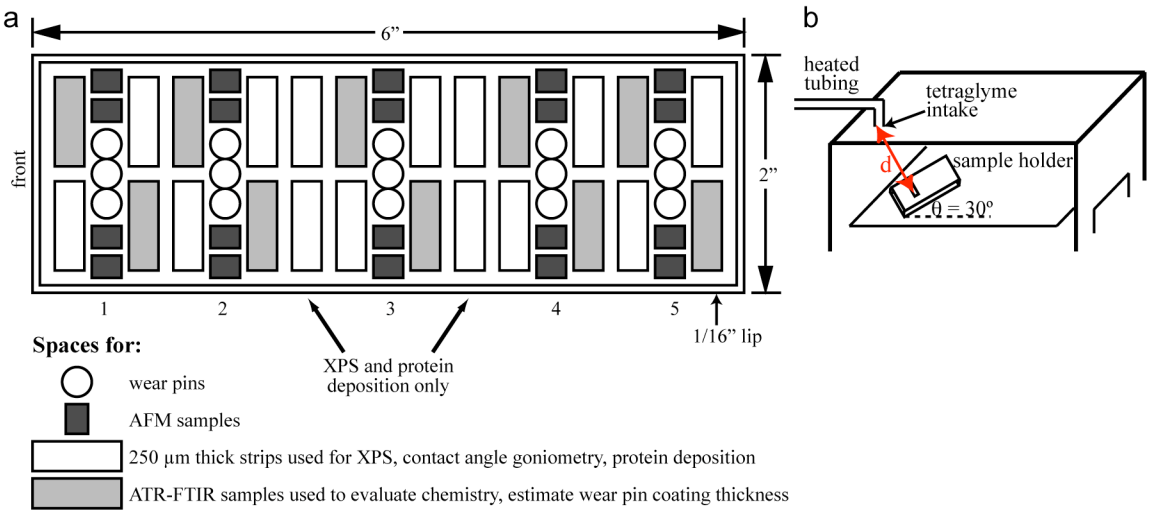

Figure 7: a) The holder used for plasma deposition of the pin-on-disk wear pins. Substrates intended for chemical characterization, AFM, and protein deposition surround each row of wear pins to generate surfaces that are maximally similar to the coatings on the wear pins. b) The placement of the holder within the plasma deposition chamber. The distance *d*, indicated in red, between the tetraglyme intake and the samples was varied to determine the effect of sample position on coating chemistry and thickness.

For these depositions, the position of the holder on the top shelf in the plasma chamber was marked so that the holder was located in the same place for every deposition, and the substrates were located in the same place on the holder (the shaded strips in Figure 7a). This enabled a quantitative study of the effect of substrate location on the deposition process. The results appear in Figure 8.

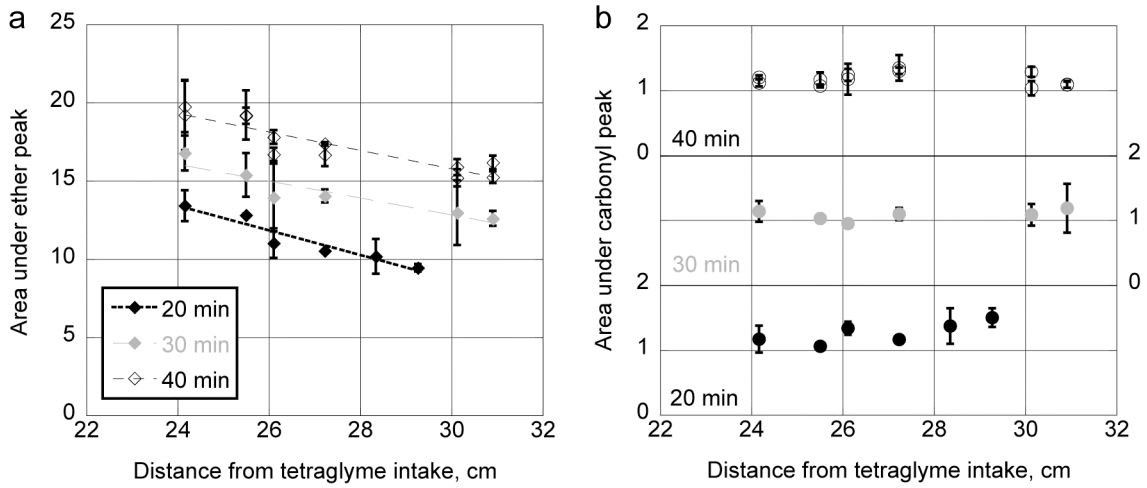

Figure 8: The effect of sample position on the chemistry of coatings deposited for 20 minutes (black), 30 minutes (grey), or 40 minutes (white) at 50 W, 6 ml/hr tetraglyme flow, with 50°C heating pads. The x axes are the distance *d* shown in Figure 7b. The carbonyl data in part b was separated by deposition time for ease of visualization. It is important to note that in these plots, unlike all others presented in this chapter, each data point represents the mean value of peak areas from ATR-FTIR spectra taken at two spots on a single substrate, rather than three substrates.

Preliminary results indicated that the deposition results varied widely across the first row of pins (the row closest to the tetraglyme intake), so these positions –the three pin slots in the first row and the adjacent spaces for four AFM samples and four thin UHMWPE strips – were not used for subsequent depositions.

The carbonyl content of the coatings appears to be independent of both the distance from the tetraglyme intake and the deposition time, but substrate position within the plasma deposition chamber clearly affects the ether content of the coatings: the area under the ether peak decreases with increasing distance from the tetraglyme intake regardless of the deposition time. The ether content can be modeled as linearly dependent on *d* according to the equation

$$E = md + b \qquad [1],$$

where E is the ether peak area, m is the slope, and b is the y-intercept. This yields the curve fits shown in Table 1. While these fits are acceptable, the R^2 values indicate that they are not ideal, and are less reliable with increasing deposition time. However, they are important for two reasons.

Table 1: Linear fit parameters for sample location versus ether peak area

Deposition time, min	Slope m	Y-intercept b	R^2
20	-0.79	32.3	0.91
30	-0.54	29.0	0.85
40	-0.59	33.4	0.83

First, chemical characterization was not performed directly on the wear pins, as most of the characterization techniques are destructive. Instead, as Figure 7a shows, the substrates adjacent to the wear pins were characterized, and the results were assumed to be representative of the pins as well. In particular, the ATR-FTIR spectra of the substrates to the front left and back right of the pins were averaged to estimate the thickness of the three pins in between, a method that assumes a linear relationship between substrate location and ether peak area (shown in Chapter 5 to be directly proportional to coating thickness). Since the data in Figure 8 show that the relationship is in fact roughly linear, this assumption is valid and the estimates of the wear pins coating thicknesses should be reasonable. In addition, since the coating thickness is directly proportional to the ether peak area, and the ether peak area can be estimated from the fits shown in Table 1, these fits can be used to approximate the substrate location necessary to produce coatings of a desired thickness.

Deposition time

The data shown in Figure 3 (unheated chamber) and Figure 8 (50°C heating pads) suggest the effects of deposition time on coating chemistry and thickness; in particular, it is clearly evident from both figures that the ether content of the coatings increases with increasing deposition time. The relationship between deposition time and coating chemistry/thickness is explored in more detail in Figure 9. Figure 9a presents a series of depositions performed for 2-30 minutes with 40°C heating pads, while Figure 9b recasts the results shown in Figure 8 to highlight the effect of deposition time. The primary purpose of taking ATR-FTIR spectra of these particular samples was to calculate the thickness of the PEG-like coatings on the wear pins that they flank; therefore, the results shown in Figure 9b are the averages of the front-left and back-right substrates represented individually in Figure 8.

In all cases, the ether content of the coatings increases linearly with increasing deposition time, and the fits are very good. These results, in conjunction with the coating thickness measurements presented in Chapter 5, clearly demonstrate that the coating thickness increases linearly with deposition time. Although the deposition rate, indicated by the slopes of the curve fits, depends on the temperature of the heating pads, the linear nature of the deposition process with time is independent of both chamber temperature and sample position.

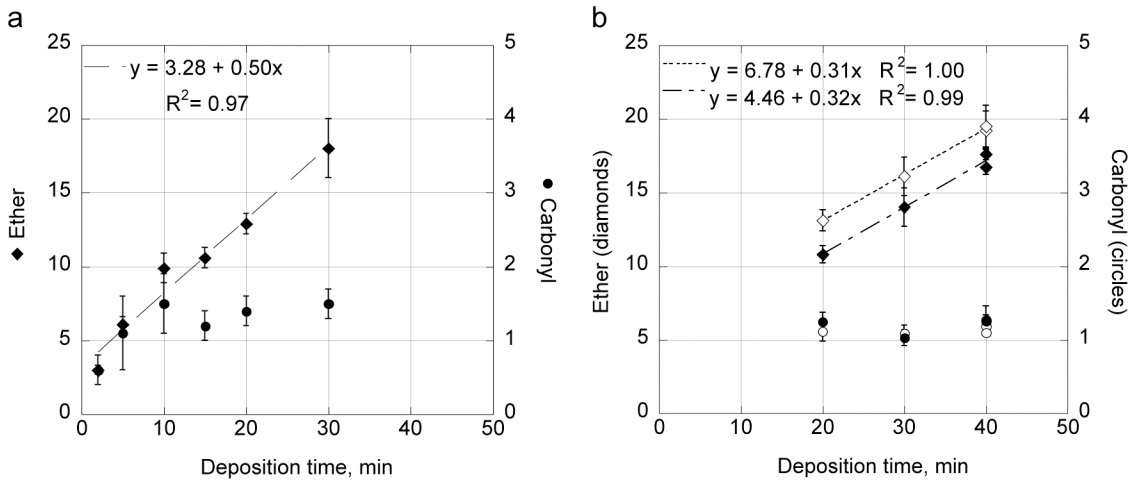

Figure 9: The effect of tetraglyme plasma deposition time on the chemical composition of coatings produced at a) 40°C and b) 50°C. The two sets of data in part b represent the results from samples at two different positions on the sample holder: the shaded strips adjacent to the wear pins in row 2 (see Figure 7a; open symbols), and row 3 (closed symbols). As in all plots in this chapter, diamonds indicate the area under the ether peak, while circles represent the area under the carbonyl peak. Depositions were performed at 50 W with 6 ml/hr tetraglyme flow.

The effect of deposition time on the carbonyl content of the coatings is somewhat more complicated. While the carbonyl content increases with increasing deposition time initially (for 2-10 minute processes), the carbonyl presence then levels off, remaining relatively constant for longer depositions (10-40 minutes). The fact that the carbonyl content stops increasing with coating thickness suggests that the formation of carbonyl species occurs early in the deposition process, such that most of the carbonyl species exist in an intermediate layer between the UHMWPE surface and a purer PEG-like coating.

In combination, the ether and carbonyl results indicate that the most PEG-like surfaces are produced from depositions at least ten minutes long. The thickness varies predictably as a function of both deposition time and substrate location within the

chamber, and either or both can be manipulated to produce surfaces of comparable chemistry and varying thickness.

Conclusions

Tetraglyme plasma deposition is a complex, multivariate process. The studies presented in this chapter were intended to evaluate the effects of certain critical variables – flow rate, power, temperature, position, and time – in order to identify a set of plasma processing conditions that would produce coatings with consistent PEG-like chemistry. The effect of each processing parameter, as well as the final plasma processing parameters used to coat the substrates used for the wear tests presented in Chapter 6, are shown in Table 2.

Table 2: Tetraglyme plasma processing parameters

Plasma Processing Parameter	Effect on Coating	Setting to Produce Wear Testing Samples
Tetraglyme flow rate	Excessively low and high flow rates produce inconsistent coating chemistry, which likely results from variations in the tetraglyme plasma vapor concentration.	6 ml/hr (through 130°C heated tubing, with additional argon gas flow through the tubing)
Power	Very high power (>200 W) yields non-PEG-like chemistry. Effects at lower power (30-100 W) are confounded by chamber temperature and merit further investigation.	50 W
Heating pad temperature	Increasing the chamber temperature decreases the carbonyl content of the coatings, producing more PEG-like chemistry.	40°C (some AFM wear testing samples) 50°C (some AFM wear testing samples, all pin-on-disk samples)
Substrate position	Coating thickness decreases linearly with increasing distance from the tetraglyme intake valve. A minimum distance *d* of ~24 cm is necessary to avoid substantial variations in deposition results.	Wear pins placed in slots 2-5, surrounded by substrates used for chemical characterization and nanotribology experiments
Deposition time	Coating thickness increases linearly with deposition time. Carbonyl content increases with deposition time up to ~10 minutes; longer depositions have relatively constant carbonyl content.	2-30 minutes (AFM wear testing samples) 20-40 minutes (pin-on-disk samples)

These deposition parameters produce coatings with consistent PEG-like chemistry and varied thickness, but they do not represent a fully optimized plasma process. If a tetraglyme-based coating were adopted for a commercial product, the plasma process would have to be optimized to ensure uniform coating chemistry and thickness across the entire acetabular cup, improve batch-to-batch reproducibility of the chemistry and thickness, and minimize the deposition time for a given coating thickness.

References

1. Rossnagel, S.M., J.J. Cuomo, and W.D. Westwood, eds. *Handbook of Plasma Processing Technology*. 1990, Noyes Publications: Park Ridge, NJ.
2. Bunshah, R.F., ed. *Handbook of Deposition Technologies for Films and Coatings*. 2nd ed. 1994, Noyes Publications: Park Ridge, NJ.
3. Laroussi, M., *Low temperature plasma-based sterilization: Overview and state-of-the-art.* Plasma Processes and Polymers, 2005. **2**(5): p. 391-400.
4. Lopez, G.P., et al., *Glow-Discharge Plasma Deposition Of Tetraethylene Glycol Dimethyl Ether For Fouling-Resistant Biomaterial Surfaces.* Journal Of Biomedical Materials Research, 1992. **26**(4): p. 415-439.
5. Lopez, G.P. and B.D. Ratner, *Molecular Adsorption and the Chemistry of Plasma-Deposited Thin Organic Films: Deposition of Oligomers of Ethylene Glycol.* Plasmas and Polymers, 1996. **1**(2).

6. Johnston, E.E., J.D. Bryers, and B.D. Ratner, *Plasma deposition and surface characterization of oligoglyme, dioxane, and crown ether nonfouling films.* Langmuir, 2005. **21**(3): p. 870-881.

7. Gref, R., et al., *'Stealth' corona-core nanoparticles surface modified by polyethylene glycol (PEG): influences of the corona (PEG chain length and surface density) and of the core composition on phagocytic uptake and plasma protein adsorption.* Colloids Surf B Biointerfaces, 2000. **18**(3-4): p. 301-313.

8. Ostuni, E., et al., *A survey of structure-property relationships of surfaces that resist the adsorption of protein.* Langmuir, 2001. **17**(18): p. 5605-5620.

9. Harder, P., et al., *Molecular conformation in oligo(ethylene glycol)-terminated self-assembled monolayers on gold and silver surfaces determines their ability to resist protein adsorption.* Journal of Physical Chemistry B, 1998. **102**(2): p. 426-436.

10. Moro, T., et al., *Surface grafting of artificial joints with a biocompatible polymer for preventing periprosthetic osteolysis.* Nature Materials, 2004. **3**(11): p. 829-836.

Chapter 4

Chemical Characterization

Introduction

Poly(ethylene glycol), or PEG, is a flexible linear polymer comprised of CH_2CH_2O repeat units, as shown in Figure 1. PEG has been extensively studied for several decades because it is hydrophilic, biocompatible, and resistant to protein and cell deposition. Collectively, these traits render it attractive for a wide range of applications. In vivo, PEG is valued for its ability (conferred by its resistance to protein deposition) to evade detection and uptake by the immune system. This has led to several therapeutic applications: PEGylation of drugs, particularly peptides and proteins, to reduce antigenicity and enzymatic degradation, and to increase their half-life in the bloodstream [1, 2]; and PEG-coated liposomes, again to increase their half-life in the bloodstream [3, 4]. In vitro, PEG enables surface patterning and functionalization for cell and tissue culture studies. For example, proteins, peptides, and other biomolecules are often conjugated to PEGylated surfaces to present specific signals for behaviors such as attachment, spreading, proliferation, and differentiation [5, 6]. These functionalized

surfaces offer potential as tissue engineering constructs for growing tissue in vitro or healing defects in vivo.

Since protein resistance makes PEG so useful, it was the focus of much of the research on PEG and related materials in the 1990s and early 2000s. In 1991, Jeon et al proposed a model for PEG-protein interactions based on two opposing forces, steric repulsion and hydrophobic attraction [7, 8]. Steric repulsion has two components: an unfavorable decrease in entropy from the protein encroaching on the polymer chains and reducing the number of conformations that are possible, and an unfavorable decrease in enthalpy if water molecules in the hydration layer around the PEG chains are expelled into the bulk aqueous solution, which goes against the osmotic gradient of the system. Hydrophobic attraction results from favorable interactions between induced dipoles in the hydrophobic portions of the protein and PEG molecules.

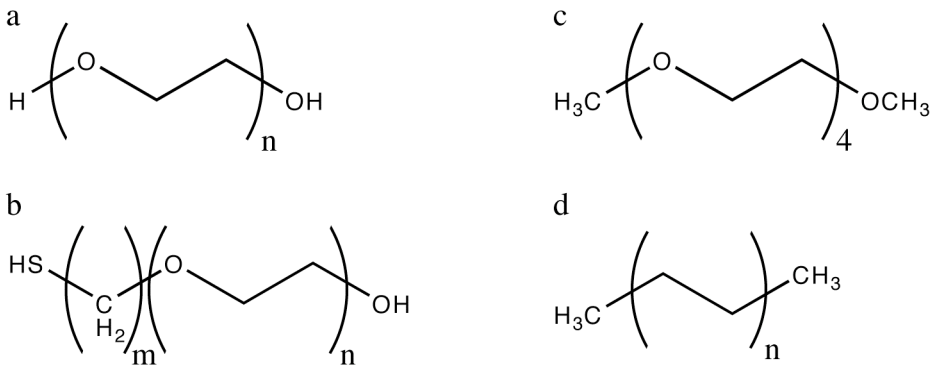

Figure 1: The chemical structures of a) poly(ethylene glycol), b) a generic oligo(ethylene glycol) SAM structure, c) tetraglyme, and d) polyethylene.

Shortly after Jeon's work was published, Prime and Whitesides introduced a model system for experimental studies of surface-protein interactions [9]. Called self-

assembled monolayers (SAMs; see Figure 1), these surfaces typically consist of short segments of molecules of interest attached to alkanethiol tail groups that spontaneously assemble into ordered surfaces on gold and silver. These surfaces allow for control of the length of each segment of the molecule, the chemical structure of the non-alkane segment, as well as the head group chemistry, and enable the formation of mixed surfaces displaying a combination of different groups. In addition, gold and silver substrates enable the use of surface plasmon resonance to accurately detect very low levels of adsorbed protein [10].

A study of SAMs with a wide variety of head group chemistries yielded four molecular characteristics common to SAMs components that resisted protein deposition: i) hydrophilicity, ii) presence of hydrogen bond acceptors, iii) absence of hydrogen bond donors, and iv) charge neutrality [11]. Although the requirements for hydrogen bond acceptors versus donors are unexpected, these results otherwise agree well with the model proposed by Jeon et al – surfaces that adsorb or hydrogen bond to water have the potential for enthalpic resistance to protein deposition, while surfaces that are less hydrophobic minimize the potential for hydrophobic attraction to protein.

Computational modeling [12, 13] and experimental investigation [14, 15] of the conformation of oligo(ethylene glycol) SAMs independently confirmed the importance of water infiltration into the ethylene glycol portion of the surface and indicated that conformational flexibility was necessary to allow for sufficient reordering of the surface to enable hydrogen bonding. In conformations that do not allow for sufficient water infiltration and hydrogen bonding, oligo(ethylene glycol) SAMs adsorb protein.

Unfortunately, SAMs function well as model surfaces, but are limited to certain substrates (gold, silver, glass) and are not robust enough for use in most medical implants. The goal of this project is to improve lubrication at the surface of the ultrahigh molecular weight polyethylene (UHMWPE) for use in acetabular cups in total hip replacements. PEG offers a number of previously-mentioned advantages, including biocompatibility, hydrophilicity, and resistance to protein deposition and phagocytosis. It is also lubricious [16, 17]. However, covalently attaching PEG to the UHMWPE surface is difficult because the surface is chemically inert, consisting entirely of CH_2 repeat units. Consequently, a different method was chosen: plasma polymerization of an ethylene glycol oligomer, tetraglyme (see Figure 1).

The Ratner group first proposed tetraglyme-based coatings as a PEG alternative in 1992 [18], and has since evaluated the effect of different plasma processing parameters [19, 20] and monomer structure [19, 21] on the resulting chemistry and protein adsorption. In addition, they have assessed the behavior of plasma-polymerized tetraglyme coatings (the most protein-resistant of the various surfaces studied) in vitro [22-24], ex vivo [23], and in vivo [25], with largely promising results – decreased protein and cell adhesion, and decreased thrombogenicity – although more extensive in vivo data is needed. For this work, however, one of the most important findings was the correlation between surface ether content (characteristic of the PEG chemical structure) and protein deposition resistance. Shen et al [22] and Cao et al [20] both found that surfaces with at least 66% ether content resisted protein and cell deposition.

In this work, plasma polymerizing tetraglyme onto the UHMWPE surface is intended to produce a covalently-bonded coating that retains the chemical structure, and

therefore beneficial traits, of poly(ethylene glycol), but is crosslinked for increased mechanical strength. To verify the chemistry of the coatings produced by plasma deposition, the samples were characterized with several standard surface-specific techniques – ATR-FTIR, XPS, and contact angle goniometry. In addition, the surfaces were exposed to fluorescently-labeled protein and then examined by fluorescence microscopy to evaluate their ability to resist protein deposition.

Two different sets of samples were evaluated: coatings produced at 40°C and 50°C. The coatings generated at 40°C were used for most of the AFM scratching experiments, which generated the thickness calibration curve discussed in Chapter 5; the microscopic wear behavior of these coatings is presented in Chapter 6. Since ATR-FTIR results indicated that the chemistry of the coatings generated at 40°C was slightly less PEG-like than that of coatings produced at higher temperatures (see Chapter 3), no wear pins were PEGylated at 40°C. Instead, all wear pins were coated at 50°C. AFM scratch testing was performed on substrates coated during the wear pin depositions as well. The results of the AFM thickness measurements appear in Chapter 5, while the microscopic wear behavior is presented in Chapter 6.

Since the plasma polymerization conditions differed for the two sets of samples and ATR-FTIR results indicated a higher carbonyl content for the samples produced at lower temperatures, full chemical characterization – ATR-FTIR, XPS, contact angle goniometry, and protein deposition – was performed on both sets of samples, and the results are presented in parallel in this chapter.

Materials and Methods

UHMWPE substrates

To accommodate the roughness and geometric requirements of different testing methods, plasma deposition was performed on three different types of UHMWPE substrates. For AFM (see Chapters 5 and 6), blocks with dimensions 3 mm x 3 mm x 5 mm were cut from bar or rod stock UHMWPE, and the 3 mm x 5 mm faces were microtomed with a Reichert Ultracut E instrument to minimize surface roughness. For pin-on-disk wear testing (see Chapter 6), pins with length 19.05 mm, diameter 6.35 mm, and end radius of curvature 3.175 mm were machined from rod stock UHMWPE, and a 2mm diameter flat was microtomed into one end to form the articulating surface. For ATR-FTIR, XPS, contact angle goniometry, and protein deposition experiments, 20 mm x 5 mm strips were cut from a 250 μm thick sheet of UHMWPE. All UHMWPE came from McMaster-Carr, and all substrates were cleaned by successive sonication in 1% Aquet solution (Bel-Art Products), deionized water 3x, acetone, and isopropanol (Sigma-Aldrich).

During each plasma deposition, thin-strip specimens were placed adjacent to AFM blocks and wear pins. For batches without wear pins, strips located at the front left, front right, and back center of the cluster of substrates were used for ATR-FTIR characterization of the entire batch, while more central strips were used for XPS, contact angle, and protein deposition measurements. For batches with wear pins, the substrates were distributed as shown in Figure 2.

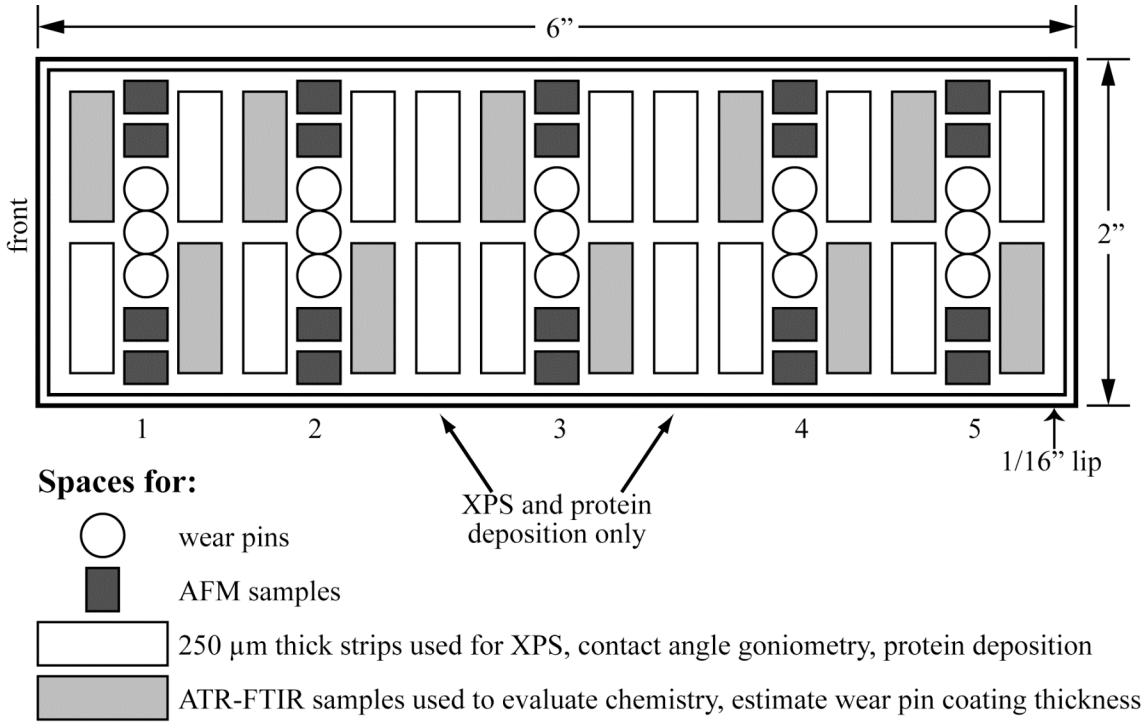

Figure 2: The location of each substrate type on the holder used for plasma deposition onto wear pins. For most batches, no more than three rows contained wear pins, and only the adjacent spaces for thin strips and AFM samples were used. XPS and protein deposition samples representative of the entire batch were placed only in one of the two rows indicated.

Plasma deposition

The plasma deposition process is described in detail in Chapter 3. Briefly, the substrates were coated with plasma-polymerized tetraglyme (Sigma-Aldrich) using a Plasma Science PS0500 instrument with a 550 W generator. The chamber was pumped down to 30 mTorr base pressure before each step of the process. High-power argon treatment (400 W, 250 sccm, 3 minutes) was used to activate the UHMWPE surface to promote covalent bonding of the coating. Tetraglyme was then plasma-polymerized onto the surface at 50 W, 30 sccm argon, with 6 mL/hr tetraglyme flow through a 130°C heating tube, for 2-40 minutes to generate a range of coating thicknesses. Afterward, the

chamber was flushed with argon (no power, 250 sccm, 1 minute) three times before the samples were removed. During the entire plasma process, the walls of the chamber were heated to 40°C produce the set of samples used to construct the thickness calibration curve (see Chapter 5) and 50°C to coat all wear pins. AFM scratch testing was performed on samples from both batches.

The thin strips used for ATR-FTIR, XPS, contact angle goniometry, and protein deposition were slightly curved. The convex side always faced upward during plasma polymerization, and all characterization experiments were performed on this side only.

ATR-FTIR

ATR-FTIR spectra were collected with a Nicolet Avatar 360 with an Omni-Sampler ATR accessory (Ge crystal, single-bounce beam path, 45° incident angle, 32 scans). For each plasma deposition batch without wear pins, spectra were collected at two spots on three strips, and the results of the six spectra were averaged to determine metrics for the batch as a whole. For wear pin depositions, spectra were collected at two spots on two strips adjacent to each pin (see Figure 2), and the results of the four spectra were averaged to determine metrics for each row of pins.

An advanced ATR correction was applied to all spectra and the region from 1800 cm^{-1} to 900 cm^{-1} was peak fit using Omnic 7.3 software. For coated samples, this region usually contained ten peaks: one carbonyl (~1730 cm^{-1}); another carbonyl or hydroxyl (1620-1650 cm^{-1}, always very small); one hydrocarbon doublet (modeled as a single peak at ~1465 cm^{-1}); and seven ether peaks from 940-1370 cm^{-1}. The areas under the most

prominent ether peak at ~1115 cm^{-1} and the main carbonyl peak at 1730 cm^{-1} were used to quantitatively compare the chemistries of different coatings.

XPS

XPS was performed on a Surface Science Instruments S-probe spectrometer with a monochromatized Al source at a 55° take-off angle (sampling depth 5-10 nm; spot size ~800 μm). For each plasma deposition batch, survey and high-resolution C1s spectra were collected at two spots on two samples, and the results were averaged to determine metrics for the batch. High-resolution C 1s spectra were peak fit with the Service Physics ESCAVB Graphics Viewer to resolve the hydrocarbon, ether, and carbonyl peaks.

Contact angle goniometry

The relative hydrophilicity of the surfaces was measured using a custom-made contact angle goniometer with a variable-magnification InfiniVar video microscope (Infinity Photo-Optical Co.), a 1.45 megapixel Sony XCD-SX910 camera, and LabView 7.1 software. 5 μL of deionized water was dropped onto the surface using a pipet, the drop was imaged using the video mode of LabView, and the static contact angle was calculated by the tangent chord theorem. Contact angle goniometry was performed at two spots on two samples per plasma deposition batch.

Statistical analysis of XPS and contact angle data

Analysis of variance (ANOVA) was used to test two hypotheses: that plasma deposition *time* had a significant effect on surface chemistry and hydrophilicity, and that

plasma deposition *temperature* had a significant effect on surface chemistry and hydrophilicity. All data for a given plasma deposition batch was assumed to be independent, and ANOVA was performed stepwise:

1. F test on all plasma batches produced at a given deposition temperature: 40°C or 50°C
2. If the F test showed that at least one batch was significantly different, the Holm *t* test was performed on all pairs of batches to determine which were different (and therefore time dependent); single batches significantly different from the rest of the coatings produced at that temperature were removed from the group
3. F test of the three resulting groups: uncoated, coated at 40°C (or subset), coated at 50°C (or subset)
4. If the F test showed that at least one group was significantly different (and therefore temperature dependent), the Holm *t* test was performed on all pairs of groups to determine which were significantly different.

Protein adsorption and fluorescence microscopy

Protein adsorption experiments were performed by exposing untreated and PEGylated UHMWPE substrates to a solution containing fluorescently-labeled protein (bovine serum albumin conjugated to AlexaFluor 488, BSA-AF, Invitrogen) and then visualizing the surfaces with a fluorescence microscope (Zeiss AxioImager M1 with Zeiss Plan-Neofluar 20x air objective, NA=0.50) to quantify the level of fluorescence. Albumin was chosen because it is the most common protein in synovial fluid [26]; the

AlexaFluor 488 fluorophore was chosen because its emission wavelength differs from the background fluorescence from the UHMWPE.

For all experiments, each sample strip was placed in a centrifuge tube containing 1 mL of BSA-AF solution or PBS for 30 minutes at room temperature. Each sample was then removed from the protein solution, and rinsed three times in 1 mL of PBS. The samples were mounted on clean microscope slides with coverslips, using 20 μL of PBS as the mounting medium. The BSA-AF was visualized at five spots on each substrate by exciting the fluorophore for seven seconds (filters: excitation 450-490 nm, emission 500-550 nm, both band pass), then imaging the surface with a Photometrics Quantix KAF1401E CCD camera and iVision 4.0 software (BioVision Technologies). The fluorescence intensity at a given spot was calculated as the mean of the brightness of the 1,363,095 pixels of each image.

To determine the detection limits of the system, untreated UHMWPE was exposed to solutions of BSA-AF in phosphate-buffered serum (Gibco, pH 7.4) with BSA-AF concentrations of 0 (pure PBS), 0.001, 0.01, 0.1, 1, 10, and 100 μg/mL. Based on the results of this experiment, untreated UHMWPE and PEGylated samples were exposed to 5 μg/mL of BSA-AF in PBS.

Results and Discussion

ATR-FTIR

ATR-FTIR identifies all infrared-active chemical bonds present in a sample and enables quantitative comparisons between surfaces. For the plasma-polymerized tetraglyme coatings, the primary bonds of interest are ether, indicative of the desired

PEG-like chemistry, and carbonyl, indicative of undesired secondary reactions. Hydrocarbon bonds derive from both the untreated UHMWPE substrate and the polymerized tetraglyme, and therefore provide limited information.

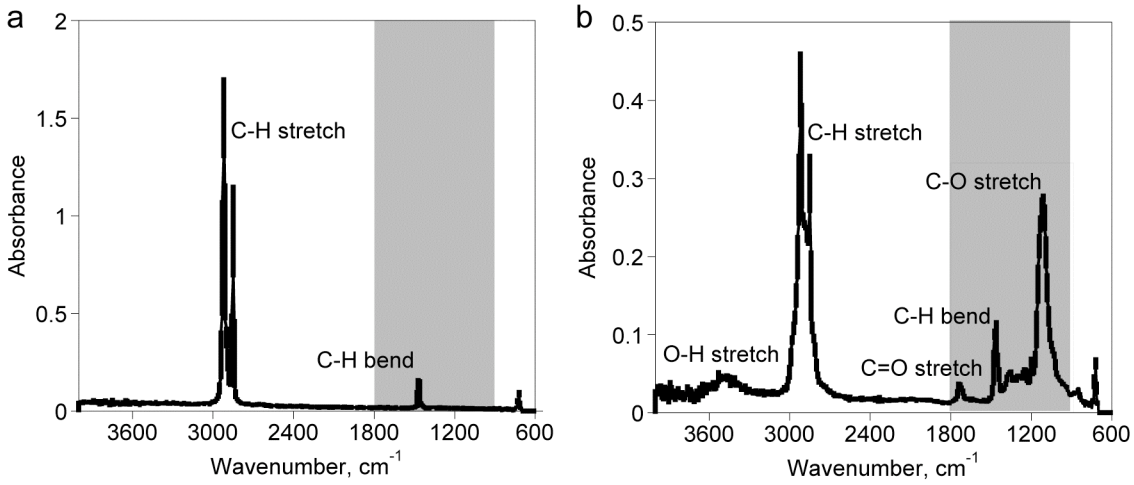

Figure 3: The full ATR-FTIR spectra of a) untreated UHMWPE and b) UHMWPE plasma-treated with tetraglyme for 30 minutes at 40°C. The grey boxes represent the region that was peak fitted for quantification of the ether and carbonyl peaks.

Figure 3 shows the full ATR-FTIR spectra of two surfaces: cleaned, untreated UHMWPE, and a PEG-like coating produced at 40°C for 30 minutes. As expected, the untreated UHMWPE exhibits only peaks associated with hydrocarbons, namely the C-H stretch and bend, while the PEGylated surface also displays a cluster of peaks from ether groups, the characteristic carbonyl stretch, and a broad hydroxyl (O-H) stretch. The absence of ether and carbonyl groups in the untreated UHMWPE indicates that the material was not oxidized before plasma treatment, while the presence of the ether group after plasma treatment indicates that the surface was successfully PEGylated. As discussed in Chapter 3, the carbonyl group forms during the tetraglyme deposition, and

one criterion for choosing the plasma parameters was to minimize the amount of carbonyl in the coating.

The final peak of note in the PEGylated sample spectrum is the hydroxyl stretch around 3500 cm^{-1}. Since tetraglyme, unlike PEG, terminates in a methoxy ($-OCH_3$) group rather than a hydroxyl, this peak does not derive from the expected chemical structure of the coating. It is possible that hydroxyl groups, like carbonyls, form during the deposition process, either from fragmented tetraglyme or from residual oxygen adsorbed to the chamber walls; if so, this change should render the coating more hydrophilic, and possibly more PEG-like. Alternatively, since the coating is hydrophilic, the hydroxyl peak may represent absorbed water contained within the coating. Either result would be beneficial.

Figure 4a shows the results of peak fitting the region from 1800 cm^{-1} to 900 cm^{-1} to quantify the ether and carbonyl content of the coatings. This region usually contained ten peaks: one carbonyl (~1730 cm^{-1}); another carbonyl or water (1620-1650 cm^{-1}, always very small); one hydrocarbon doublet (modeled as a single peak at ~1465 cm^{-1}); and seven ether peaks from 940-1370 cm^{-1}. Of these, the areas under the carbonyl peak at ~1730 cm^{-1} and the most prominent ether peak at ~1115 cm^{-1} were used for quantification.

At both 40 and 50°C, the ether content of the coatings increases linearly with increasing deposition time (Figure 4b and c), indicating that the coatings are becoming thicker, enriched in ether bonding, or both; ATR-FTIR cannot be used to distinguish between these two possibilities. However, atomic force microscopy studies presented in

Chapter 5 show that the increase in ether content in the 40°C coatings is directly proportional to an increase in coating thickness.

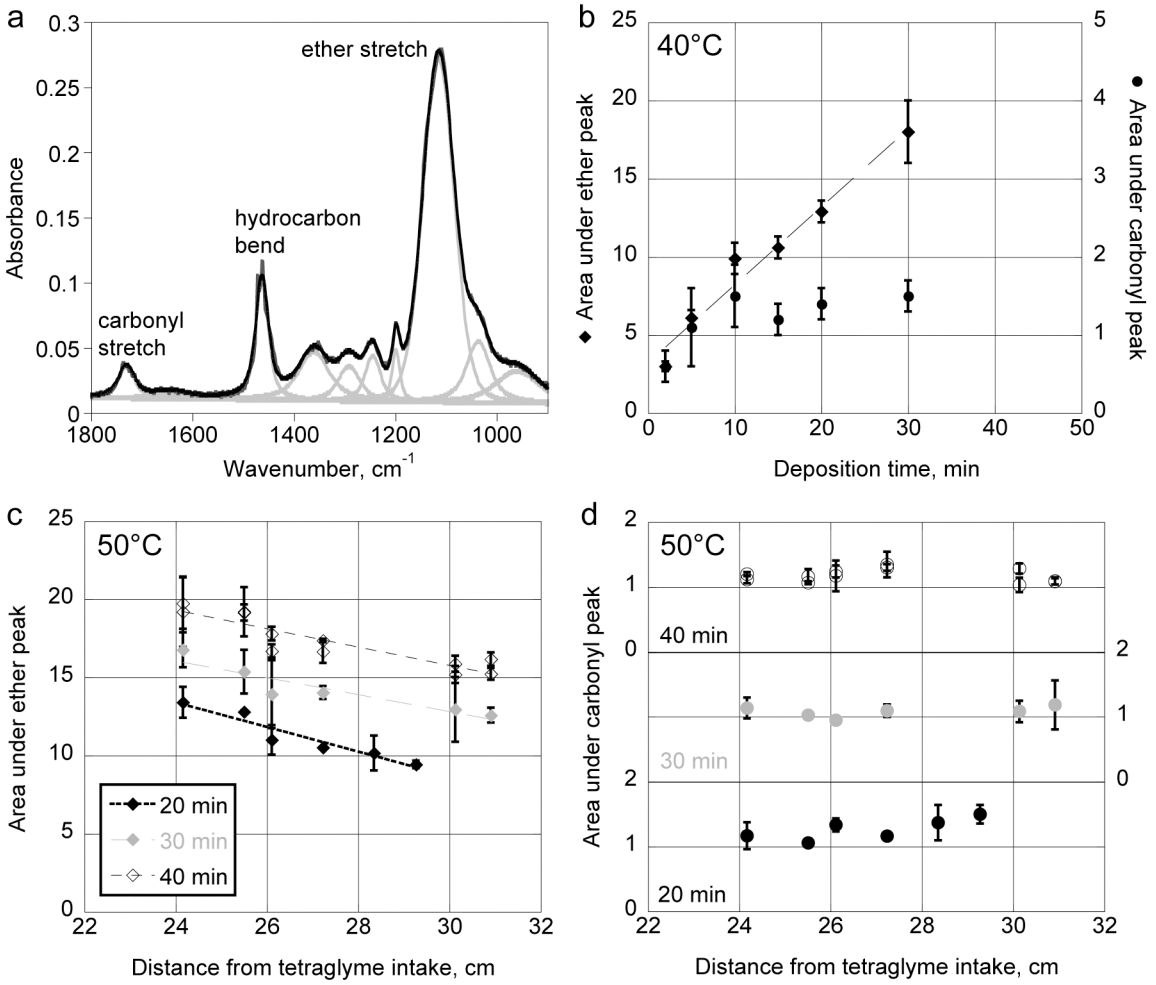

Figure 4: a) A representative ten-peak fit to the region of the spectrum from 1800 cm^{-1} to 900 cm^{-1}. The areas under the ether and carbonyl stretches were calculated from the peak fits and plotted in b-d. b) The chemistry of the coatings generated at 40°C. The ether content increases linearly with deposition time, as shown by the linear fit represented by the dashed line, while the carbonyl content increases only for the first ten minutes of the deposition. c) The ether content of the coatings generated at 50°C during 20-, 30-, and 40-minute depositions. Like the 40°C coatings, the ether bonding increases linearly with deposition time; however, as the dashed lines show, it also decreases linearly with increasing distance from the tetraglyme intake, a variable not examined at 40°C. d) The carbonyl content of the same 50°C coatings. Unlike the ether bonding, the carbonyl content remains relatively constant regardless of deposition time and sample position. All depositions were performed at 50 W.

For the 40°C depositions, the carbonyl content increases with increasing deposition time for about ten minutes, then levels off for longer processes. Since the coating thickness increases while the carbonyl content remains constant, it is likely that the majority of the carbonyl groups form during the first ten minutes of the deposition and are therefore concentrated closer the interface with the UHMWPE substrate in thicker coatings.

The 50°C depositions involved longer process times, 20-40 minutes. During these depositions, the carbonyl content of the coatings (Figure 4d) remains constant for all deposition times and substrate locations. This confirms that, as in the 40°C depositions, the carbonyl content does not depend on coating thickness, since the thickness increases with increasing deposition time and decreases with increasing distance from the tetraglyme intake.

XPS

The XPS results for selected samples are shown in Table 1 and Table 2. For comparison, the results for cleaned, untreated UHMWPE appear in the first line of both tables. The untreated substrates exhibit very slight oxidation (about 4%), which was usually below the detection limit of the ATR-FTIR. The plasma-treated surfaces look markedly different. As expected for a PEG-like chemical structure (see Figure 1), the ratio of carbon to oxygen of the surfaces is roughly 2:1, and the surfaces have greater than 70% ether (C-O) bonding. These results correlate well with both the expected

chemical structure and the literature values for plasma-polymerized tetraglyme coatings [21].

Table 1: XPS results for samples plasma treated at 40°C

Tetraglyme Deposition Time (min)	Coating Thickness (nm)	Composition		C1s bonding		
		% C 285 eV	% O 533 eV	% CH_x 285.0 eV	**% C-O 286.5 eV**	% C=O 288.0 eV
0	N/A	96.6 (0.6)	3.5	95.7 (1.6)	**4.0 (1.4)**	0.4 (0.8)
2	29[a]	69.8 (0.7)	30.2	18.4 (4.3)	**74.6 (3.7)**	7.0 (1.1)
5	64[a]	69.5 (0.8)	30.5	15.6 (1.1)	**78.3 (1.0)**	6.1 (0.9)
10	110[b]	70.2 (0.2)	29.8	19.7 (2.3)	**72.4 (2.6)**	7.9 (0.2)

All data shown are the mean values, with standard deviations in parentheses.
[a] Measured by atomic force microscopy
[b] Calculated from AFM calibration of ATR-FTIR data

Table 2: XPS results for samples plasma treated at 50°C

Tetraglyme Deposition Time (min)	Coating Thickness (nm)	Composition		C1s bonding		
		% C 285 eV	% O 533 eV	% CH_x 285.0 eV	**% C-O 286.5 eV**	% C=O 288.0 eV
0	N/A	96.6 (0.6)	3.5	95.7 (1.6)	**4.0 (1.4)**	0.4 (0.8)
20	113-133[a]	68.8 (0.6)	31.2	11.6 (0.9)	**83.2 (1.7)**	5.2 (0.8)
30	147-171[a]	69.0 (0.1)	31.0	12.2 (0.4)	**82.1 (0.6)**	5.7 (0.4)
40	189-206[a]	68.5 (0.3)	31.5	12.0 (0.7)	**82.5 (1.0)**	5.6 (0.4)

All data shown are the mean values, with standard deviations in parentheses.
[a] Calculated from AFM calibration of ATR-FTIR data; range is due to placement of the substrates on the deposition holder (see Figure 2)

It is interesting to note that the coatings produced at 50°C contain 5-10% more ether than the coatings produced at 40°C, as well as slightly less carbonyl. However, the

40°C coatings evaluated by XPS were also produced during shorter depositions than the 50°C coatings. Based on the ATR-FTIR studies of time and temperature effects on the plasma deposition process presented in Chapter 3, the decrease in carbonyl bonding likely stems from the increase in deposition temperature, since increased time produced the opposite effect, surfaces with equal or greater carbonyl content.

Since ATR-FTIR samples the entire thickness of the coatings, changes in the absorption of a bond present in the coating can reflect changes in either coating thickness or relative bond content within the coating. When the coating thickness increases and bond absorption decreases, as in the case of the carbonyl bond at increasing deposition temperatures, the change clearly results from a decrease in relative bond content. However, when both the coating thickness and the area under the ATR-FTIR peak increase, as in the case of ether bonding at increasing deposition time and temperature, the cause is not clear.

Therefore, changes in the ether content of the coating cannot be decoupled from changes in coating thickness using ATR-FTIR. However, the XPS results offer some insight. At both 40°C and 50°C, increasing deposition time does not increase ether content; at both temperatures, the difference between samples with different deposition times is not statistically significant ($p < 0.05$). However, the effect of deposition time is statistically significant (again, $p < 0.05$). The surfaces produced at 50°C all contain 82-83% ether, regardless of the deposition time, while the surfaces produced at 40°C exhibit more variation (likely due to their more varied positions within the deposition chamber), but all contain less ether, 72-78%. This indicates that the higher deposition temperature produces more PEG-like coatings, at least at the near surface. Since XPS probes only the

top 5-10 nm of the coating, it is impossible to know whether the differences in ether and carbonyl content between the samples produced at 40°C and 50°C exist throughout the thickness of the coatings.

The difference in information content between XPS and ATR-FTIR has additional implications. XPS is much more surface-sensitive than ATR-FTIR, probing a depth of a few nanometers as opposed to a few hundred microns. Since proteins and cells interact only with the upper surface (angstroms-nanometers) of materials to which they are exposed, XPS provides valuable information to predict these interactions. By contrast, ATR-FTIR characterizes the entire coating thickness, which is more likely to affect mechanical properties and tribological performance.

Contact angle goniometry

Contact angle goniometry measures the relative hydrophilicity of surfaces. Like XPS, contact angle goniometry measures only near-surface properties of materials since only the first few nanometers of material interact with the droplet. Consequently, the results should correlate well with the near-surface chemistry measured by XPS (which itself correlated to the temperature of the plasma deposition chamber), but should be independent of coating thickness. As Figure 5 shows, both of these expectations are observed. Untreated UHMWPE has a contact angle of 90.4°, while all PEGylated surfaces, with thicknesses ranging from 30-200 nm, exhibit much lower contact angles. The surface roughness does not change during the plasma deposition process, so the decrease in contact angle with tetraglyme plasma treatment should be entirely due to changes in surface chemistry. The dramatic reduction in contact angle after plasma

treatment clearly demonstrates that the PEGylated surfaces are, as expected, significantly more hydrophilic than unmodified UHMWPE ($p < 0.05$).

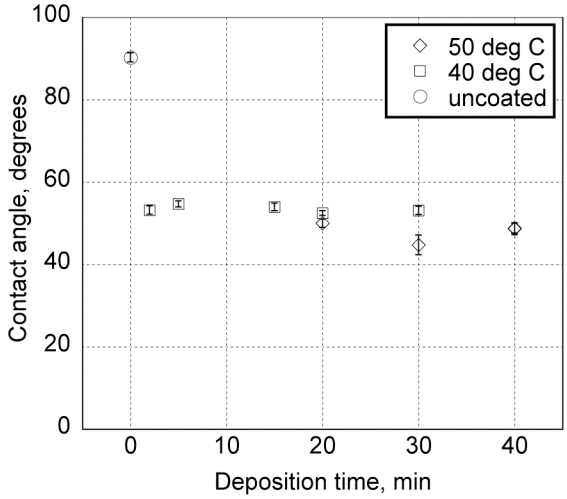

Figure 5: Contact angle results for samples produced at 40°C and 50°C, as well as uncoated UHMWPE. The difference between all three groups is statistically significant ($p < 0.05$).

At both 40°C and 50°C, changing the deposition time does not significantly change the contact angle ($p < 0.05$), except for the 50°C 30-minute samples, which exhibit a slightly lower contact angle than any other batch. This appears to be anomalous and is not reflected in the XPS results. However, the effect of deposition time is statistically significant ($p < 0.05$): the surfaces produced at 40°C have slightly higher contact angles (52.5°-54.3°) than those produced at 50°C (44.9°-50.0°). This finding agrees well with the XPS results. Ether and carbonyl bonds are hydrophilic, and hydrocarbon groups are hydrophobic. The surfaces produced at 40°C are 80-84% ether and carbonyl, while the surfaces produced at 50°C are 88% ether and carbonyl. The

greater percentage of hydrophilic bonds in the surfaces produced at 50°C renders these surfaces slightly more hydrophilic, such that they exhibit a slightly lower contact angle.

Protein adsorption

Precise quantification of adsorbed protein requires calibration of the detection system, which can be difficult for fluorescence microscopy. However, approximate quantification is fairly straightforward, and is sufficient to determine whether or not surfaces resist protein deposition. The protein deposition experiments therefore involved construction of an approximate calibration curve, followed by protein adsorption and imaging on a set of coated and uncoated samples. In all cases, uncoated UHMWPE substrates soaked in PBS for the duration of the protein exposure were used as negative controls.

If a protein-adsorptive surface is exposed to a range of concentrations of protein solution, the surface will typically adsorb protein linearly with increasing concentration until the surface is fully covered by a monolayer of protein molecules (in some cases, protein will continue to adsorb, forming multilayers). If the protein is fluorescently labeled, the fluorescence signal from the surface should therefore also increase steadily and then level out for exposure concentrations that yield monolayer adsorption. The working range for experiments intended to differentiate between surfaces is therefore the set of exposure concentrations that produce a fluorescence signal above background (the signal from unexposed samples such as the PBS soak controls) but below full monolayer coverage – the linear region of the adsorption plot.

From this information, it is not possible to calculate the actual weight or surface concentration of protein adsorbed; however, if the fluorescent signal is proportional to the amount of protein present, it is possible to determine the relative amount of adsorbed protein on different surfaces. The calibration curve in Figure 6a shows the fluorescence of uncoated UHMWPE substrates exposed to protein solutions with a range of concentrations of six orders of magnitude. Background fluorescence levels were measured on uncoated UHMWPE substrates exposed to PBS without protein.

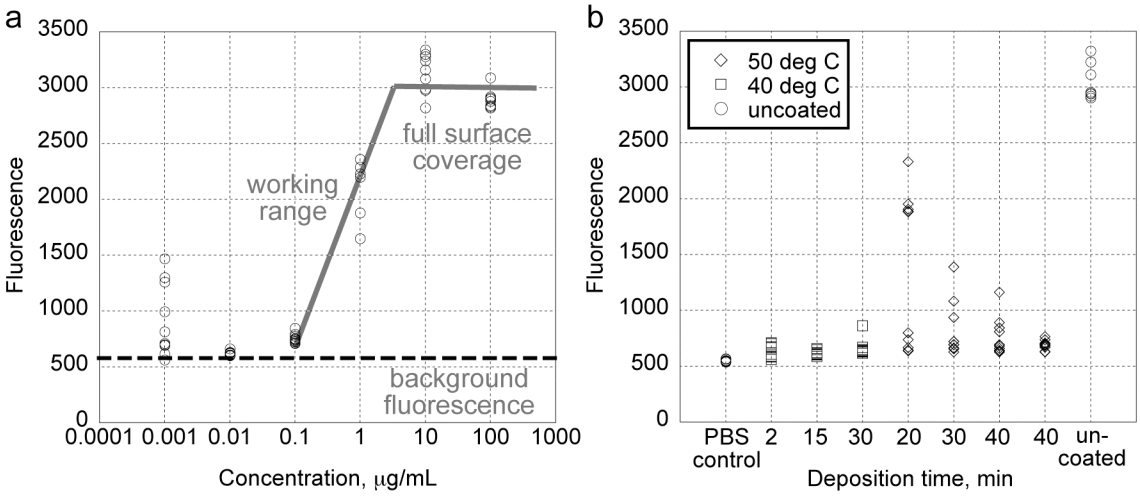

Figure 6: a) The protein adsorption calibration curve for uncoated UHMWPE. The dashed black line represents background fluorescence, while the grey lines are a visual aid that approximate the adsorption curve. The inflection point of the curve was placed at ~5 μg/mL rather than 10 μg/mL because of the fluorescence exhibited by the uncoated surface in b), which was exposed to 5 μg/mL. b) Protein deposition on uncoated UHMWPE and selected coatings generated at 40°C and 50°C. For each surface, the data points represent the mean fluorescence of five spots on two substrates from the same plasma deposition batch. For visual clarity, the standard deviations are not displayed. The background signal is indicated by the results of the PBS control, which was exposed to PBS solution without BSA-AF.

The uncoated surfaces exhibit the full range of expected adsorption behavior. Exposure concentrations of 0.01 μg/mL or less yield undetectable or unreliable results

(the wide range of fluorescence at 0.001 μg/mL likely results from protein clumping). Exposure concentrations of 0.1-10 μg/mL produce a log-linear relationship between adsorbed protein and fluorescence; this therefore constitutes the working range of the system. Exposure to a higher concentration, 100 μg/mL does not increase fluorescence, indicating that full monolayer coverage begins somewhere between 1 and 10 μg/mL. Based on these results, the coatings generated at 40°C and 50°C, as well as uncoated UHMWPE were exposed to 5 μg/mL BSA-AF.

As Figure 6b shows, all of the coated surfaces resist protein deposition, with most exhibiting levels that are close to the background fluorescence from the substrate (the PBS control). By contrast, the uncoated UHMWPE exhibits considerably higher fluorescence. According to the calibration curve in Figure 6a, protein becomes detectable for exposure solution concentrations between 0.01 and 0.1 μg/mL. Assuming that total protein adsorption on uncoated UHMWPE is linear with exposure concentration until a monolayer forms, the detection limit of the system can be approximated as the amount of protein adsorbed from ~0.05 μg/mL solution, two orders of magnitude lower than the concentration of the solution to which the 40°C and 50°C coatings were exposed.

The coatings produced at 40°C exhibit fluorescence levels very close to the detection limit of the system. They therefore reduced protein adsorption by approximately two orders of magnitude relative to uncoated UHMWPE. The coatings produced at 50°C exhibit a wider range of fluorescence, suggestive of lower surface uniformity; however, the majority of spots on these surfaces also approach the detection limit of the system, and also therefore reduced protein adsorption by approximately two orders of magnitude. One of the two 50°C 20-minute coatings adsorbed substantially

more protein than any other coated surface (although less than the uncoated UHMWPE) and may have been poorly coated, or contaminated.

Overall, the fluorescence results show that all of the PEGylated surfaces adsorb significantly less protein than uncoated UHMWPE, confirming that the plasma-polymerized tetraglyme coatings do resist protein adsorption. As expected from the XPS and contact angle results, plasma deposition time does not affect protein adsorption; however, plasma deposition temperature may have an effect. The coatings produced at 40°C appear to be either slightly more protein resistant, or slightly more uniform, than the coatings produced at 50°C, despite their somewhat lower ether content and higher hydrophobicity.

It is also interesting to note that both sets of samples were aged prior to the protein deposition experiments: 13 months for the 40°C coatings, and 4 months for the 50°C coatings. Despite aging, both sets of samples adsorb so little protein that it is nearly undetectable by this method.

Conclusions

The ATR-FTIR and XPS results confirm that all of the plasma-deposited coatings have chemical structures similar to poly(ethylene glycol), although the coatings generated at 50°C are slightly more PEG-like than those produced at 40°C. The increased ether content of the 50°C coatings depends solely on plasma deposition temperature, rather than time, and is also independent of coating thickness. Contact angle goniometry confirms that the PEGylated surfaces are significantly more hydrophilic than untreated UHMWPE. Furthermore, the increase in ether content of the 50°C surfaces observed by

XPS correlates to a small decrease in contact angle with respect to the 40°C surfaces, confirming that the more PEG-like surfaces are also more hydrophilic, as expected. The differences in ether content and contact angle between the uncoated UHMWPE, 40°C, and 50°C surfaces are statistically significant ($p < 0.05$).

All of the PEGylated surfaces resist protein deposition, adsorbing roughly two orders of magnitude less protein than uncoated UHMWPE. Plasma deposition time does not affect the degree of protein resistance, but coatings produced at 50°C may adsorb slightly more protein than those produced at 40°C. The coatings remain protein resistant for at least 13 months, suggesting that they should have an acceptable shelf life.

References

1. Roberts, M.J., M.D. Bentley, and J.M. Harris, *Chemistry for peptide and protein PEGylation.* Advanced Drug Delivery Reviews, 2002. **54**(4): p. 459-476.
2. Caliceti, P. and F.M. Veronese, *Pharmacokinetic and biodistribution properties of poly(ethylene glycol)-protein conjugates.* Advanced Drug Delivery Reviews, 2003. **55**(10): p. 1261-1277.
3. Allen, T.M., *The Use of Glycolipids and Hydrophilic Polymers in Avoiding Rapid Uptake of Liposomes by the Mononuclear Phagocyte System.* Advanced Drug Delivery Reviews, 1994. **13**(3): p. 285-309.
4. Gref, R., et al., *'Stealth' corona-core nanoparticles surface modified by polyethylene glycol (PEG): influences of the corona (PEG chain length and*

surface density) and of the core composition on phagocytic uptake and plasma protein adsorption. Colloids Surf B Biointerfaces, 2000. **18**(3-4): p. 301-313.

5. Bearinger, J.P., D.G. Castner, and K.E. Healy, *Biomolecular modification of p(AAm-co-EG/AA) IPNs supports osteoblast adhesion and phenotypic expression.* Journal of Biomaterials Science-Polymer Edition, 1998. **9**(7): p. 629-652.
6. Desai, T.A., *Micro- and nanoscale structures for tissue engineering constructs.* Medical Engineering & Physics, 2000. **22**(9): p. 595-606.
7. Jeon, S.I., et al., *Protein Surface Interactions in the Presence of Polyethylene Oxide .1. Simplified Theory.* Journal of Colloid and Interface Science, 1991. **142**(1): p. 149-158.
8. Jeon, S.I. and J.D. Andrade, *Protein Surface Interactions in the Presence of Polyethylene Oxide .2. Effect of Protein Size.* Journal of Colloid and Interface Science, 1991. **142**(1): p. 159-166.
9. Prime, K.L. and G.M. Whitesides, *Self-Assembled Organic Monolayers - Model Systems for Studying Adsorption of Proteins at Surfaces.* Science, 1991. **252**(5009): p. 1164-1167.
10. Mrksich, M., G.B. Sigal, and G.M. Whitesides, *Surface-Plasmon Resonance Permits in-Situ Measurement of Protein Adsorption on Self-Assembled Monolayers of Alkanethiolates on Gold.* Langmuir, 1995. **11**(11): p. 4383-4385.
11. Ostuni, E., et al., *A survey of structure-property relationships of surfaces that resist the adsorption of protein.* Langmuir, 2001. **17**(18): p. 5605-5620.

12. Wang, R.L.C., H.J. Kreuzer, and M. Grunze, *The interaction of oligo(ethylene oxide) with water: a quantum mechanical study.* Physical Chemistry Chemical Physics, 2000. **2**(16): p. 3613-3622.

13. Pertsin, A.J. and M. Grunze, *Computer simulation of water near the surface of oligo(ethylene glycol)-terminated alkanethiol self-assembled monolayers.* Langmuir, 2000. **16**(23): p. 8829-8841.

14. Harder, P., et al., *Molecular conformation in oligo(ethylene glycol)-terminated self-assembled monolayers on gold and silver surfaces determines their ability to resist protein adsorption.* Journal of Physical Chemistry B, 1998. **102**(2): p. 426-436.

15. Zolk, M., et al., *Solvation of oligo(ethylene glycol)-terminated self-assembled monolayers studied by vibrational sum frequency spectroscopy.* Langmuir, 2000. **16**(14): p. 5849-5852.

16. Lee, S., et al., *Boundary lubrication of oxide surfaces by Poly(L-lysine)-g-poly(ethylene glycol) (PLL-g-PEG) in aqueous media.* Tribology Letters, 2003. **15**(3): p. 231-239.

17. Lee, S., et al., *Influence of molecular architecture on the adsorption of poly(ethylene oxide)-poly(propylene oxide)-poly(ethylene oxide) on PDMS surfaces and implications for aqueous lubrication.* Macromolecules, 2004. **37**(22): p. 8349-8356.

18. Lopez, G.P., et al., *Glow-Discharge Plasma Deposition Of Tetraethylene Glycol Dimethyl Ether For Fouling-Resistant Biomaterial Surfaces.* Journal Of Biomedical Materials Research, 1992. **26**(4): p. 415-439.

19. Lopez, G.P. and B.D. Ratner, *Molecular Adsorption and the Chemistry of Plasma-Deposited Thin Organic Films: Deposition of Oligomers of Ethylene Glycol.* Plasmas and Polymers, 1996. **1**(2).

20. Cao, L., B.D. Ratner, and T.A. Horbett, *Plasma deposition of tetraglyme inside small diameter tubing: Optimization and characterization.* Journal of Biomedical Materials Research Part A, 2007. **81A**(1): p. 12-23.

21. Johnston, E.E., J.D. Bryers, and B.D. Ratner, *Plasma deposition and surface characterization of oligoglyme, dioxane, and crown ether nonfouling films.* Langmuir, 2005. **21**(3): p. 870-881.

22. Shen, M.C., et al., *Multivariate surface analysis of plasma-deposited tetraglyme for reduction of protein adsorption and monocyte adhesion.* Langmuir, 2003. **19**(5): p. 1692-1699.

23. Cao, L., et al., *Glow discharge plasma treatment of polyethylene tubing with tetraglyme results in ultralow fibrinogen adsorption and greatly reduced platelet adhesion.* Journal of Biomedical Materials Research Part A, 2006. **79A**(4): p. 788-803.

24. Cao, L., et al., *Plasma-deposited tetraglyme surfaces greatly reduce total blood protein adsorption, contact activation, platelet adhesion, platelet procoagulant activity, and in vitro thrombus deposition.* Journal of Biomedical Materials Research Part A, 2007. **81A**(4): p. 827-837.

25. Shen, M.C., et al., *PEO-like plasma polymerized tetraglyme surface interactions with leukocytes and proteins: in vitro and in vivo studies.* Journal of Biomaterials Science-Polymer Edition, 2002. **13**(4): p. 367-390.

26. Heuberger, M.P., et al., *Protein-mediated boundary lubrication in arthroplasty.* Biomaterials, 2005. **26**(10): p. 1165-1173.

Chapter 5

Coating Thickness Measurement

Introduction

Surface modification is a common approach to achieving a desired surface functionality while retaining the mechanical properties of the bulk material. Chemical characterization of the system is necessary to ensure that the coating has the expected chemical structure. Measuring the thickness of the coating may also be extremely important, as it often influences performance. In medical devices, it can affect parameters such as drug delivery rates [1]. In tissue engineering, it alters cellular responses to the materials [2]. For polymer coatings, film thickness can alter basic material properties including the glass transition temperature [3] and crystallinity [4], as well as the phase separation behavior of polymer blends [5].

PEG-like coating thickness is one of the most important variables in this study. Coating thickness has been shown to affect protein adsorption on self-assembled monolayers of poly(ethylene glycol) [6] and PEGylated nanoparticles [7], along with the rate of phagocytosis of the PEGylated nanoparticles [7]. In addition, coating thickness is

a critical factor in the wear behavior of modified surfaces, affecting plowing and asperity penetration [8] as well as load distribution in the coating and substrate [9].

While measuring coating thickness is important, it is often also challenging, and may involve substrates or environments different from those used for the actual system under investigation. Figure 1 illustrates the environment and sample requirements for a number of common techniques. A few methods, such as x-ray photoelectron spectroscopy (XPS) [10], Auger, and SIMS [11] sputtering, are relative and require calibration of the sputtering time [12]; however, the majority provide absolute thickness information. In terms of approach, the absolute techniques fall into three major categories: cross-sectioning followed by imaging; profile measurement of a step edge; and edge-free methods, such as ellipsometry.

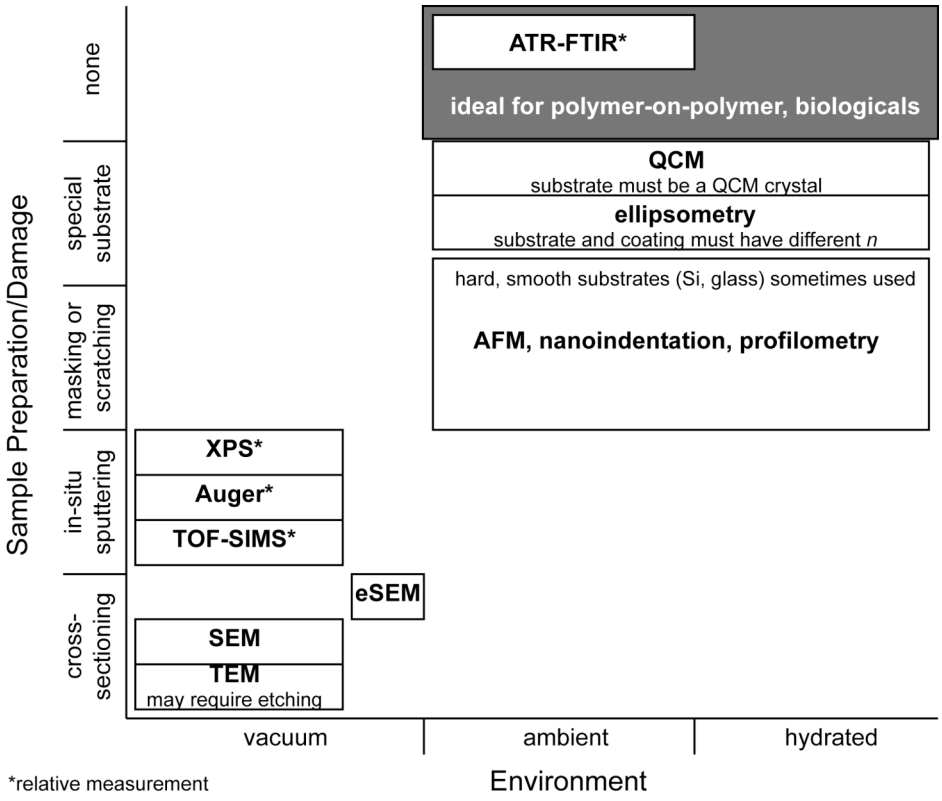

Figure 1: An overview of common coating thickness measurement methods and the sample preparation methods and environmental conditions they usually require. Asterisks denote methods that provide relative, rather than absolute, thickness values.

Predominant methods involving cross-sectioning include scanning and transmission electron microscopy (SEM and TEM). Although both can provide excellent images and highly accurate results independent of surface roughness, both yield a thickness determined in vacuum. Environmental SEM allows for sample hydration, but the chamber pressure is still less than 0.05 atm. SEM accommodates a wide range of samples fairly easily, but TEM involves substantial sample preparation: sample thickness cannot exceed 1 μm (200 nm for mostly-carbon samples such as polymers), and amorphous materials require staining to generate contrast [13, 14].

Step edge techniques include masking or scratching to generate the step, followed by atomic force microscopy (AFM), nanoindentation, or profilometry to measure the height of the resulting step. These methods can provide ambient or hydrated thicknesses, as well as information about surface roughness, but generating and locating the step edge is often challenging. To produce a well-defined step edge by masking, the mask must be highly conformal, particularly if the substrate is rough, and removal must not tear the coating. To produce an accurate step by scratching, the scratch cannot penetrate the substrate, a significant concern for soft substrates. In addition, since the step edge must be distinguishable from the surface features, these methods may not work well on coatings whose thickness is on the same order of magnitude as their surface roughness. Both the cross-sectioning and step edge techniques are also typically destructive and time-consuming.

Edge-free techniques, such as angle-resolved XPS, ellipsometry, and quartz crystal microbalance (QCM) measurement, have their own unique advantages and disadvantages. Angle-resolved XPS provides both coatings thickness and detailed chemical composition information, but works only on ultrathin coatings (less than 10-20 nm thick) [10, 15]. Ellipsometry can be performed under ambient or hydrated conditions, but requires that the complex index of refraction of the coating and substrate both be known and different [16]. Similarly, QCM can also be performed in air or hydrated; however, it requires knowledge or assumption of the coating density, or coupling with other measurement systems, such as ellipsometry, in order to calculate coating thickness [17]. In addition, QCM must be performed on a special substrate, rather than on the

actual samples. Like step edge techniques, ellipsometry and QCM also may not work well on coatings with significant surface roughness [16-18].

The PEGylated UHMWPE samples used in this study present several challenges. The coatings are too thick to use angle-resolved XPS. The RMS roughness of even microtomed UHMWPE surfaces is 20-35 nm, much larger than ellipsometry, QCM, or step-edge techniques like masking can easily accommodate. Bulk PEG and UHMWPE have the same refractive index (1.51) [19], rendering them difficult if not impossible to distinguish by ellipsometry. Attempts to generate intact cross-sections by razor cutting, microtoming, and focused ion beam milling all failed, eliminating the possibility of using SEM or TEM.

To overcome these challenges, a new thickness measurement method was developed based on attenuated total reflection Fourier transform infrared spectroscopy (ATR-FTIR). ATR-FTIR is a well-established, non-destructive method for determining the chemical composition of materials based on their chemical bonding. In addition, it is much faster than more common thickness measurement techniques, requiring no sample preparation, pumpdown, or sputtering.

The theory behind ATR-FTIR appears in detail in Chapter 2. Briefly, ATR-FTIR is a chemical characterization technique that achieves surface specificity by passing the infrared beam through a crystal to generate an evanescent wave at the surface, which is in direct contact with the surface of the sample. The penetration depth d of the evanescent wave into the sample depends on the angle θ of the beam through the crystal; the refractive indices n_1 and n_2 of the crystal and sample, respectively; and the wavelength λ of the infrared light [20]:

$$d = \frac{\lambda}{2\pi\sqrt{n_1^2 \sin^2\theta - n_2^2}} \qquad [1].$$

The sample volume depends on the penetration depth and the surface area A_c of the sample in contact with the crystal:

$$V = dA_c \qquad [2].$$

Infrared-active chemical bond motions (stretching, bending, wagging) generate peaks at known wavelengths. The area under each peak in the absorbance spectrum is directly proportional to the number of bonds corresponding to that peak that are present in the sampling volume. Although the absolute number of each type of bond cannot be calculated easily, the peak areas from different spectra can be compared to determine the relative quantities of each bond present. For samples that contain a chemical bond unique to the coating, this enables ATR-FTIR to measure relative coating thicknesses. However, to determine absolute coating thicknesses, the ATR-FTIR signal must be calibrated by a second measurement technique.

Yang et al proposed a method to ascertain this relation using variable-angle ATR-FTIR [21], but it applies only to systems with unique chemical bonds present in both the substrate and the coating, and it was verified only for non-hydrated coatings 10-110 nm thick. Zhang et al combined ATR-FTIR and AFM to estimate the thickness of poly(ethylene terephthalate) films on glass substrates, a soft-on-hard system, but did not provide enough experimental detail to create a reproducible methodology [3].

In this study, we also use AFM to calibrate ATR-FTIR measurements, but extend the technique to more difficult classes of coatings: soft-on-soft material combinations, such as polymer coatings on polymer substrates, and hydrated systems. As Figure 1 shows, techniques to measure the thickness of these materials are currently lacking.

Hydrated methods usually require non-polymer substrates with specific properties: good scratch resistance, a well-defined refractive index, nanometer-scale surface roughness, and oscillation resonance. Polymers rarely meet these requirements, but are often the intended substrates for the actual coating applications.

AFM topography imaging can be used to measure step edges of coatings generated in two ways: externally, by masking [22] or manually scratching [5, 11, 23, 24] the coating; or internally, by scratching the coating with the AFM tip in contact mode [25]. However, scratching is usually performed to remove soft coatings, such as polymers or proteins, from hard surfaces, such as silicon or glass [3, 5, 11, 18, 23, 24], rather than soft surfaces that can themselves also be scratched.

In contrast, this work utilized contact-mode AFM scratching to create defects in soft polymer coatings on soft polymer substrates. The absolute coating thicknesses found by AFM were then correlated to ether peak area from ATR-FTIR in order to calibrate the infrared signal so that ATR-FTIR alone could be used to rapidly and non-destructively calculate the PEG-like coating thickness of subsequent samples.

Materials and Methods

For ATR-FTIR, substrates approximately 5 mm x 20 mm were cut from UHMWPE sheets 250 μm thick (McMaster-Carr). For AFM, UHMWPE (McMaster-Carr) blocks with dimensions 3 mm x 3 mm x 5 mm were cut from a 3 mm thick bar, and the 3 mm x 5 mm faces were microtomed with a Reichert Ultracut E instrument to minimize surface roughness. All substrates were cleaned by successive sonication in 1% Aquet solution (Bel-Art Products), deionized water 3x, acetone, and isopropanol (Sigma-

Aldrich). The substrates were coated with plasma-polymerized tetraglyme (Sigma-Aldrich) using a Plasma Science PS0500 instrument with a 13.56 MHz, 550 W generator. High-power argon treatment (400 W, 250 sccm, 3 minutes) was used to clean and activate the UHMWPE surface to promote covalent bonding of the coating. Tetraglyme was then plasma polymerized onto the surface at 50 W, 30 sccm argon, with 6 mL/hr tetraglyme flow through a 130°C heating tube, for 2-30 minutes to generate a range of coating thicknesses. The chamber was flushed with argon (no power, 250 sccm, 1 minute) three times before the samples were removed. The walls of the chamber were heated to 40-50°C during the entire plasma process, and the chamber was pumped down to a base pressure of 30 mTorr before each step. All samples used to generate the thickness calibration curve were coated on the same day; samples used to test the generality of the calibration were coated on different days.

ATR-FTIR was used to determine both the chemical composition and the relative thicknesses of the coatings. Spectra were taken using a Nicolet Avatar 360 with an Omni-Sampler ATR accessory (Ge crystal, single-bounce beam path, 45° incident angle, 32 scans). For each plasma deposition batch, spectra were collected on three samples at two spots, and the results of the six spectra were averaged to determine metrics for the batch as a whole, including the samples scratched by AFM.

An advanced ATR correction was applied to all spectra and the region from 1800 cm^{-1} to 900 cm^{-1} was peak fit using Omnic 7.3 software. For coated samples, this region usually contained ten peaks: one carbonyl (~1730 cm^{-1}); another carbonyl or water (1620-1650 cm^{-1}, always very small); one hydrocarbon doublet (modeled as a single peak at ~1465 cm^{-1}); and seven ether peaks from 940-1370 cm^{-1}. In contrast, uncoated

UHMWPE, which consists of linear -(CH_2)- hydrocarbon chains, exhibits only the hydrocarbon doublet. Since tetraglyme contains both ether and hydrocarbon bonds (see Figure 2), the most prominent ether peak, located at approximately 1115 cm^{-1}, was chosen as an indicator of coating thickness.

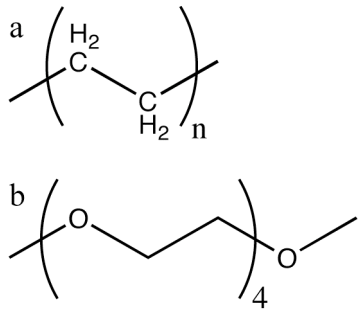

Figure 2: The chemical structures of a) UHMWPE and b) tetraglyme.

Atomic force microscopy was performed with an Asylum Research MFP-3D instrument using silicon cantilevers (Nanosensors FM-50 tips, spring constant ~2 nN/nm). All experiments were performed in phosphate-buffered saline (PBS, Gibco, pH 7.3). To wear away the coatings, a region of the surface (either 2 μm x 2 μm or 1 μm x 4 μm) was repeatedly scratched in contact mode with normal forces of 0.7-2 μN. A larger region of the surface (6 μm x 6 μm or 2 μm x 8 μm) was imaged in tapping mode before scratching began, and again after every 1-4 scratches to evaluate the extent of damage to the coating. This ensured that, even with some instrument drift, the images showed both the wear box and a substantial unworn area. To facilitate removal of the thicker coatings, after the initial image was taken, a rectangle slightly smaller than the intended wear box was pre-scratched 5-10 times in contact mode at 1-2 μN normal force using the

MicroAngelo® lithography feature of the MFP-3D software. The whole region was then re-imaged, and then scratching of the wear box began. Figure 3 shows the progression of a typical scratching experiment, including image analysis.

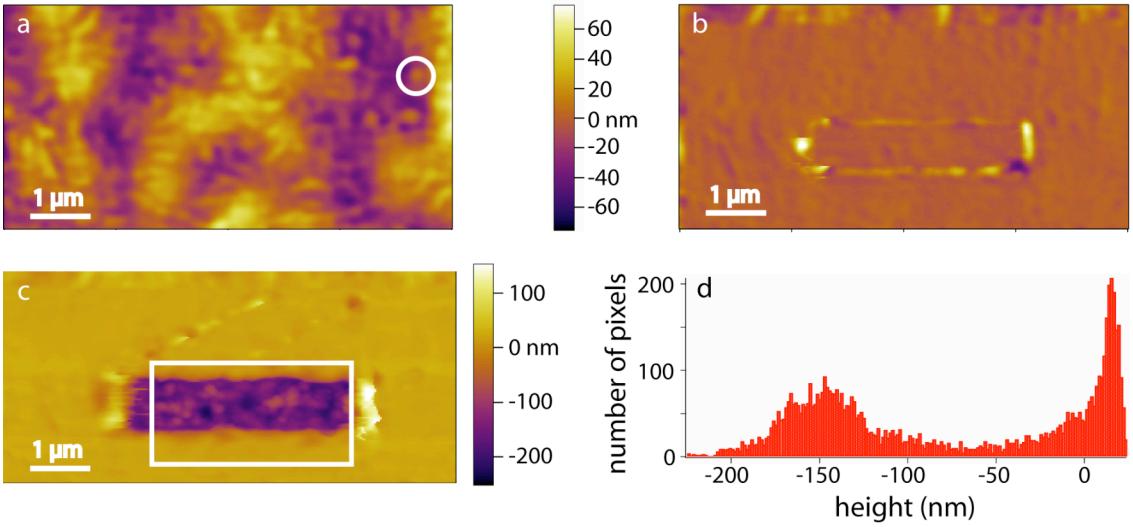

Figure 3: The sequence of an AFM scratching experiment. a) The initial image of the surface before the lithographic pre-scratch. This image was used as the reference for subtraction of all subsequent images; the peak used to align the images is circled in white. b) The subtracted image of the surface after the lithographic pre-scratch. The outline of the pre-scratch box is clearly visible. c) The subtracted image of the surface after lithographic pre-scratching and two scratches of the full wear box. The region outside the white box was masked off to produce the histogram of peak heights shown in part d. Note that the scale is identical for the initial reference image (a) and the image of the lithographic pre-scratch (b), but different for the masked, worn image (c).

Image analysis was performed using MPD-3D software and Igor Pro 6.02A. The image taken before the first contact mode scratch served as a reference for every subsequent image in a series of scratches. Since the substrate was relatively rough – 20-35 nm RMS roughness after microtoming; plasma treatment did not alter the roughness – the reference image was subtracted from each subsequent image to produce images that highlighted wear-induced changes in the topography. To compensate for any drift over

the course of the experiment, a characteristic feature in the unworn region of all images in a series was chosen as a reference point, and the highest pixel of that feature in each worn image was aligned with the highest pixel of that same feature in the initial image before subtraction.

The subtracted images feature a frame of unworn material surrounding a wear box, often with pile-up of worn material around the edges of the box. This produces a topographical distribution that contains three regions: a small peak from the pile-up; a very large peak from the unworn region (the intact coating surface); and a small peak from the worn area (the newly-exposed substrate). The peak from the unworn region is much larger than the other peaks because the unworn area of the image is 7-8 times larger than the worn region. To produce a histogram with both of these peaks clearly visible and similarly sized, much of the unworn region was masked off, as was the pile-up. The thickness of the coating was then calculated as the difference between the centers of the peak from the intact coating surface and the exposed substrate in the resulting histogram.

One crucial aspect of this method is the ability to determine when the substrate surface has been exposed. In this study, the distinguishing characteristic between the two materials was their wear behavior. The PEG-like coating tears suddenly, resulting in removal of micron-sized pieces of material, while the UHMWPE wears gradually and, after repeated scratches, develops a sinusoidal profile of plastically deformed peaks and troughs perpendicular to the direction of scratching. In addition, the tearing of the PEG coating is visible on images taken during the contact-mode scratching; when the coating tears, the tip slips and disrupts the image.

Based on these observations, tapping-mode height images used to calculate the coating thickness for ATR-FTIR calibration curve were taken after the coatings tore, but before the development of the sinusoidal UHMWPE wear profile. For a given series of scratches at a single spot, one representative image was used to determine the thickness of the coating at that point on the sample. Series of scratches were performed at different points on the surface of each sample, which was approximately 3 mm x 5 mm in size, to attain a representative set of thickness measurements for the coating as a whole.

Results

Detailed chemical characterization of the PEGylated UHMWPE surfaces is presented in Chapter 3. As expected, the ATR-FTIR spectra exhibit only carbonyl (C=O), hydrocarbon (CH_x), and ether (C-O) peaks. The ether peaks, particularly the most prominent peak at 1115 cm^{-1}, increase in both height and area with increasing PEG-like coating thickness, as shown in Figure 4.

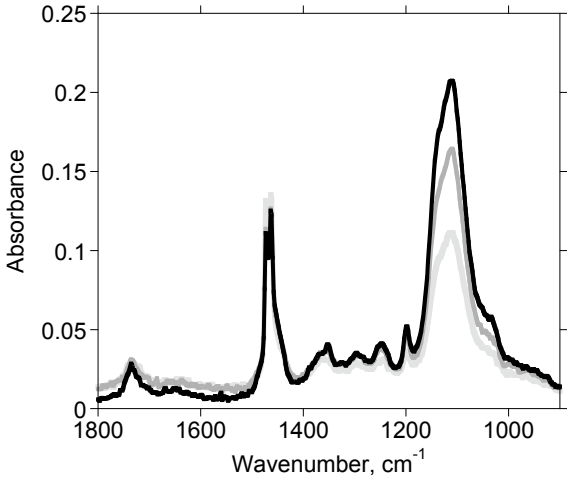

Figure 4: An overlay of the ATR-FTIR absorbance spectra of coatings with three different thicknesses: 64 nm in light gray, 108 nm in darker gray, and 195 nm in black.

The absolute thickness of the coatings was determined by serial AFM scratching and imaging. Figure 3 shows a representative set of AFM results: the unsubtracted initial image, with an RMS roughness of 21 nm; the subtracted image of the lithographic pre-scratch before the coating was worn away; the subtracted, masked image of the area after two scratches; and the histogram constructed from the masked image. In the histogram, the peak just above zero comes from the unworn coating surface, while the peak centered near -150 nm comes from the region where the coating has been removed.

When a lithographic pre-scratch was employed to facilitate removal of thicker coatings, the thickness of the removed coating did not appear to depend on the normal load applied during the pre-scratch. The coatings did not wear at all when the pre-scratch loads were too low. At higher lithography loads, the coatings tore away quickly (after 1-3 contact-mode scratches), and subsequent scratches on the exposed substrate produced the sinusoidal profile characteristic of UHMWPE wear.

The calibration curve constructed from the ATR-FTIR ether peak areas and the AFM coating thicknesses appears in Figure 5. As expected, the area under the ether peak is directly proportional to the coating thickness. Theoretically, the y-intercept should be zero, such that a surface with no ether signal has no coating thickness. In fact, when unconstrained, the y-intercept is only -3.3 nm, within the error of the measurement, and the R^2 value is 0.97 for both the constrained and unconstrained calibration curves. Therefore, in accordance with theory, the constrained calibration was found to be

$$t = 11.1a \qquad [3],$$

where t is the coating thickness in nanometers and a is the area under the ether peak.

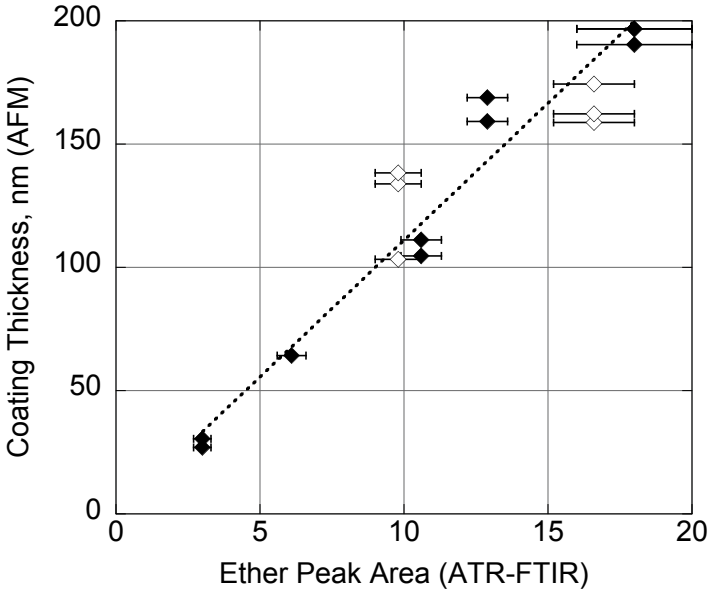

Figure 5: The ATR-FTIR calibration curve generated from the AFM scratching experiments. Filled diamonds represent calibration data, which were fitted to the dotted line; open diamonds indicate validation results. The ether peak areas are shown as the mean and standard deviation of six spectra, while the coating thickness measurements are displayed individually and therefore do not have error bars.

To validate the calibration method, two additional substrates were coated on different days at different deposition times and evaluated by ATR-FTIR and AFM. Using the ether peak areas from their ATR-FTIR spectra and the calibration curve given by Equation 3, the sample thicknesses were calculated and compared to the actual values measured by AFM. The results appear in Table 1.

Table 1: Comparison of calculated and measured coating thicknesses

Sample	Ether peak area	Calculated thickness, nm (ATR-FTIR, Eq. 3)	Measured thickness, nm (AFM)	Mean difference, nm
1a	16.6	185	159	19
1b			174	
1c			162	
2a	9.8	109	134	16
2b			103	
2c			138	

Discussion

This chapter describes the development of ATR-FTIR as a method for measuring the thickness of the PEG-like coatings. AFM was used to calibrate the ATR-FTIR measurements. Although construction of the AFM calibration curve was time-consuming and damaged the samples, it was only performed once. Afterward, coating thicknesses were determined solely by ATR-FTIR measurements, which are fast (spectra take about a minute, as opposed to an hour or more for AFM scratching or any vacuum technique) and non-destructive.

The methods described here should be useful for several types of coatings – polymer-on-polymer coatings and hydrated coatings – whose thickness is difficult to measure by more common techniques. However, when proposing a new method, it is important to consider both the advantages and limitations. These exist for both AFM and ATR-FTIR.

AFM can be used to examine surfaces with significant (tens of nanometers) surface roughness, and it can be performed on hydrated coatings. The image-scratch-image sequence provides valuable information about the surface roughness and coating wear behavior in addition to the absolute thickness measurement. The major constraints

imposed by the AFM scratching technique are that it must be possible both to remove the coatings from their substrates by contact mode AFM, and to know when the substrate has been exposed. The former is most likely to be true for coatings that are softer than the substrates, or poorly bonded. The latter may be accomplished in several ways. Several AFM methods, most notably phase contrast [26] and lateral force (friction) microscopy [24], have been developed to distinguish between different materials, particularly polymer blends. Both of these approaches are well-established and may work well for a number of systems, including polymer coatings on polymer substrates. However, neither of these methods proved effective for distinguishing between the UHMWPE and the PEG-like coating investigated in this study. Consequently, the wear behavior of the two materials became the distinguishing factor, as described in the Methods section.

ATR-FTIR is rapid and non-destructive, and it provides valuable information about the chemical structure of the coating in addition to the relative thickness measurement. However, relative thickness measurements are only possible for material combinations such that the coating possesses a unique infrared-active chemical bond not present in the substrate. In addition, the technique relies on three key assumptions: 1) that the density and chemical composition of the coatings does not vary substantially within a single sample or between different samples; 2) that the ATR-FTIR penetration depth at the wavelength of the peak unique to the coating is greater than the thickness of the coating; and 3) that the ATR-FTIR penetration depth is constant for every sample.

The first assumption ensures constant bond density, both between and within samples, which is necessary to produce a linear calibration curve. Violating this assumption may lead to a non-linear calibration curve, which should still be usable as

long as each ATR-FTIR peak area corresponds to a unique coating thickness, and vice versa.

The second assumption ensures that the ATR-FTIR signal reflects the chemical bonds present in the full coating thickness. If this assumption is violated, such that the infrared beam passes through only part of the coating, then the peak area will reach a maximum at which it becomes independent of the coating thickness. In that case, using an ATR crystal with an index of refraction closer to that of the sample may help to attain a greater sampling depth.

The third assumption ensures that the peak areas can be compared between spectra. If this assumption is violated (and not corrected for), the method will not work. Direct peak area comparisons are valid only if the ATR-FTIR sample volume is constant for every specimen, which is easy to achieve if the specimens have the same dimensions and are held in close enough contact with the ATR crystal such that the contact pressure is relatively constant. However, if the contact area must vary substantially, the resulting changes in sample depth from specimen to specimen can be corrected for by using the ratio of two peak areas as the FTIR metric. In this case, one peak must be unique to the coating, and the second must be unique to the substrate.

In the PEGylated UHMWPE model system presented here, the linearity of the calibration curve indicates that the first assumption holds. The penetration depth at 1115 cm^{-1} was calculated to be nearly 600 nm (see Chapter 2), whereas the coating thicknesses did not exceed 200 nm, so the second assumption holds. Due to the compliance and thinness (250 μm) of the substrates used for the ATR-FTIR analysis, the only region of the sample to maintain contact with the ATR crystal was the region directly beneath the

holder exerting pressure on the sample. This ensured a relatively constant contact area. In addition, changing the pressure exerted on the sample while maintaining good contact with the crystal did not substantially alter the resulting spectra. Therefore, the third assumption holds as well.

The validity of the technique was tested by calculating the expected thickness of two additional coatings from their ATR-FTIR ether peak areas using Equation 3 and comparing the calculated value to the actual thickness measured by AFM. The results differed by 10-15% of the actual thickness, more than expected from the calibration curve fit ($R^2 = 0.97$). However, the difference likely arose from changes in the density or degree of crosslinking of the PEG-like coatings due to variation in the plasma deposition process, a characteristic of the model system rather than the measurement technique.

Conclusions

This study successfully measured coating thicknesses ranging from 30-200 nm. The thickness of the validation samples measured by AFM was within 20 nm (10-15%) of the thickness calculated by ATR-FTIR. The limits of the thicknesses measured were constrained by plasma deposition of the PEG-like coating, not by AFM scratching or the ATR-FTIR sampling depth. At the lower limit, the method successfully resolved coating thicknesses comparable to the RMS roughness of the substrate (20-35 nm). At the upper limit, the coatings could still be removed with just a few scratches as long as the lithographic pre-scratch step was performed; therefore, this is probably not the actual upper limit of the technique for this model system. The true upper bound would be determined by either the ability to remove the coatings by AFM scratching (which will

differ for every coating material) or by the ATR-FTIR sampling depth at the wavelength of the peak unique to the coating.

Calibrating relative ATR-FTIR thickness measurements with AFM can provide rapid, non-destructive measurement of the thickness of a wide range of coatings on a wide range of substrates. This combination of methods is expected to be particularly useful for polymer-on-polymer and hydrated films.

References

1. Susut, C. and R.B. Timmons, *Plasma enhanced chemical vapor depositions to encapsulate crystals in thin polymeric films: a new approach to controlling drug release rates.* International Journal of Pharmaceutics, 2005. **288**(2): p. 253-261.
2. Jones, D.S., et al., *Examination of surface properties and in vitro biological performance of amorphous diamond-like carbon-coated polyurethane.* Journal of Biomedical Materials Research Part B-Applied Biomaterials, 2006. **78B**(2): p. 230-236.
3. Zhang, Y., et al., *Glass transition temperature determination of poly(ethylene terephthalate) thin films using reflection-absorption FTIR.* Macromolecules, 2004. **37**(7): p. 2532-2537.
4. Frank, C.W., et al., *Structure in thin and ultrathin spin-cast polymer films.* Science, 1996. **273**(5277): p. 912-915.

5. El-Mabrouk, K., M. Belaiche, and M. Bousmina, *Phase separation in PS/PVME thin and thick films.* Journal of Colloid and Interface Science, 2007. **306**(2): p. 354-367.

6. Prime, K.L. and G.M. Whitesides, *Adsorption of Proteins onto Surfaces Containing End-Attached Oligo(Ethylene Oxide) - a Model System Using Self-Assembled Monolayers.* Journal of the American Chemical Society, 1993. **115**(23): p. 10714-10721.

7. Gref, R., et al., *'Stealth' corona-core nanoparticles surface modified by polyethylene glycol (PEG): influences of the corona (PEG chain length and surface density) and of the core composition on phagocytic uptake and plasma protein adsorption.* Colloids Surf B Biointerfaces, 2000. **18**(3-4): p. 301-313.

8. Holmberg, K., H. Ronkainen, and A. Matthews, *Tribology of thin coatings.* Ceramics International, 2000. **26**(7): p. 787-795.

9. Johnson, K.L., *Contact Mechanics*. 1985, Cambridge, UK: Cambridge University Press.

10. Cumpson, P.J., *Angle-Resolved XPS and AES - Depth-Resolution Limits and a General Comparison of Properties of Depth-Profile Reconstruction Methods.* Journal of Electron Spectroscopy and Related Phenomena, 1995. **73**(1): p. 25-52.

11. Norrman, K., K.B. Haugshoj, and N.B. Larsen, *Lateral and vertical quantification of spin-coated polymer films on silicon by TOF-SIMS, XPS, and AFM.* Journal of Physical Chemistry B, 2002. **106**(51): p. 13114-13121.

12. Quadakkers, W.J. and H. Viefhaus, *Guidelines for Methods of Testing and Research in High Temperature Corrosion*, in *European Federation of Corrosion*

Publications, Number 14, H.J. Grabke and D.B. Meadowcroft, Editors. 1995, The Institute of Materials: London.

13. Egerton, R.F., *Physical Principles of Electron Microscopy*. 2005, New York: Springer.
14. Bogner, A., et al., *A history of scanning electron microscopy developments: Towards "wet-STEM" imaging.* Micron, 2007. **38**(4): p. 390-401.
15. Liu, H.A. and T.J. Webster, *Nanomedicine for implants: A review of studies and necessary experimental tools.* Biomaterials, 2007. **28**(2): p. 354-369.
16. Tompkins, H.G., *A User's Guide to Ellipsometry*. 1993, Mineola, NY: Dover Publications, Inc.
17. Marx, K.A., *Quartz crystal microbalance: A useful tool for studying thin polymer films and complex biomolecular systems at the solution-surface interface.* Biomacromolecules, 2003. **4**(5): p. 1099-1120.
18. Mykhaylyk, T.A., et al., *Comparative characterisation by atomic force microscopy and ellipsometry of soft and solid thin films.* Surface and Interface Analysis, 2007. **39**(7): p. 575-581.
19. Brandrup, J., et al., eds. *Polymer Handbook*. 4th ed. 1999, John Wiley & Sons, Inc.: New York.
20. Smith, B.C., *Fundamentals of Fourier Transform Infrared Spectroscopy*. 1996, New York: CRC Press.
21. Yang, P., et al., *Thickness measurement of nanoscale polymer layer on polymer substrates by attenuated total reflection infrared spectroscopy.* Analytical Chemistry, 2005. **77**(4): p. 1068-1074.

22. Girard-Lauriault, P.L., et al., *Atmospheric pressure deposition of micropatterned nitrogen-rich plasma-polymer films for tissue engineering.* Plasma Processes and Polymers, 2005. **2**(3): p. 263-270.

23. Benesch, J., A. Askendal, and P. Tengvall, *The determination of thickness and surface mass density of mesothick immunoprecipitate layers by null ellipsometry and protein (125)iodine labeling.* Journal of Colloid and Interface Science, 2002. **249**(1): p. 84-90.

24. Cyganik, P., et al., *AFM/LFM surface studies of a ternary polymer blend cast on substrates covered by a self-assembled monolayer.* Surface Science, 2002. **507**: p. 700-706.

25. Kaupp, G., *Atomic Force Microscopy, Scanning Nearfield Optical Microscopy and Nanoscratching*. NanoScience and Technology, ed. P. Avouris, et al. 2006, New York: Springer.

26. Raghavan, D., et al., *Mapping polymer heterogeneity using atomic force microscopy phase imaging and nanoscale indentation.* Macromolecules, 2000. **33**(7): p. 2573-2583.

Chapter 6

Coating Tribology

Introduction

Ultrahigh molecular weight polyethylene (UHMWPE) has been used as a bearing surface in joint replacements since it was introduced as the acetabular component of total hip replacements (THRs) by Sir John Charnley in 1962 [1]. Although UHMWPE has proven to be an excellent material for joint replacements due to its bulk biocompatibility and high wear resistance, UHMWPE components still produce millions or billions of wear particles per year in vivo [2]. The particles are primarily sub-micron in size [2], which means they can be phagocytosed readily by macrophages. Phagocytosis of UHMWPE particles initiates an immune response cascade that can lead to chronic inflammation, joint pain, periprosthetic bone loss, implant loosening, and the necessity for revision surgery. This process, known as aseptic loosening or wear-mediated osteolysis, is the primary cause of late-stage failure of total joint replacements, and it is known to result predominantly from UHMWPE particles, rather than bone cement, ceramic, or metal debris [3, 4].

Consequently, decreasing the wear rate of UHMWPE has been one of the main areas of total joint replacement research for many years. Modifications to the bulk material have included the addition of carbon fibers for reinforcement, which resulted instead in early failure of a number of tibial inserts of total knee replacements due to increased contact stresses and poor material consolidation [5, 6]; high pressure treatments to increase lamellar size, with mixed results [7]; and crosslinking to reduce lamellar orientation, which is known to be a precursor to wear particle formation [8]. Although crosslinking UHMWPE does reduce the wear rate, it also reduces the ultimate tensile properties [9] and fracture toughness of the bulk material [10]. As a result, some crosslinked UHMWPE acetabular cups have failed due to a combination of reduced material toughness and poor implant design choices, such as overly thin cups and the inclusion of stress concentrators [11, 12].

Surface modification of UHMWPE is an attractive alternative for wear reduction because it has the potential to improve the surface wear behavior while retaining the favorable bulk material properties such as toughness and fatigue resistance. A number of researchers have hardened the UHMWPE surface by ion bombardment/implantation, which generates surface crosslinking [13, 14] or diamond-like coatings (DLCs) [15, 16]. This can lead to a decrease in wear [13] and an increase in scratch resistance [15].

An alternative approach is to increase lubrication at the UHMWPE-counterbearing interface by applying soft hydrophilic polymer coatings to the UHMWPE surface. Three groups have tried this. Pavoor et al dip-coated UHMWPE with polyelectrolyte multilayers, which reduced the wear rate of the UHMWPE [17]. However, the decrease in wear resulted from formation of a lubricious transfer film on

the counterbearing, a mechanism unlikely to be effective in the body, where synovial fluid may wash lubricious PEM fragments away from the articulating interface.

Therefore, covalently-bonded lubricious coatings seem more promising. Zhang et al generated hyaluronan coatings on sintered UHMWPE microcomposites and found that they significantly reduced the wear volume compared to uncoated UHMWPE, but the sintering method using during the coating process produced inferior quality UHMWPE [18]. This suggests that direct surface treatments, such as photopolymerization or plasma treatment, are preferable. Moro et al photopolymerized 2-methacryloyloxyethyl phosphorylcholine (MPC), a monomer similar to phospholipids found in cell membranes, onto UHMWPE to form a covalently-bonded brush layer on the surface [19]. The MPC coating resists protein deposition [20]; it also reduces particle immunogenicity and decreases the wear rate of crosslinked UHMWPE [19].

The performance of the hyaluronan and MPC surfaces provides strong proof of concept for the use of covalently-bonded hydrogel coatings to increase lubricity and decrease wear of UHMWPE. This study investigates the efficacy of an alternative coating material, poly(ethylene glycol) (PEG). PEG is a flexible linear polymer made from CH_2CH_2O repeat units (see Figure 1) that is hydrophilic, lubricious, biocompatible, and resistant to protein deposition. It has been used for a variety of other biomedical applications, such as conjugation to drugs to reduce antigenicity and enzymatic degradation [21, 22], and to reduce phagocytosis of drug-releasing liposomes [23, 24].

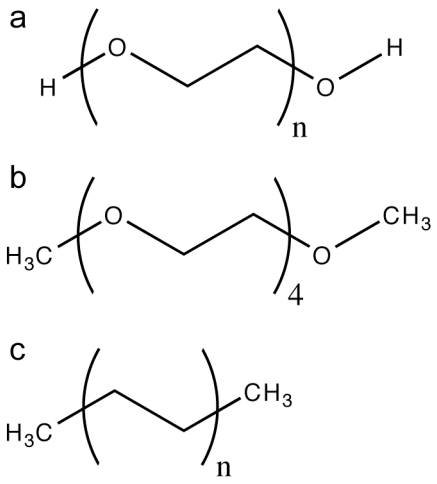

Figure 1: The chemical structures of a) poly(ethylene glycol), b) tetraglyme, and c) polyethylene.

Crosslinked PEG-like surfaces made from plasma-polymerized tetraglyme have similar chemistry to PEG, and are also hydrophilic and protein resistant. These coatings have been characterized chemically [25] and evaluated as anti-thrombogenic surfaces for blood-contacting applications [26]. Plasma deposition offers several significant advantages over solution-state grafting or adsorption [27]. It produces coatings that are conformal, continuous, and sterile. It also generates covalent bonds between the coatings and the substrates, even when the substrate is a material such as UHMWPE that lacks reactive side groups. Finally, plasma deposition produces coatings that are crosslinked, which is likely to increase the mechanical strength and wear resistance of the material relative to an uncrosslinked, end-grafted brush layer like MPC.

This study examines the chemical composition, hydrophilicity, protein deposition resistance, and wear behavior of plasma-polymerized tetraglyme coatings on UHMWPE. Characterization of the surfaces was performed using X-ray photo electron spectroscopy (XPS), attenuated total reflection Fourier transform infrared spectroscopy (ATR-FTIR),

contact angle goniometry, protein deposition, atomic force microscopy (AFM) and wear testing. The wear behavior was observed on three different length scales – millimeter, tens to hundreds of microns, and less than ten microns – to elucidate the tribological mechanisms occurring at each level. This understanding should enable intelligent design decisions regarding future iterations of PEG-like coatings, as well as other hydrogels used for similar purposes, to tailor their wear behavior.

Materials and Methods

Materials

UHMWPE substrates were cut from 250 μm thick sheets (XPS, ATR-FTIR, contact angle, protein deposition) or rod stock (AFM, wear pins, ATR-FTIR mapping), both from McMaster-Carr. Using a Reichert Ultracut E with a fresh glass blade, smooth surfaces 3 mm x 5mm or 2 mm in diameter were microtomed on the AFM samples and wear pins, respectively. All substrates were then cleaned by successive sonication in 1% Aquet solution (Bel-Art Products), deionized water 3x, acetone, and isopropanol (Sigma-Aldrich).

Plasma deposition

Clean UHMWPE substrates were coated with tetraglyme (Sigma-Aldrich) using a Plasma Science PS0500 parallel-plate reactor with a 13.56 MHz, 550 watt RF generator. High-power argon treatment (400 W, 250 sccm, 3 minutes) was used to activate the UHMWPE surface to promote covalent bonding of the coating. Tetraglyme was then plasma polymerized onto the surface at 50 W, 30 sccm argon, with 6 mL/hr tetraglyme

flow through a 130°C heating tube, for 20-40 minutes to generate a range of coating thicknesses. During the entire plasma process, the walls of the chamber were heated to 50°C.

X-ray photoelectron spectroscopy (XPS)

XPS was performed on a Surface Science Instruments S-probe spectrometer with a monochromatized Al source at a 55° take-off angle (sampling depth 5-10 nm; spot size ~800 μm). For each plasma deposition batch, survey and high-resolution C1s spectra were collected at two spots on two samples, and the results were averaged to determine metrics for the batch as a whole. High-resolution C 1s spectra were peak fit with the Service Physics ESCAVB Graphics Viewer to resolve the hydrocarbon, ether, and carbonyl peaks.

Contact angle goniometry

The relative hydrophilicity of the surfaces was measured using a custom-made contact angle goniometer with a variable-magnification InfiniVar video microscope (Infinity Photo-Optical Co.), a 1.45 megapixel Sony XCD-SX910 camera, and LabView 7.1 software. 5 μL of deionized water was pipetted onto the surface, the drop was imaged in LabView, and the static contact angle was calculated by the tangent chord theorem. Contact angle goniometry was performed at two spots on two samples per plasma deposition batch.

Attenuated total reflection-Fourier transform infrared spectroscopy (ATR-FTIR)

ATR-FTIR spectra were collected using a Nicolet Avatar 360 with an Omni-Sampler ATR accessory (Ge crystal, single-bounce beam path, 45° incident angle, 32 scans, 4 cm^{-1} resolution). An advanced ATR correction was applied to all spectra and the region from 1800 cm^{-1} to 900 cm^{-1} was peak fit using Omnic 7.3 software. The area under the most prominent ether peak at ~1115 cm^{-1} was used to compare the relative thickness of different coatings.

ATR-FTIR mapping

ATR-FTIR maps were collected with a ThermoNicolet Nexus 870 FT-IR ESP with a Nicolet Continuum XL FT-IR Imaging Microscope (15x objective) and a Ge ATR crystal (single-bounce beam path, 32 scans per spot, 25 μm spot size, 37.5 μm step size, 4 cm^{-1} resolution). All spectra were truncated to 1800-900 cm^{-1}, baseline corrected, and an advanced ATR-FTIR correction was applied, again using Omnic 7.3. Profiles of the ether/hydrocarbon ratio (the ratio of the area under the ether peak normalized by the area under the carbonyl peak) were constructed to evaluate the coating thickness across the mapped region.

Protein adsorption

Uncoated and PEGylated UHMWPE substrates were soaked in 5 μg/mL bovine serum albumin conjugated to AlexaFluor 488 (BSA-AF, Invitrogen) in phosphate-buffered saline (PBS, Gibco, pH 7.4) for 30 minutes, then rinsed three times with PBS; albumin was chosen because it is the most common protein in synovial fluid [28]. To

quantify protein adsorption, the surfaces were visualized with a Zeiss AxioImager M1 fluorescence microscope with a Zeiss Plan-Neofluar 20x air objective, NA=0.50, using a 450-490 nm excitation filter and a 500-550 nm emission filter (both band pass). Five areas on each sample imaged with a Photometrics Quantix KAF1401E CCD camera and iVision 4.0 software (BioVision Technologies). The fluorescence intensity at a given area was calculated as the mean of the brightness of the 1,363,095 pixels of each image.

Pin-on-disk testing

Unidirectional wear tests were performed on a custom-built pin-on-disk tribotester [29]. UHMWPE wear pins (length 19.05 mm, diameter 6.35 mm, and end radius of curvature 3.175 mm, with a 2 mm diameter flat, RMS roughness ~0.030 μm, microtomed into one end) were articulated against a CoCr disk, R_a 0.027 ± 0.001 μm, sliding speed 36 mm/sec, at room temperature, in bovine calf serum (HyClone) diluted 1:1 v/v with deionized water and 0.1% wt/v sodium azide (Sigma-Aldrich) added. To counteract evaporation, the serum volume was replenished with deionized water at a rate of 1.0 mL/hr using a syringe pump (Cole-Parmer). The mean contact pressure P, calculated using Equation 1, was 3 or 21 MPa, and the sliding distance was 2500 or 500 m, respectively. After the tests finished, the pins were rinsed in deionized water and examined by ATR-FTIR to determine coating survival.

$$P = \frac{L}{A} \qquad [1]$$

L is the normal load applied directly above the pin on the pin-on-disk apparatus; A is the nominal contact area, the area of the entire 2 mm diameter flat microtomed onto the pin.

Atomic force microscopy (AFM) scratch testing

The AFM scratching technique, which was used to evaluate both coating thickness and miscroscale wear behavior, has been described in more detail elsewhere [30]. Briefly, atomic force microscopy was performed with an Asylum Research MFP-3D instrument using silicon cantilevers (Nanosensors FM tips, spring constant ~2 nN/nm, radius of curvature ~ 5 nm) in PBS (Gibco, pH 7.3). As shown in Figure 2, the surface was sequentially imaged non-destructively in tapping mode (image size: 8 μm x 2 μm); lithographed in contact mode to produce a rectangular defect (ten passes along the lithography path, normal force 1.0-2.0 μN); and scratched in contact mode (1.0-2.5 μN) inside the 4 μm x 1 μm wear box enclosed by the lithographic defect. After lithography (which was omitted from some sequences to evaluate the behavior of fully intact coatings) and again after every 1-4 scratches, the surfaces was re-imaged in tapping mode. During scratching, the AFM also recorded images, which show the real-time scratching behavior of the coatings. All scratching and imaging steps were performed with the same AFM tip. However, any blunting or adhesion of wear particles that may have occurred during wear did not appear to affect the subsequent image quality.

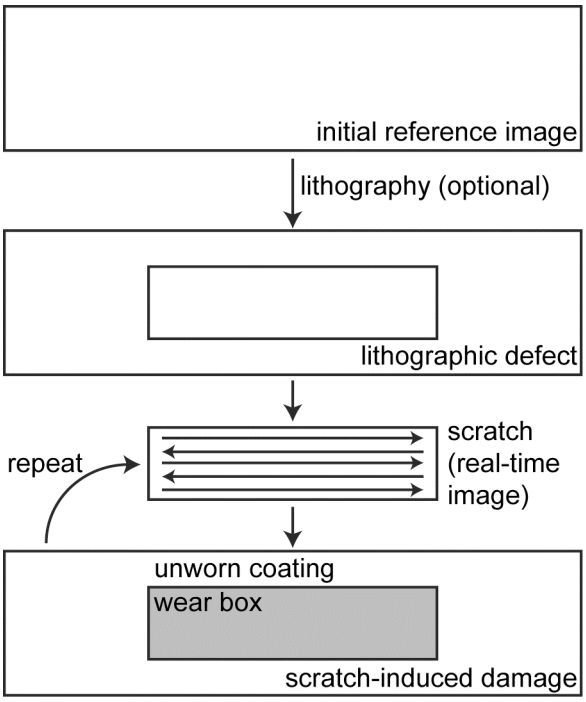

Figure 2: The AFM scratch process. The surface was sequentially imaged, lithographed, imaged, scratched (which also generated a real-time image of the wear box), imaged, re-scratched, and re-imaged.

Image analysis was performed using MPD-3D software and Igor Pro 6.02A. The image taken before the first contact mode scratch served as a reference for all tapping-mode images. After scratching and re-imaging, the reference image was subtracted from each subsequent image to produce images that highlighted wear-induced changes in the topography. The smooth region surrounding the wear box is unworn coating. The height of the unworn area was used as the zero point for calculation of the volumetric wear rate of the coating.

Results

Coating Characterization

This chapter evaluates the wear behavior of coatings produced at 50°C. The XPS, ATR-FTIR, contact angle goniometry, and protein adsorption results for these coatings are presented in detail in Chapter 4. Briefly, all plasma-treated samples exhibit similar surface chemistry, which is highly PEG-like, with an ether content of 82-83%. As expected, the PEGylated surfaces are much more hydrophilic than uncoated UHMWPE, with a mean contact angle of 48.1° compared to 90.4° for uncoated UHMWPE, and the PEGylated surfaces adsorb considerably less protein than the uncoated UHMWPE. This suggests that, unlike UHMWPE particles, fragments of the PEG-like coating will not cause an immune response in vivo.

Pin-on-disk testing: microscale and mesoscale coating tribology

Pin-on-disk tribotesting was used to determine the conditions under which the coating can survive; survival was defined as the presence of the main ether peak at 1115 cm^{-1} in ATR-FTIR spectra of the entire pin surface taken after the wear test ended. 21 MPa, 500 m tests were used to mimic the contact pressure found in the knee, while 3 MPa, 2500 m tests were used to mimic the hip. Longer runs were used for the 3 MPa experiments after preliminary results indicated that the coatings readily survived shorter tests. The results are shown in Table 1.

Table 1: Coating survival results

Samples	Pin-on-disk conditions		Clinical scenario	Number of pins	Outcome (measured by ATR-FTIR of entire pin surface)
	Mean contact pressure, MPa	Sliding distance, m			
PEG-like coating > 140 nm thick	21	500	Knee	5	Coating wore off completely: 5
PEG-like coating > 200 nm thick	3	2500	Hip	4	Coating present: 3 (2 >250 nm thick, 1 210 nm thick) Coating wore off completely: 1 (210 nm thick)

No PEG-like coatings survived the tests conducted at 21 MPa, regardless of coating thickness (>140 nm, 210 nm, >250 nm). During the lower-pressure tests, two pairs of pins with different initial coating thicknesses (210 nm and >250 nm) were evaluated. Of the three coatings that survived, two had an initial thickness of >250 nm, and one had an initial thickness of 210 nm.

To determine the mesoscale wear mechanisms of the coatings that survived, the pins subjected to the 3 MPa, 2500 m wear tests were then examined in more detail by ATR-FTIR mapping. Instead of taking a single spectrum of the entire 2 mm diameter pin surface, ATR-FTIR mapping takes spectra with much smaller spot sizes (here, 25 μm) at specified intervals (37.5 μm) over an area several hundred microns on each side.

The maps in Figure 3 show the ratio of the area under the ether and hydrocarbon peaks. The ether peak derives from the PEG-like coating, while the hydrocarbon peak is primarily from the UHMWPE substrate. The ratio normalizes for differences in the signal that arise from the curvature of the ATR crystal. Maps of unworn PEG-like

coatings, which were taken on samples of comparable chemistry and thickness, show that the thickness of the coatings varies moderately across the surface. After pin-on-disk testing, the coatings exhibited two primary morphologies: relatively constant thickness across the mapped regions of the PEG-like layer initially 210 nm thick, and wear (both smooth and rougher) combined with coating removal in the >250 nm thick coatings. In the latter case, coating loss occurred on the scale of hundreds of microns.

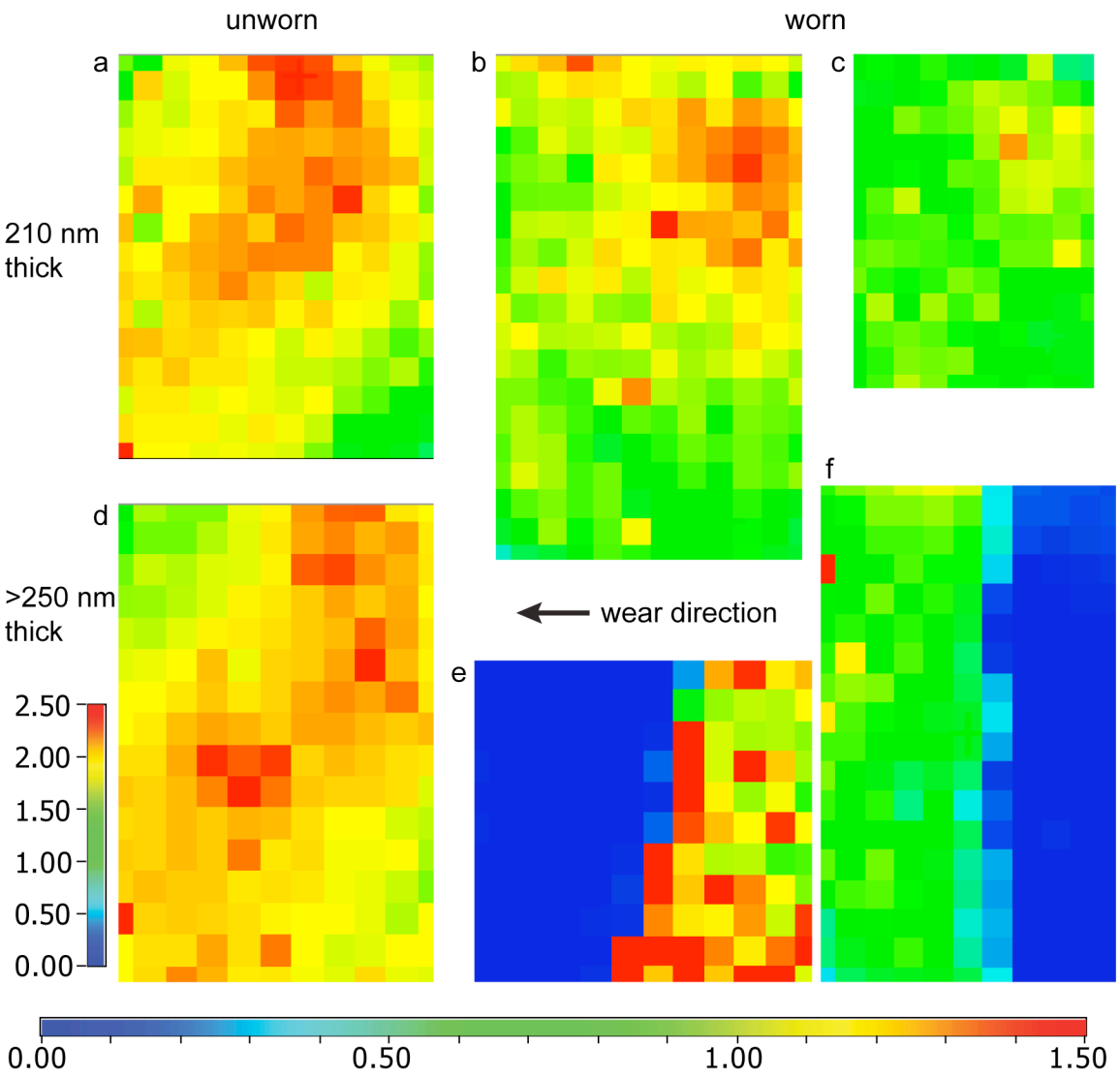

Figure 3: ATR-FTIR maps of the ether/hydrocarbon ratio, which measures the relative thickness of the PEG-like coating across each surface, on two unworn controls and two worn pin-on-disk surfaces of different initial coating thickness. In all maps, 1 pixel = 37.5 μm; map sizes vary based on the sample area in direct contact with the ATR crystal during imaging. a) An unworn PEG-like coating, mean thickness 210 nm. b-c) two different areas on the same wear pin with initial mean coating thickness 210 nm. d) An unworn PEG-like coating, mean thickness >250 nm. b-c) two different areas on the same wear pin with initial mean coating thickness >250 nm. Note that the ether/hydrocarbon ratio ranges from 0-1.5 in all maps except for d), which has a range of 0-2.5.

AFM scratching: microscale tribology

Atomic force microscopy was used to model the asperity wear behavior of the PEG-like coatings by repeatedly scratching the coatings with a sharp AFM tip (~10 nm radius) in contact mode, which produced real-time images of the wear box during scratching. In addition, the surface was non-destructively imaged in tapping mode after every 1-4 scratches to track the progression of surface damage. Four different coating thicknesses, ranging from 125 nm to >250 nm, were tested.

During nanoscratching, uncoated UHMWPE consistently formed ripples with an average period of ~1 μm perpendicular to the direction of wear. This behavior, which appears in Figure 4, is remarkably similar in both appearance and period to the surface texture that develops on UHMWPE in reciprocating wear tests and hip joint simulators [2, 31-33]; it also appears to confirm at the microscale a millimeter-scale model of UHMWPE wear against a sliding wedge proposed by Fang et al [34].

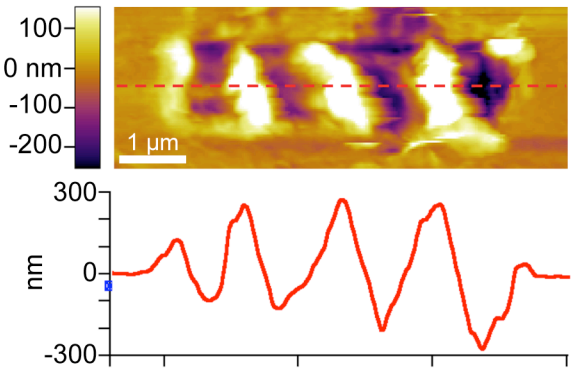

Figure 4: Characteristic ripple formation on uncoated UHMWPE after nanoscratching. The linescan shows the profile of the surface along the dotted red line on the image.

At the microscale level, the PEG-like coatings exhibited three different types of damage – roughening, thinning, and deep tearing – all distinctly different from the

characteristic ripples formed by uncoated UHMWPE. Individual surfaces usually failed as a result of combinations of damage behaviors (roughening followed by thinning, thinning combined with localized deep tearing) and all behaviors occurred in coatings of at least three different thicknesses, suggesting that they are intrinsic to the PEG-like material, rather than related to the coating thickness.

Roughening, shown in Figure 5, consists of small, shallow tears on the coating surface. Wear particles either were not completely removed, or were removed and immediately deposited nearby, such that there was no overall loss of coating volume in the worn region. Roughening usually occurred early in the wear process, on samples without a lithographic defect, or with a shallow/incomplete defect. In a few cases, roughening took place after successive thinning; this likely resulted from a lithographic defect that did not penetrate the full thickness of the coating, such that the coating thinned until it reached the bottom of the defect, then roughened like a defect-free surface again.

The roughening process could have occurred by two different mechanisms, adhesion and microfracture. In adhesive wear, a small area of one articulating surface sticks to a small area of the countersurface. As sliding continues, the harder surface (the AFM tip) pulls a particle out of the softer surface (the PEG-like coating). Alternately, during microfracture, subsurface cracks form in one material as it articulates against the countersurface. When a crack directed normal to the surface intersects a subsurface crack, a wear particles is liberated. Either mechanism could produce the roughening seen here. However, the wear particles may not have fully dissociated from the PEG-like coating, which would explain why there is no loss of coating volume.

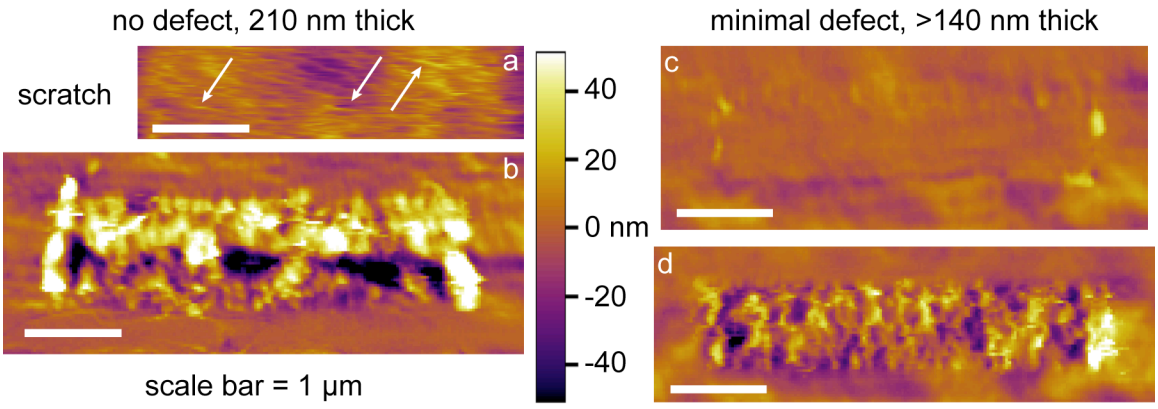

Figure 5: Roughening of the wear box in coatings with (c-d) and without (a-b) lithographic defects. a) The real-time images of the contact-mode 1 μN scratch that caused the roughening in b) the tapping-mode image of the wear box and surrounding unworn region. Superficial tearing appears throughout the scratching image, and is highlighted by the arrows. c) A very shallow lithographic defect around an unworn wear box. d) The same wear box after two 1 μN scratches. The 210 nm thick coating was produced in the same plasma deposition batch as the 210 nm thick coatings subjected to pin-on-disk testing and ATR-FTIR mapping (see Figure 3).

Thinning, shown in Figure 6, removed a uniform layer of material from the coating surface, generating a smooth wear box of uniform depth. In most cases, successive scratches deepened the worn area without roughening it, although deep tearing often eventually occurred in localized regions of surfaces that otherwise wore smoothly (see Figure 7). Successive thinning that produces a smooth worn area appears to result from continuous adhesive wear by the AFM tip.

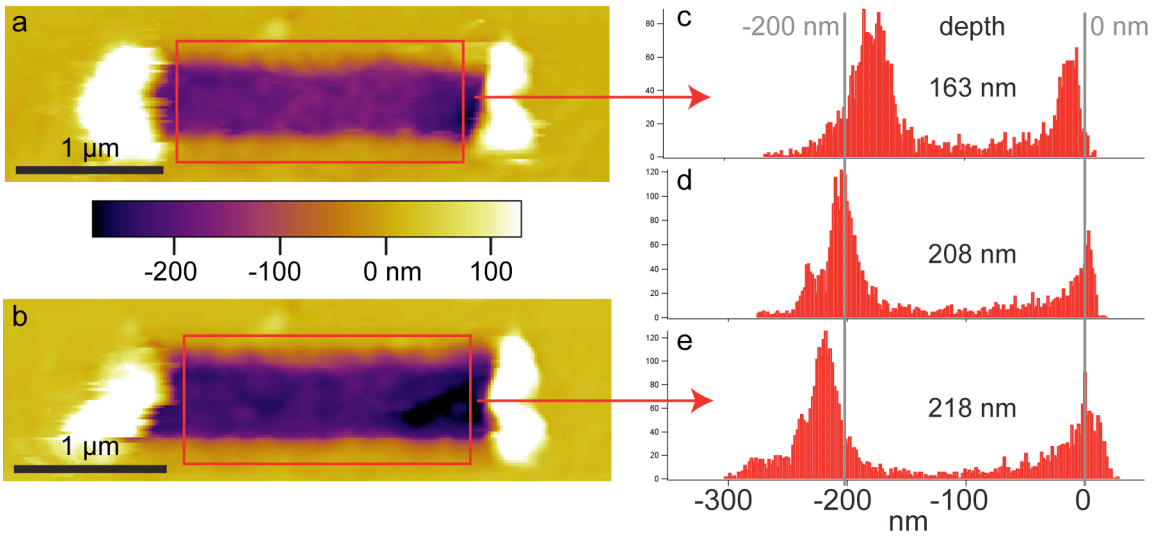

Figure 6: Successive thinning of a PEG-like coating with initial thickness >250 nm. The images were taken after a) two 2 μN scratches and b) four additional 1 μN scratches. c-e) The height distributions in the wear box plus a small area of unworn coating, outlined in red in a) and b). From top to bottom, the histograms correspond to images taken after c) two 2 μN scratches (image a), d) two additional 1 μN scratches, e) two additional 1 μN scratches (image b; six scratches total). This coating was produced in the same plasma deposition batch as the >250 nm surfaces subjected to pin-on-disk testing and ATR-FTIR mapping (see Figure 3).

Coatings of three different thicknesses exhibited thinning behavior, and the average adhesive wear factor k was calculated for each coating according to Archard's Law for adhesive wear,

$$k = \frac{V}{Lx} \qquad [2],$$

where k is the adhesive wear factor, V is the wear volume, L is the normal load, and x is the sliding distance [35]. The results appear in Table 2.

Table 2: Thinning/adhesive wear factors

Coating thickness, nm	k, $nm^2/\mu N$	Standard deviation, $nm^2/\mu N$
125	243	122
>140	196	96
>250	211	102

As expected, all three coatings exhibit similar wear rates. The high standard deviations result from the fact that the wear rate was not always constant over the course of the AFM scratching experiments. Coating loss often decreased as scratching progressed, possibly because the much stiffer UHMWPE substrate began to support more of the load as the coating was removed, changing the effective stiffness of the system.

Deep tearing, shown in Figure 7, removed large pieces of the coating from either localized areas of the wear box, producing deep wells (d-g), or the entire wear box (a-c). The localized regions were often, though not always, located at the corners of wear boxes with initial defects. This suggests a delamination mechanism, with subsurface cracks/tears intersecting the lithographic defect to liberate sections of coating that usually exceeded 100 nm in depth (as opposed to tens of nanometers for microfracture), and ranged from less than 0.5 μm to 4 μm (the width of the entire wear box) in length and width. The cyclic wear rate due to delamination was not calculated because delamination depends primarily on factors such as the crack propagation behavior of the PEG-like coating that could not be readily determined.

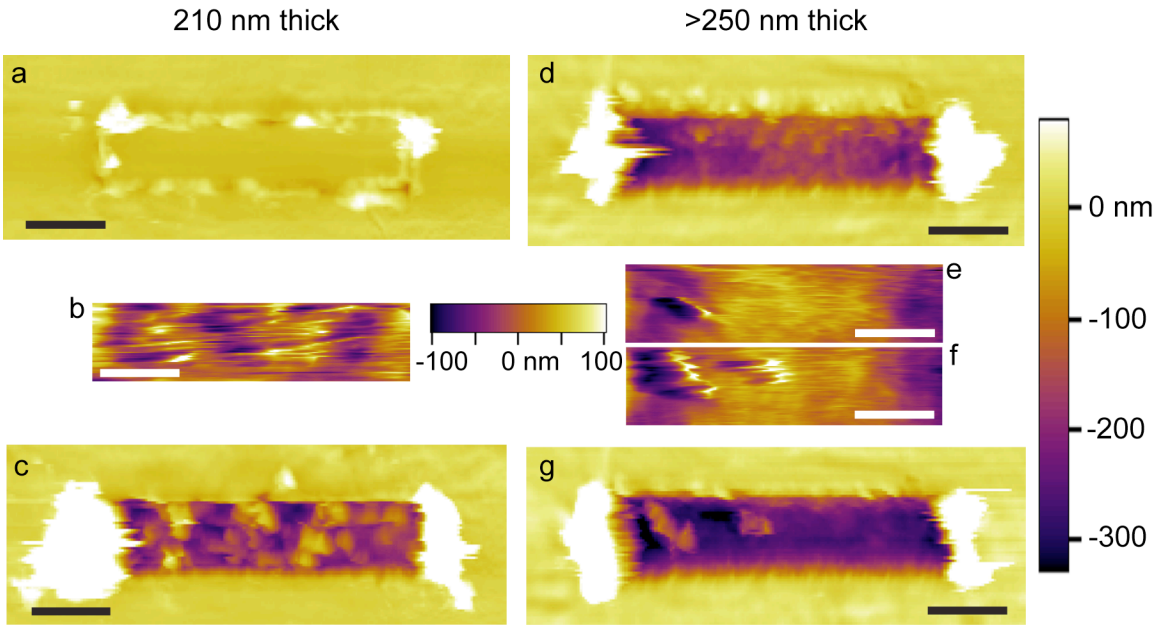

Figure 7: Deep tearing of coatings 210 nm (a-c) and >250 nm (d-g) thick. In all images, the scale bar represents 1 μm. Images a, c, d, and g correspond to the large legend bar on the right; scratches b, e, and f correspond to the small legend bar in the middle of the figure. a, d) The surfaces before the scratches that caused tearing. b, e, and f) The real-time images taken during contact-mode scratching of the wear box. Since they were taken by the tip as it scratched the coating, the contact-mode images show only the worn region. c, g) The wear box, surrounded by unworn coating, after tearing occurred. In these sequences, the 210 nm thick coating tore throughout the wear box during a single 2 μN scratch (b), while the >250 nm thick coating tore in one place during e) and a second spot during f) (sequential 1.5 μN scratches), generating two deeper holes on the left side of the wear box in g). During scratches e) and f), the middle and right side of the >250 nm thick coating wore by thinning, an instance of mixed-mode wear that occurred repeatedly during these experiments.

Discussion

The concept of lubricating the UHMWPE surface of total joint replacements with soft hydrophilic polymer coatings is relatively new. To date, only three other hydrogel coatings have been investigated: polyelectrolyte multilayers [17], hyaluronan [18], and MPC [19]. These surface modifications vary not only in chemical structure, but also in terms of molecular architecture and bonding to the UHMWPE and molecular architecture. The PEMs consisted of interpenetrating or crosslinked networks adsorbed

rather than covalently bonded to the UHMWPE. The hyaluronan coating was crosslinked and adsorbed to a porous UHMWPE surface. The MPC coating consisted of a brush layer of chains covalently end-grafted to the UHMWPE.

This study introduces PEG-like coatings as a potential surface modification for UHMWPE for orthopedic applications. Unlike all prior hydrogel coatings, it combines the strongest molecular architecture – a crosslinked network – with the strongest attachment to UHMWPE – covalent bonding. Characterization of the coatings indicated that they retain a predominantly PEG-like chemical structure, with greater than 80% ether content, and they are both hydrophilic and resistant to protein deposition. Pin-on-disk testing determined that while they cannot withstand the high contact pressures present in total knee replacements, they show promise for use in total hip replacements where the contact stresses are lower.

Tribological analysis was conducted in order to determine the wear mechanisms occurring within the coating at the macro-, meso-, and microscales. At the macroscale, pin-on-disk testing of a 2 mm diameter contact area, the coating was on the pin, and therefore the coating remained in continuous sliding contact throughout the entire test, a much more rigorous test than if the coating had been placed on the disk. The macroscale results are promising: ATR-FTIR spectra of the coatings subjected to 3 MPa mean contact pressure indicated that PEG-like coating remained present on three of the four wear pins, as evidenced by the presence of an ether peak at 1115 cm^{-1}. However, this analysis could not evaluate the distribution of the coating across the surface.

The mesoscale ATR-FTIR mapping provided a detailed analysis of the coating thickness across the surface by examining spots 25 μm in diameter, with a spacing of

37.5 μm. At this scale, the coatings exhibited one of two distributions: relatively even thickness across regions hundreds of square microns (Figure 3b-c), or loss of large portions of coating adjacent to intact regions (Figure 3e-f). In the latter case, the coating appears to be removed entirely, exposing bare UHMWPE (or leaving behind a layer of PEG so thin as to be undetectable by ATR-FTIR).

Microscale AFM scratching yielded three predominant wear behaviors: surface roughening, thinning, and deep (often through-thickness) tearing. Roughening resulted from very shallow tearing, visible during the contact-mode AFM scratch, at the coating surface, likely due to an adhesive and/or microfracture wear mechanism. This type of wear occurred only in the absence of a significant lithographic defect, and it always preceded other wear behaviors. Unfortunately, if this type of wear also occurred on the pin-on-disk surfaces due to asperity contact with the CoCr disk, it would not have been detectable by ATR-FTIR mapping because it would be indistinguishable from the localized coating thickness variation inherent to the surfaces, as shown in the unworn coatings in Figure 3a and d.

However, both thinning and tearing occurred at the micro- and mesoscale. The worn pin surfaces mapped in Figure 3b and c, as well as the left side of the region in Figure 3f, are all relatively smooth, reminiscent of the thinned but smooth surfaces generated by adhesive wear during AFM scratching (see Figure 6). These regions either did not wear at all – a result not observed during the AFM scratch tests, regardless of whether or not the surfaces had a lithographic defect – or wore evenly across an area hundreds of microns in each direction, probably by an adhesive wear mechanism.

Deep tearing, which removed regions of coating more than 100 nm thick and up to 4 μm (the full width of the wear box) across during one or two AFM scratches, appears to involve delamination. At the mesoscale, the phenomenon is much larger, with hundreds of square microns of coating tearing away cleanly (see Figure 3e and f). Unfortunately, it is impossible to determine why the coating tore at a given location. However, at the microscale, deep tears often formed in corners of the wear box, where the lithographic defect had already broken bonds on two sides of potential wear particles, creating a crack directed downward from the coating surface. This suggests that delamination occurs more readily in the presence of a defect.

Two sets of PEG-like coatings (210 nm and >250 nm thick) were examined at all three scales. Despite their greater thickness, both wear pins with coatings >250 nm thick exhibited significant localized delamination at the mesoscale, with hundreds of square microns of coating removed from the surface. Both coatings survived in some places, but also wore away to expose large regions of bare UHMWPE. At the microscale (AFM modeling of asperity contact), the >250 nm thick coating failed by either pure delamination or a combination of delamination and adhesive wear. A combined process would readily explain the mesoscale results.

The 210 nm coatings behaved quite differently. At the macroscale, only one of the two surfaces survived the 3 MPa pin-on-disk wear test. The coating that survived remained intact at the mesoscale as well, exhibiting no holes in the coating on the order of 25 μm in diameter or larger. This indicates that it either thinned or did not wear at all. Interestingly, at the microscale, the 210 nm thick coating consistently delaminated during AFM nanoscratching. This suggests that, at the macro- and mesoscales, one pin surface

fully delaminated, while the other did not wear. If the delamination mechanism could be delayed/prevented, perhaps by tailoring the plasma deposition process to increase the covalent bonding at the UHMWPE-PEG interface (which Johnston et al achieved by varying the plasma power [25]), this coating might be appropriate for clinical use.

Conclusions

The coatings examined in this study represent the first generation of PEG-like materials evaluated as lubricious surfaces for UHMWPE in total joint replacements. The PEGylated surfaces are hydrophilic, with contact angles of 45-50°, and resist protein deposition. In addition, the coatings can at least partially withstand a contact pressure of 3 MPa, which is comparable to the loading in total hip replacements.

Tribological studies of the wear behavior of the PEG-like coatings determined that they fail predominantly by a combination of adhesive wear and partial or total delamination, which occurs more readily at sites that already have a surface defect. These results suggest several avenues of future research to improve the wear resistance of the PEG-like coatings. First, to prevent the coatings from delaminating at the UHMWPE-PEG interface, the plasma deposition conditions should be altered to promote increased covalent bonding between the substrate and the coating. Second, increased crosslinking should be investigated to strengthen the coatings. This has the potential to improve resistance to both thinning and delamination within the bulk of the PEG-like coating.

References

1. Kurtz, S.M., *The UHMWPE Handbook: ultra-high molecular weight polyethylene in total joint replacement*. 2004, Boston: Elsevier Academic Press.
2. McKellop, H.A., et al., *The Origin of Submicron Polyethylene Wear Debris in Total Hip-Arthroplasty.* Clinical Orthopaedics and Related Research, 1995(311): p. 3-20.
3. Harris, W.H., *Osteolysis and Particle Disease in Hip-Replacement - a Review.* Acta Orthopaedica Scandinavica, 1994. **65**(1): p. 113-123.
4. Ingham, E. and J. Fisher, *Biological reactions to wear debris in total joint replacement.* Proceedings of the Institution of Mechanical Engineers Part H-Journal of Engineering in Medicine, 2000. **214**(H1): p. 21-37.
5. Wright, T.M. and D.L. Bartel, *The Problem of Surface Damage in Polyethylene Total Knee Components.* Clinical Orthopaedics and Related Research, 1986(205): p. 67-74.
6. Wright, T.M., et al., *Failure of Carbon Fiber-Reinforced Polyethylene Total Knee-Replacement Components - a Report of 2 Cases.* Journal of Bone and Joint Surgery-American Volume, 1988. **70A**(6): p. 926-932.
7. Kurtz, S.M., et al., *Advances in the processing, sterilization, and crosslinking of ultra-high molecular weight polyethylene for total joint arthroplasty.* Biomaterials, 1999. **20**(18): p. 1659-1688.

8. Edidin, A.A., et al., *Plasticity-induced damage layer is a precursor to wear in radiation-cross-linked UHMWPE acetabular components for total hip replacement.* Journal of Arthroplasty, 1999. **14**(5): p. 616-627.

9. Ries, M.D. and L. Pruitt, *Effect of cross-linking on the microstructure and mechanical properties of ultra-high molecular weight polyethylene.* Clinical Orthopaedics and Related Research, 2005(440): p. 149-156.

10. Baker, D.A., A. Bellare, and L. Pruitt, *The effects of degree of crosslinking on the fatigue crack initiation and propagation resistance of orthopedic-grade polyethylene.* Journal of Biomedical Materials Research Part A, 2003. **66A**(1): p. 146-154.

11. Tower, S.S., et al., *Rim cracking of the cross-linked longevity polyethylene acetabular liner after total hip arthroplasty.* Journal of Bone and Joint Surgery-American Volume, 2007. **89A**(10): p. 2212-2217.

12. Furmanski, J., et al., *Fracture of highly cross-linked UHMWPE acetabular liners.* Journal of Bone and Joint Surgery-American Volume, 2008. **submitted**.

13. Shi, W., X.Y. Li, and H. Dong, *Improved wear resistance of ultra-high molecular weight polyethylene by plasma immersion ion implantation.* Wear, 2001. **250**: p. 544-552.

14. Klapperich, C., L. Pruitt, and K. Komvopoulos, *Nanomechanical properties of energetically treated polyethylene surfaces.* Journal of Materials Research, 2002. **17**(2): p. 423-430.

15. Bertoti, I., et al., *Nitrogen-PBII modification of ultra-high molecular weight polyethylene: Composition, structure and nanomechanical properties.* Surface & Coatings Technology, 2007. **201**(15): p. 6839-6842.

16. Marcondes, A.R., et al., *Improvements of ultra-high molecular weight polyethylene mechanical properties by nitrogen plasma immersion ion implantation.* Brazilian Journal of Physics, 2004. **34**(4B): p. 1667-1672.

17. Pavoor, P.V., et al., *Wear reduction of orthopaedic bearing surfaces using polyelectrolyte multilayer nanocoatings.* Biomaterials, 2006. **27**(8): p. 1527-1533.

18. Zhang, M., et al., *A novel ultra high molecular weight polyethylene-hyaluronan microcomposite for use in total joint replacements. II. Mechanical and tribological property weight composite for evaluation.* Journal of Biomedical Materials Research Part A, 2007. **82A**(1): p. 18-26.

19. Moro, T., et al., *Surface grafting of artificial joints with a biocompatible polymer for preventing periprosthetic osteolysis.* Nature Materials, 2004. **3**(11): p. 829-836.

20. Ishihara, K., et al., *Photoinduced graft polymerization of 2-methacryloyloxyethyl phosphorylcholine on polyethylene membrane surface for obtaining blood cell adhesion resistance.* Colloids and Surfaces B-Biointerfaces, 2000. **18**(3-4): p. 325-335.

21. Roberts, M.J., M.D. Bentley, and J.M. Harris, *Chemistry for peptide and protein PEGylation.* Advanced Drug Delivery Reviews, 2002. **54**(4): p. 459-476.

22. Caliceti, P. and F.M. Veronese, *Pharmacokinetic and biodistribution properties of poly(ethylene glycol)-protein conjugates.* Advanced Drug Delivery Reviews, 2003. **55**(10): p. 1261-1277.

23. Allen, T.M., *The Use of Glycolipids and Hydrophilic Polymers in Avoiding Rapid Uptake of Liposomes by the Mononuclear Phagocyte System.* Advanced Drug Delivery Reviews, 1994. **13**(3): p. 285-309.

24. Gref, R., et al., *'Stealth' corona-core nanoparticles surface modified by polyethylene glycol (PEG): influences of the corona (PEG chain length and surface density) and of the core composition on phagocytic uptake and plasma protein adsorption.* Colloids Surf B Biointerfaces, 2000. **18**(3-4): p. 301-313.

25. Johnston, E.E., J.D. Bryers, and B.D. Ratner, *Plasma deposition and surface characterization of oligoglyme, dioxane, and crown ether nonfouling films.* Langmuir, 2005. **21**(3): p. 870-881.

26. Cao, L., et al., *Glow discharge plasma treatment of polyethylene tubing with tetraglyme results in ultralow fibrinogen adsorption and greatly reduced platelet adhesion.* Journal of Biomedical Materials Research Part A, 2006. **79A**(4): p. 788-803.

27. Ratner, B.D., A. Chilkoti, and G.P. Lopez, *Plasma Deposition and Treatment for Biomaterial Applications*, in *Plasma Deposition, Treatment, and Etching of Polymers*, R. d'Agostino, Editor. 1990, Academic Press, Inc.: San Diego.

28. Heuberger, M.P., et al., *Protein-mediated boundary lubrication in arthroplasty.* Biomaterials, 2005. **26**(10): p. 1165-1173.

29. Klapperich, C., K. Komvopoulos, and L. Pruitt, *Tribological properties and microstructure evolution of ultra-high molecular weight polyethylene.* Journal of Tribology-Transactions of the ASME, 1999. **121**(2): p. 394-402.

30. Kane, S.R., P.D. Ashby, and L.A. Pruitt, *ATR-FTIR as a Thickness Measurement Technique for Hydrated Polymer-on-Polymer Coatings.* Biomaterials, 2008. **submitted**.

31. Wang, A., C. Stark, and J.H. Dumbleton, *Mechanistic and morphological origins of ultra-high molecular weight polyethylene wear debris in total joint replacement prostheses.* Proceedings of the Institution of Mechanical Engineers Part H-Journal of Engineering in Medicine, 1996. **210**: p. 141-155.

32. Bragdon, C.R., et al., *The importance of multidirectional motion on the wear of polyethylene.* Proceedings of the Institution of Mechanical Engineers Part H-Journal of Engineering in Medicine, 1996. **210**: p. 157-165.

33. Zhou, J., et al., *Tribological and nanomechanical properties of unmodified and crosslinked ultra-high molecular weight polyethylene for total joint replacements.* Journal of Tribology-Transactions of the ASME, 2004. **126**(2): p. 386-394.

34. Fang, H.W., S.M. Hsu, and J.V. Sengers, *Single wedge sliding tests to investigate the mechanism of UHMWPE particle generation with microfabricated surface textures.* Polymer Testing, 2006. **25**(3): p. 424-434.

35. Archard, J.F., *Contact and Rubbing of Flat Surfaces.* Journal of Applied Physics, 1953. **24**(8): p. 981-988.

Chapter 7

Conclusions and Future Directions

Introduction

A crosslinked plasma-deposited PEG-like coating on UHMWPE has been developed as a lubricious surface to reduce wear of the acetabular component of total hip replacements. The effect of various plasma deposition parameters on the PEG-like coating chemistry is discussed in detail in Chapter 3. The chemical composition, hydrophilicity, and protein deposition resistance of two promising sets of coatings – both tetraglyme-based, but produced at 40°C or 50°C – appear in Chapter 4. Chapter 5 proposes a novel method based on ATR-FTIR for measuring the thickness of hydrated polymer-on-polymer systems such as the PEG-like coatings on UHMWPE. Chapter 6 investigates the wear behavior of the 50°C coatings at three length scales – millimeter, tens to hundreds of microns, and under ten microns – in order to identify the fundamental wear mechanisms and propose modifications to improve wear resistance.

Each step of the investigative process, from development of the plasma deposition protocol to the final stages of wear testing conducted on the PEGylated surfaces, both answered some questions and raised many more. This chapter identifies the most critical

outstanding issues and suggests lines of inquiry that would enhance understanding of the basic science and further progress toward the ultimate goal of the project: developing a lubricious wear-resistant coating that increases the longevity of total hip replacements.

Plasma deposition

Plasma deposition is a powerful but complex process with an almost infinite number of variables. To adapt this process for commercial use, several crucial parameters must be further considered: spatial variation of the plasma, chamber temperature, and deposition power. This study took advantage of spatial variation in order to efficiently generate coatings with a wide range of thicknesses. However, in order to produce a uniform coating over the entire surface of an acetabular cup, the plasma deposition process would have to be less spatially-dependent than the process used in this study. This could likely be achieved by circulating the vapor within the chamber to achieve homogeneous tetraglyme vapor concentrations, or by rotating the cups during deposition. These measures should also improve batch-to-batch reproducibility, as substrate location contributed to the variability observed in these experiments.

Deposition power and chamber temperature both affect the rate of the coating deposition, as well as the chemistry of the resulting coating, and they are not independent because raising the power increases the chamber temperature. Better temperature control could be achieved by using a small, well-insulated chamber with built-in, feedback-controlled heating and cooling capacity. Both chamber temperature and deposition power should be explored more thoroughly in order to optimize the desired coating

chemistry, with particular attention to increasing the covalent bond density between the coating and the substrate, and determining the relationship between each variable and the resulting crosslink density.

In addition to equipment improvements, the next step in plasma process development would be to perform systematic optimization of the process based on all of the major variables discussed in Chapter 3, with particular attention to the effects of temperature and power. Such a study might also yield insight into the mechanisms of competing reactions – monomer fragmentation, recombination, deposition, crosslinking, and desorption – occurring during the plasma process, which would improve control of the resultant coating chemistry.

Coating chemistry and molecular architecture

Perhaps the most obvious approach to reducing wear is to make materials harder. This tactic is both highly intuitive and well-supported by relationships such as Archard's Law,

$$V = k\frac{Lx}{H} \qquad [1].$$

Consequently, researchers have attempted to harden UHMWPE through means such as carbon fiber reinforcement [1, 2]; bulk [3] or surface [4, 5] crosslinking; and the application of diamond-like coatings [6, 7]. But the natural joint, which has a coefficient of friction 1-2 orders of magnitude below that found in artificial joint replacements [8], and which often lasts more than 75 years, employs a soft hydrogel – cartilage – to bear the load and lubricate the articulating interface. A small number of investigators have attempted to achieve similar success by coating UHMWPE with hydrophilic polymers.

These have included both biologically-inspired surfaces, namely hyaluronan [9] and a phosphorylcholine derivative [10], as well as one synthetic material, a combination of poly(acrylic acid) and polyallylamine [11]. Following the latter approach, this study proposed the use of crosslinked poly(ethylene glycol).

Due to the relative immaturity of the field, many basic questions remain. What factors dictate the lubricity and wear resistance of these materials – chemical structure, hydrophilicity, coating thickness, mode of surface attachment? What is the role of molecular architecture, or the connectivity of the polymer chains? Do brush layers behave differently than crosslinked coatings of nearly-identical chemical structure, and how great is the effect of the molecular weight between crosslinks? Does protein deposition resistance affect lubricity or wear behavior?

One significant challenge in answering these questions is the difficulty in isolating variables. Coatings with different chemical structures likely also have different substrate bonding and crosslink densities. Changing the molecular architecture to examine crosslinked versus end-grafted coatings also slightly changes the chemistry, and can significantly change the number of bonds between the coating and the surface, as well as the thickness of the layer. While thickness can be adjusted via process parameters or the length of end-grafted polymer chains, it is difficult to control the density of covalent bonding to the substrate, and may be even more difficult to quantify the degree of attachment.

Despite these challenges, it is important to identify the critical factors that determine coating performance in order to make rational design decisions. To this end, the first step would be a general comparison of the wear behavior of coatings with

widely-varying chemistries (charged and neutral, with a range of hydrophilicities, including both protein-resistant and protein-adsorbent hydrogels). More specific molecular architecture studies comparing brush layers and coatings of varied crosslink density, but otherwise nearly identical chemical structure, are also warranted.

Preliminary results from microscale wear testing of the PEG-like coatings highlight the tribological impact of small differences in coating chemistry and molecular architecture. As reported in Chapter 4, the 50°C coatings exhibit slightly higher hydrophilicity and ether content, with a corresponding decrease in hydrocarbon (see Table 1), as compared to the 40°C coatings. The lower hydrocarbon content of the 50°C coatings appears to reflect a decrease in crosslinking, which allows the 50°C coatings to swell more. Therefore, the ATR-FTIR hydrated thickness calibration curve developed for the more-crosslinked 40°C coatings underestimates the thickness of the 50°C coatings (see Table 2).

Due to the constraints of surface attachments, coatings that are covalently bonded to surfaces swell in only one direction, perpendicular to the surface. Therefore, the swelling ratio Q, which is inversely related to the crosslink density X, depends only on the change in thickness, t:

$$X \propto \frac{1}{Q} \qquad [2]$$

$$Q = \frac{t_{wet}}{t_{dry}} \qquad [3].$$

For the 50°C coatings, the ratio of the true thickness to the predicted thickness of the 50°C samples is equivalent to the relative swelling ratio of the two materials. The dry thickness is constant because it is simply the amount of coating, measured by ATR-FTIR,

that is present on the same UHMWPE substrate before theoretical prediction or actual swelling.

$$\frac{Q_{50}}{Q_{40}} = \frac{\frac{t_{50}}{t_{dry}}}{\frac{t_{40}}{t_{dry}}} = \frac{t_{true}}{t_{predicted}} \qquad [4]$$

Therefore the thickness ratio reflects the relative degree of crosslinking in the two coatings:

$$\frac{X_{40}}{X_{50}} = \frac{t_{true}}{t_{predicted}} \qquad [5].$$

Table 1: Comparison of coatings produced at 40°C and 50°C

Deposition temperature, °C	XPS C1s bonding			Contact angle, degrees
	% CH_x 285.0 eV	**% C-O 286.5 eV**	% C=O 288.0 eV	
40	17.9 (2.9)	75.1 (2.6)	7.0 (0.8)	53.5 (0.9)
50	11.9 (0.7)	82.6 (1.2)	5.5 (0.6)	48.1 (1.6)

The results displayed are the mean values for all coatings produced at each temperature; the standard deviations are shown in parentheses.

Table 2: Predicted vs. actual coating thicknesses for 50°C samples

Sample	Ether peak area *a*	Predicted thickness, nm t = 11.1*a*	True thickness measured by AFM, nm	$\frac{t_{true}}{t_{predicted}}$
20 min, slot 4	9.8 (0.8)	109 (9)	125	1.15
40 min, slot 5	16.0 (0.4)	178 (5)	210	1.18

Standard deviations are shown in parentheses.

Table 2 shows that the 40°C coatings have 15-18% higher crosslink density than the 50°C coatings. Although relatively small, the difference in crosslink density significantly alters the microscopic wear behavior of the materials, as shown in Figure 1. The more-crosslinked coatings produced at 40°C exhibit only one damage mechanism: tearing that eventually leads to partial or total delamination. In the absence of a

lithographic defect, these coatings were remarkably difficult to damage. Even in the presence of a defect, they still show the ability to resist wear, as evidenced by the fact that the tears on the left side of the wear box in Figure 1b-c grow larger, but do not cause the coating to fully delaminate, even after a total of 16 scratches.

In contrast, the less-crosslinked coatings produced at 50°C, which are discussed at length in Chapter 6, exhibit three microscale damage mechanisms: roughening, thinning, and delamination. They roughen readily, in just one or two 1 μN scratches, in the absence of a defect; they also wear away more slowly by thinning. No coatings produced at 50°C underwent scratching without visible damage, while the 40°C coatings often did when the lithographed defect was not sufficiently deep.

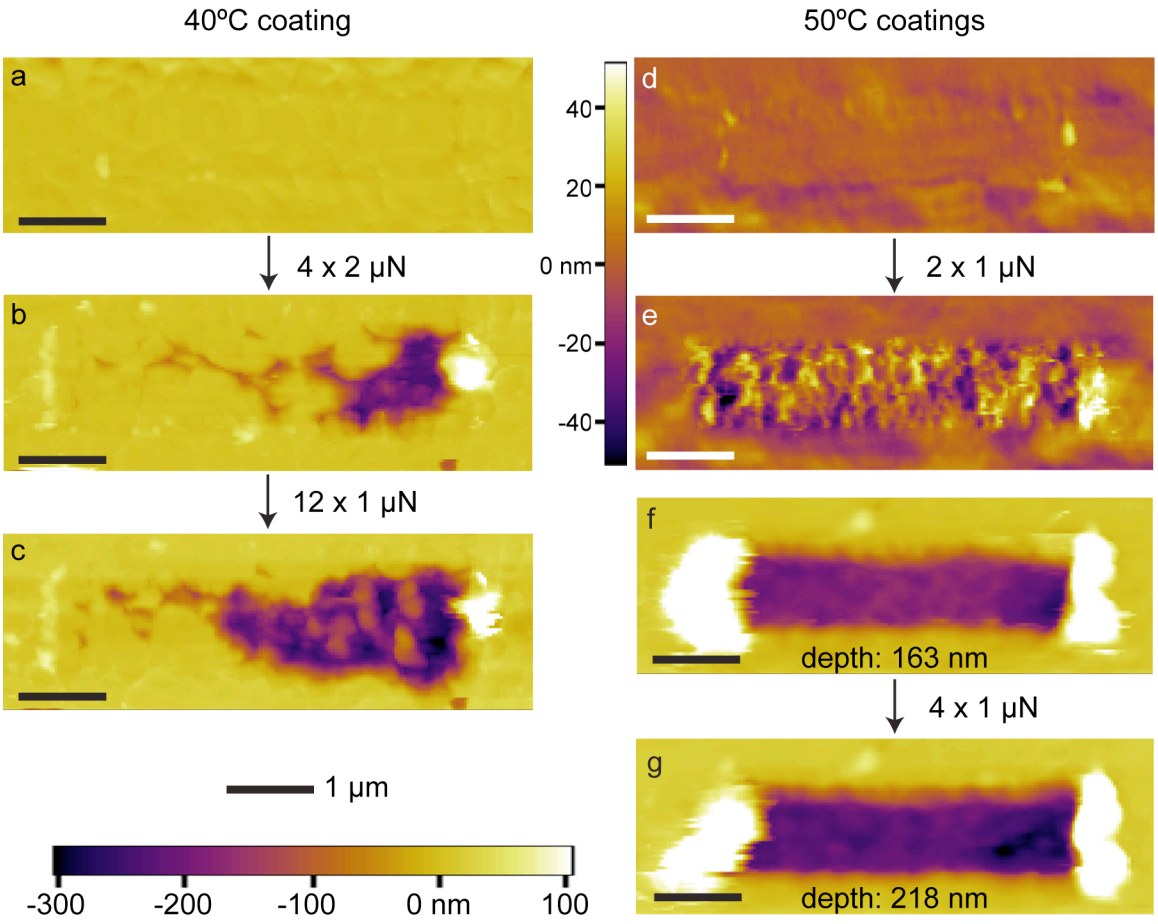

Figure 1: A comparison of characteristic microscale wear behavior of coatings produced at 40°C (a-c) and 50°C (d-e, f-g). a) A 40°C coating surface after lithography but before scratching; the rectangular defect is barely visible. b) After four 2 µN scratches, the right side of the wear box delaminated, while the left and middle exhibited some tearing without delamination. c) After another twelve 1 µN scratches, part of the middle had also delaminated, but the left side was largely intact. The tears grew moderately without delaminating, and the surface exhibited no signs of roughening or thinning. In contrast, the 50°C coatings in d-g damaged readily. d) A 50°C coating surface after lithography but before scratching; again, the defect is barely visible. e) After only two 1 µN scratches, the entire surface of the wear box had roughened considerably, a common result in 50°C surfaces with minimal or no initial defect. f) A different 50°C coating surface after two 2 µN scratches; the coating delaminated smoothly to a depth of 163 nm. g) After an additional four 1 µN scratches, the coating thinned to a depth of 218 nm and remained smooth. The 40°C coatings never exhibited thinning.

The difference between the behavior of the 40°C and 50°C coatings strongly indicates that further investigation into the effect of crosslinking is necessary. It is likely

that three regimes of wear behavior will exist: moderate wear resistance, similar to that exhibited by the 50°C coatings, at low crosslink density; improved resistance, similar to the behavior of the 40°C coatings, at intermediate density; and decreasing resistance at high crosslink density, as the coating becomes embrittled and unable to absorb a significant amount of water. Once the most promising coatings have been identified, larger-scale wear testing, including pin-on-disk and joint simulator studies, will be necessary to determine whether the coatings can significantly decrease the wear rate of UHMWPE under clinically-relevant conditions.

Conclusions

The major impact of the studies presented in this dissertation is threefold. First, a method for measuring the thickness of hydrated polymer-on-polymer coatings was developed. This method, which uses ATR-FTIR to quantify the amount of coating present and AFM scratching to calibrate the ATR-FTIR data, addresses a significant and widely-acknowledged challenge in the field of soft coating research. Second, a hydrophilic, biocompatible, wear-resistant coating based on poly(ethylene glycol) was developed as a lubricious surface modification for UHMWPE in acetabular cups. The tribological behavior of the PEG-like coating produced at 50°C was evaluated at three length scales, which allowed for determination of both the mechanisms of failure and several potential approaches to alleviate them. Finally, preliminary studies established that coatings with similar chemistry but different levels of crosslinking exhibit significantly different microscopic wear behavior. A 15-18% increase in the degree of crosslinking is sufficient to eliminate two of the three microscopic wear mechanisms

observed in the less-crosslinked material. This result is interesting for both the basic science of the structure-function relationships in wear-resistant coatings, as well as for the potential clinical application of a successful material.

References

1. Wright, T.M. and D.L. Bartel, *The Problem of Surface Damage in Polyethylene Total Knee Components.* Clinical Orthopaedics and Related Research, 1986(205): p. 67-74.
2. Wright, T.M., et al., *Failure of Carbon Fiber-Reinforced Polyethylene Total Knee-Replacement Components - a Report of 2 Cases.* Journal of Bone and Joint Surgery-American Volume, 1988. **70A**(6): p. 926-932.
3. Edidin, A.A., et al., *Plasticity-induced damage layer is a precursor to wear in radiation-cross-linked UHMWPE acetabular components for total hip replacement.* Journal of Arthroplasty, 1999. **14**(5): p. 616-627.
4. Shi, W., X.Y. Li, and H. Dong, *Improved wear resistance of ultra-high molecular weight polyethylene by plasma immersion ion implantation.* Wear, 2001. **250**: p. 544-552.
5. Klapperich, C., L. Pruitt, and K. Komvopoulos, *Nanomechanical properties of energetically treated polyethylene surfaces.* Journal of Materials Research, 2002. **17**(2): p. 423-430.

6. Bertoti, I., et al., *Nitrogen-PBII modification of ultra-high molecular weight polyethylene: Composition, structure and nanomechanical properties.* Surface & Coatings Technology, 2007. **201**(15): p. 6839-6842.

7. Marcondes, A.R., et al., *Improvements of ultra-high molecular weight polyethylene mechanical properties by nitrogen plasma immersion ion implantation.* Brazilian Journal of Physics, 2004. **34**(4B): p. 1667-1672.

8. Hills, B.A., *Boundary lubrication in vivo.* Proceedings of the Institution of Mechanical Engineers Part H-Journal of Engineering in Medicine, 2000. **214**(H1): p. 83-94.

9. Zhang, M., et al., *A novel ultra high molecular weight polyethylene-hyaluronan microcomposite for use in total joint replacements. II. Mechanical and tribological property weight composite for evaluation.* Journal of Biomedical Materials Research Part A, 2007. **82A**(1): p. 18-26.

10. Moro, T., et al., *Surface grafting of artificial joints with a biocompatible polymer for preventing periprosthetic osteolysis.* Nature Materials, 2004. **3**(11): p. 829-836.

11. Pavoor, P.V., et al., *Wear reduction of orthopaedic bearing surfaces using polyelectrolyte multilayer nanocoatings.* Biomaterials, 2006. **27**(8): p. 1527-1533.

Appendix

Detailed Experimental Protocols

This appendix includes detailed protocols for the following procedures:

Surface Cleaning

Protocol:

1. If there is any ink (from a Sharpie, other marker, or pen) on the surfaces, pre-rinse by squirting with acetone until the dripping acetone is clear.
2. Turn on sonicator heating.
3. Sonicate the samples for 5 minutes in 1% Aquet (or other lab detergent) in deionized water.
4. Rinse the samples and container(s) with deionized water to remove detergent bubbles.
5. Sonicate the samples 3 times for 5-minute intervals in deionized water, changing the water after each interval.
6. Turn off sonicator heating.
7. Sonicate the samples for 5 minutes in acetone.
8. Sonicate the samples for 5 minutes in isopropanol.

Notes:

- For large numbers of small samples, a strainer will be helpful for rinsing the samples and changing the sonication liquids.
- Used acetone and isopropanol are chemical waste and should not be poured down the drain. Since they are volatile (and will be warm after sonication), it is best to handle them in the hood.

This protocol is based on verbal instructions from Lara Gamble at the National ESCA and Surface Analysis Center for Biomedical Problems (NESAC/BIO) facility at the University of Washington.

Tetraglyme Deposition Protocol

This protocol was developed with assistance from Steve Kaplan at 4th State Inc. All depositions were performed at the 4th State facility in Belmont, CA.

Instrument Setup:

1. Use liquid chamber at 4th State Inc., which has a 550 W generator and three mass flow controllers (MFCs). MFC 1 and 2 are for up to 1000 sccm; MFC 3 is for up to 100 sccm.
2. Attach an argon (Ar) line to MFC 1 (or 2) and a second Ar line to MFC 3.
3. For the tetraglyme:
    a. Attach the high-temperature heat tubing to the intake opening on the top of the chamber
    b. Attach a 3-way valve to the free end of the tubing.
    c. Add a needle valve with a shutoff valve to the top, and attach another Ar line to the needle valve.
    d. Connect the syringe pump line to the last part of the three-way valve. Use a 10 ml Hamilton gas-tight syringe and place a check valve between the syringe and the line to ensure unidirectional flow.

Before running samples:

1. Set the heating pads on the sides of the chamber to the desired temperature (usually 50°C).
2. Set the heating tube to 130.0°C.
3. Fill syringe with tetraglyme and program the syringe pump:
    a. Set syringe type to Hamilton 10 ml under "Table."
    b. Select flow rate and volume. Volume is calculated from the flow rate and deposition time, and 0.02 ml extra volume is added to account for loss of fluid volume in the tubing.
4. Flush all Ar lines to remove any traces of other gases.
5. Set the needle valve volume for the Ar flush on the tetraglyme line:
    a. With needle and shutoff valves on the tetraglyme line closed, run 30 sccm of Ar through MFC 3 and allow pressure to reach equilibrium in the chamber.
    b. Open the shutoff valve, then open the needle valve just enough to increase the chamber pressure to the next possible reading (for example, 0.045 Torr to 0.047 Torr). Leave the needle valve open at this setting for all processes. Close the shutoff valve (it will be opened again during the tetraglyme flow step to allow Ar to flow through the heat tubing).
6. Place the screen on the top shelf.
7. Program the plasma chamber using the settings shown below.
8. Do two full pre-runs of the deposition process before depositing tetraglyme on substrates. For tetraglyme step, run 6 ml/hr of tetraglyme at 50 W (9.1% power) for 5 minutes (volume: 0.52 ml).

Plasma chamber programming (use process 4, program in "change settings" mode)

1. Step 1
    a. MFC 1: 250 sccm (25.0%) Ar
    b. MFC 2, 3: 0
    c. RF: 400 W (72.7%)
    d. Time: 3 min
    e. Base pressure: 0.030 Torr
    f. Slow vent: 4 min
2. Step 2
    a. MFC 1, 2: 0
    b. MFC 3: 30 sccm (30.0%) Ar
    c. RF: depends on processing parameters (usually 50 W, 9.1%)
    d. Time: depends on processing parameters (2-40 minutes)
    e. Base pressure: 0.030 Torr
3. Step 3
    a. MFC 1: 250 sccm (25.0%) Ar
    b. MFC 2, 3: 0
    c. RF: 0
    d. Time: 1 min
    e. Base pressure: 0.030 Torr
4. Steps 4 and 5
    a. Repeat step 3

Deposition Process

1. When all samples are in the chamber, all settings are correct, and pre-runs have been completed, make sure key is turned to automatic mode, then press run.
2. Keep notes detailing the length of the initial pumpdown process, the chamber pressure and plasma color during each step, and the heat tubing temperature.
3. When the tetraglyme step (step 2) is about to start, climb onto the stepstool. When the instrument beeps to indicate the start of step 2, open the shutoff valve controlling the Ar flush and press run on the syringe pump.
4. If the match network keeps reaching a load min or indicating cable failure, press the max button a few times until it stabilizes around 20-30%.
5. When the tetraglyme process ends, turn off the Ar shutoff valve. The syringe pump shuts off by itself when it finishes pumping the specified volume.
6. After the process ends, check the chamber for tetraglyme drips and wipe them up with lint-free cloths before starting the next process. Try to run shorter deposition times before longer ones to minimize the effects of tetraglyme buildup in the chamber – a short run after a very long run will deposit more tetraglyme than a short run done before any long runs.
7. After finishing for the day, wipe the inside of the chamber down with ethanol and lint-free cloths. Turn off the heating for the heat tubing and squirt about 10 ml of methanol through the tubing (place a cloth below the intake to catch the drip). Clean the chamber in manual mode with argon or oxygen plasma: 500 sccm (50%) at 400 W (72.7%).

Figure 1: Entire plasma deposition system

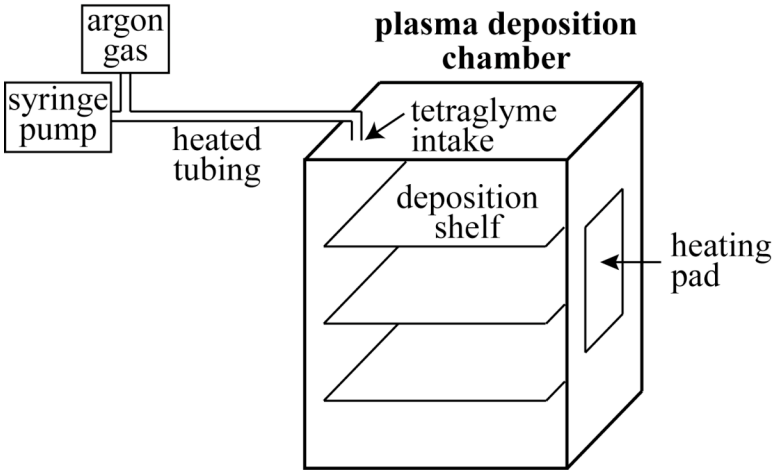

Figure 2: Sample holder for deposition onto pin-on-disk wear pins

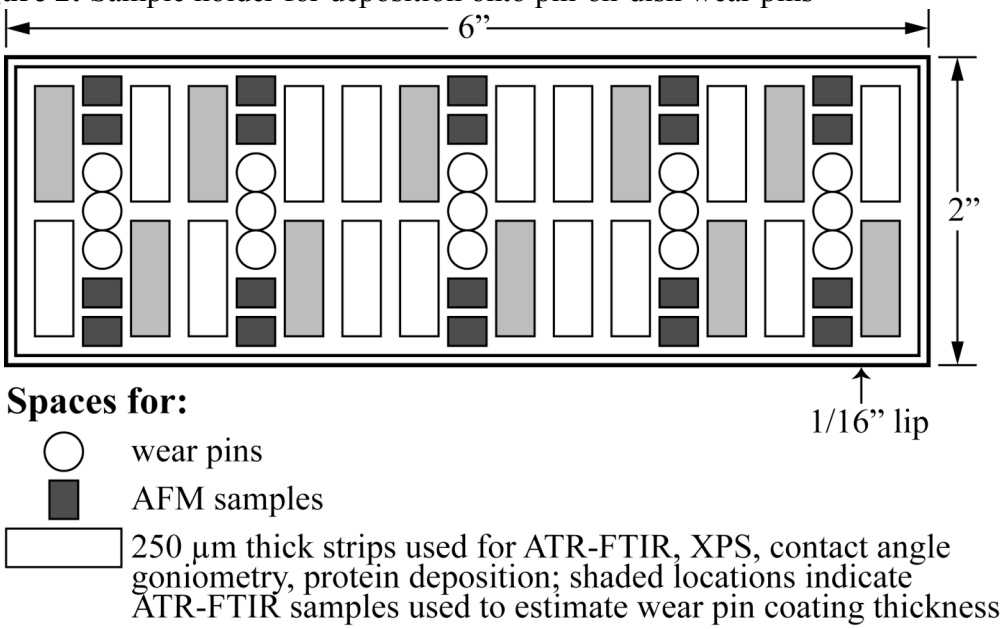

Figure 3: Placement of sample holder in plasma chamber

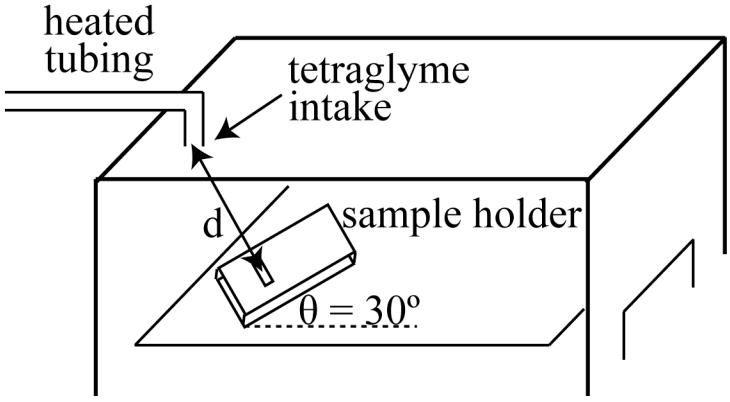

Protein Adsorption Protocol

Materials:
stock solution* (in original BSA-Alexa Fluor 488 bottle): 5 mg/mL
phosphate-buffered saline, pH 7.4
glass microscope slides
glass coverslips
samples (5 mm x 20 mm strips of UHMWPE, PEGylated or not)

*stored in -35°C freezer

Deposition:

1. Thaw both solutions
2. Dilute stock protein solution to desired concentration, making sure to produce at least 1 mL of solution per sample strip
3. Pipet 1 mL of protein solution into one microcentrifuge tube per strip, then add strips to all tubes
4. Let soak at room temperature for 30 minutes
5. Remove strips and shake each in microcentrifuge tubes filled with 1 mL PBS
6. Repeat step 5 twice in fresh tubes of PBS
7. Wick away excess PBS with a Kimwipe, then mount the sample on a microscope slide

Mounting:

1. Clean glass microscope slides and coverslips with acetone
2. Pipet 10 μL of PBS onto each spot on the slide where a strip will be placed
3. Place each strip on a spot of PBS, convex side up
4. Pipet 10 μL of PBS onto the top of each strip
5. Dab a small amount of Permount onto the sides of the slide where the ends of the coverslip will be
6. Place a coverslip onto the slide and hold it down with a weight (chunks of aluminum from the machine shop) until the Permount has dried and the coverslip stays on the slide
7. Store slides in -35°C freezer until fluorescence microscopy is performed

Fluorescence Microscopy:

a. Focus microscope in phase contrast at 5x
b. Change to 20x to take pictures, making sure microscope is still focused
c. After opening the path to the camera, open "Take Fluor Picture" script and click run
    i. exposure time: 7 seconds
    ii. number of pictures per substrate: 5
d. Between each picture, move to a new spot on sample, opening and closing the path to the eyepiece and camera as necessary
e. When complete, open all images
f. Use "Analysis" script to determine average brightness of each picture

Pin-on-Disk Wear Testing Protocol

Setup:

1. Draw ~12 mL of bovine calf serum (diluted 1:1 with deionized water; 0.1% sodium azide added) into a syringe and let it sit to warm to room temperature. Use a fresh needle every time to avoid contaminating the stock serum solution.
2. In separate beakers, sonicate the pin and the disk in deionized water for 10 minutes.
3. Dry the pin on a Kimwipe. Rinse the polished face of the disk with acetone, then dry it with a Kimwipe. Be careful not to scratch the microtomed surface of the pin or the polished surface of the disk.
4. Assemble the disk holder and attach it to the motor platform. Fully tighten all screws.
5. Insert the pin into the collet and tighten the screw in the collet to hold the pin firmly in place. Place the collet into the pin holder, making sure it sits flat in the holder, and tighten the two set screws on the outside of the holder.
6. Screw the pin holder onto the rod at the end of the arm of the wear tester, using washers as spacers to keep arm as horizontal as possible when the pin is touching the disk. Make sure the arm is balanced (by adjusting the weight near the strain gauge and adding weight directly above the pin holder if needed, usually 2/10 lb) such that the pin can hover over the disk without touching it.
7. Mark the wear direction on the front of the pin with a Sharpie.
8. Add the room-temperature serum to the disk, filling the well completely.
9. If running a test longer than about 8 hours, fill the syringe pump with deionized water and set the pump to1 mL/hr. This prevents the system from running dry and maintains a fairly constant concentration of serum.

Friction Calibration

1. On the computer, create a text file and direct the voltage recording program to save to this file. Note: this file must be CLOSED while the voltage data is being recorded; otherwise the data does not write to the file.
2. Place the pin in the serum, but out of contact with the disk. The only weight above the pin should be the weight needed to balance the arm (usually 2/10 lb). Record the voltage for 20 counts.
3. Hang the weight attached to the fishing line from the rod holding the pin and loop the pine over the guide attached to the ring stand on the side of the table. Make sure that the fishing line is as horizontal as possible to ensure that the force is fully lateral, and make sure that the pin is not in contact with the disk (which would create friction). Record this weight and the voltage for 20 counts.
4. Repeat, successively increasing the weights, to attain a range larger than the voltages expected during the wear test. Be sure to record the applied weights for each set of data, starting with 0 g. See Table 1 for the exact masses of the weights.

Wear Testing

1. On the computer, create a new text file for the wear test data and direct the voltage recording program to save to this file.
2. Place the desired weights above the pin. Be sure to also add the weight needed to balance the arm. *This weight does not count toward the applied normal force.*
3. Set the controller dial to the desired speed in rpm (see Table 2).
4. Turn on the power switch.
5. Start the timer.
6. Start recording the friction.
7. Let the experiment run, checking on it periodically to make sure that the serum hasn't leaked away from the disk surface and that the arm isn't vibrating too much. When it has finished, stop recording the friction, then turn off the motor.

Clean-up

1. Remove the serum with the syringe, taking care to avoid scratching the disk.
2. Bring the pin (in holder), disk, and disk holder to 5103.
3. Clean the pin – with wear direction marked! – by dipping it twice in a beaker of fresh deionized water. Let it air-dry on a Kimwipe.
4. Take four ATR-FTIR spectra of the pin once it dries, then place it in the freezer to minimize microstructural relaxation.
5. Rinse the pin and disk holders in deionized water.
6. Rinse the disk in deionized water. If needed, gently wipe the surface with acetone and a Kimwipe to remove the wear track. Sonicate for 10 minutes in deionized water, then rinse the polished surface with acetone.

Table 1: Actual mass of calibration weights

Marking	Mass in g
500 g (cylindrical weight with hook)	153.5
2/10 lb	90.7
4/10 lb	181.5
½ lb	227.3 (calculated, roughly verified)

Table 2: Conversion from rpm to actual speed

Rpm setting	Speed calculated from calibration curve, y = 0.0095x (cycles/sec)	Calculated speed for 40 mm diameter wear track	
		mm/sec	m/min
10	0.095	11.9	0.72
20	0.190	23.9	1.43
30	**0.285**	**35.8**	**2.15**
40	0.380	47.8	2.87
50	0.475	59.7	3.58
60	0.570	71.6	4.30
70	0.665	83.6	5.01
80	0.760	95.5	5.73
90	0.855	107.4	6.45

Publishing Agreement

It is the policy of the University to encourage the distribution of all theses and dissertations. Copies of all UCSF theses and dissertations will be routed to the library via the Graduate Division. The library will make all theses and dissertations accessible to the public and will preserve these to the best of their abilities, in perpetuity.

I hereby grant permission to the Graduate Division of the University of California, San Francisco to release copies of my dissertation to the Campus Library to provide access and preservation, in whole or in part, in perpetuity.

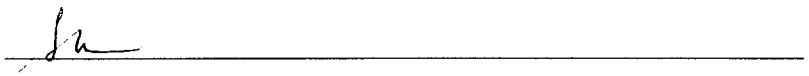

Author Signature

5/22/08

Date